HOKKAIDO UNIVERSITY

Title	Study on Mixed Ionic-Electronic Conductivity of Inorganic Thin Films Fabricated by Reactive Sputtering Process
Author(s)	倉, 千晴
Degree Grantor	北海道大学
Degree Name	博士(工学)
Dissertation Number	甲第13244号
Issue Date	2018-03-22
DOI	https://doi.org/10.14943/doctoral.k13244
Doc URL	https://hdl.handle.net/2115/70120
Type	doctoral thesis
File Information	Chiharu_Kura.pdf



Hokkaido University Collection of Scholarly and Academic Papers : HUSCAP

Study on Mixed Ionic-Electronic Conductivity of Inorganic Thin Films Fabricated by Reactive Sputtering Process

反応性スパッタ法により作製した無機薄膜の
イオン－電子混合伝導性に関する研究

Chiharu Kura

Graduate School of Chemical Sciences and Engineering

Hokkaido University

March 2018

Table of contents

Chapter 1 Introduction

1-1 History of Solid State Ionics ・・・1

1-2 The issue of mixed ionic-electronic conductors ・・・4

1-3 Approaches and objectives of this thesis ・・・7

(a) Memristive switching caused by room temperature oxide ion conduction of Ga(I) suboxides ・・・10

(b) Development of metal nitride nanocrystalline membranes with high hydridic conductivity ・・・13

1-4 Contents of this thesis ・・・16

1-5 References ・・・18

Chapter 2 Development of resistive switching gallium oxide thin film with tailoring gallium valence state and oxygen deficiency

2-1 Introduction ・・・27

2-2 Experimental ・・・29

2-3 Results ・・・31

2-4 Discussion ・・・43

2-5 Conclusion ・・・46

2-6 References ・・・47

Chapter 3 Hydrogen separation by nanocrystalline titanium nitride membranes with high hydride ion conductivity

3-1 Introduction ・・・51

3-2 Experimental ・・・53

3-2-1 Hydrogen permeability tests

(a) Preparation of aluminum porous support ・・・53

(b) RF sputtering deposition of TiN_x membranes ・・・56

(c) Hydrogen permeation tests of TiN_x membranes ・・・57

(d) Method to determine the p_{H2} at TiN_x/support interface ・・59

3-2-2 Characterization techniques

(a) Material characterization ・・・61

(b) Density-functional theory (DFT) calculations ・・・63

3-3 Results and Discussion

3-3-1 Fabrication of TiN_x membranes ・・・65

3-3-2 Hydrogen permeability ・・・66

3-3-3 Hydrogen solubility in TiN_x ・・・77

3-3-4 Mobile hydrogen species ・・・82

3-3-5 Hydride ion conduction mechanism ・・・84

3-4 Conclusion ・・・87

3-5 References ・・・95

Appendix: Estimation of hydridic ion conductivity ・・・101

(a) Comparison with other hydrogen permeable membranes

(b) Hydridic ion conductivity

References of Appendix ・・・106

Chapter 4 Improved hydrogen permeability of TiN_x nanocrystalline membranes by microstructural tailoring

4-1 Introduction ・・・108

4-2 Experimental

4-2-1 Hydrogen permeability tests ・・・109

4-2-2 Characterization techniques ・・・110

4-3 Results and Discussion

4-3-1 Fabrication of TiN_x membranes ・・・111

4-3-2 Hydrogen permeability ・・・113

4-3-3 Grain size dependence of hydrogen solubility ・・・122

4-4 Conclusion ・・・126

4-5 References ・・・130

Chapter 5 Hydrogen permeability of hafnium nitride nanocrystalline membranes by interfacial hydridic conduction

5-1 Introduction ・・・132

5-2 Experimental

5-2-1 Hydrogen permeability tests

(a) RF sputtering deposition of HfN_x membranes ・・・133

(b) Hydrogen permeation tests of HfN_x membranes ・・・134

5-2-2 Characterization techniques

(a) Material characterization ・・・135

(b) Density-functional theory (DFT) calculations ・・・137

5-3 Results and Discussion

5-3-1 Fabrication of HfN_x membranes ・・・138

5-3-2 Hydrogen permeability ・・・145

5-3-3 Mobile hydrogen species ・・・147

5-3-4 Grain size dependence of permeability and solubility ・・155

5-3-5 Comparison of HfN_x and TiN_x ・・・161

5-4 Conclusion ・・・163

5-5 References ・・・166

Chapter 6 Summary ・・・170

List of publications ・・・175

Acknowledgement ・・・178

Chapter 1

Introduction

1-1 History of Solid State Ionics

Solid ionic conductors are solid state materials that can generate the electric current fluxes of ions under applied field, and the sciences and technology involving solid ionic conductors are called Solid State Ionics. Solid State Ionics is a multidisciplinary scientific field, where chemistry, physics and materials science meet to explore ionic transport in solids including ceramics, glasses, polymers and composites with various morphologies (ex. single crystals, sintered bodies, composites or thin films).[1] In 21st century, Solid State Ionics is emerged as one of the most attractive scientific fields because of its useful technological applications (ex. batteries,[2-13] fuel cells,[14-19] redox flow batteries,[20,21] capacitors,[22,23] sensors[24-31] or gas separation membranes[32-34]). Moreover, their applied research fields have been expanded to the information and communication field (ex. memristors,[35-37] switches,[38,39] conductor[40-42] or photo-nanoionic devices[43,44]), and life sciences (Fig. 1-1).

The history of the ionic conduction in solids originates in the discovery of the validity of Faraday's law for solid conductors (i.e. the amount of mass transported by the current in the solid was given by Faraday's law) which is demonstrated by Warburg et al. in 1833.[45-47] From a microscopic standpoint, ionic conduction in solids is caused by the

existence of defects in the solid bulk interior. These defects are known as point defects; Schottky defect is formed when oppositely charged ions leave their lattice sites, creating lattice vacancies in ionic crystals. In Kröger-Vink notation, the above reaction is denoted as

$$\text{Null} \leftrightarrows V_M'' + V_X^{\bullet\bullet} \quad (1\text{-}1)$$

Frenkel defect is formed when an ion moves from a lattice point to an interstitial position, creating both a lattice vacancy and an interstitial ion.

$$\text{Null} \leftrightarrows V_M'' + M_i^{\bullet\bullet} \quad (1\text{-}2)$$

The ionic diffusion mediated via vacancies are called as vacancy diffusion mechanism, and the diffusion of interstitial ions are categorized to interstitial diffusion mechanism (Fig. 1-2).

The theory of defect thermodynamics in solids was began by Joffé Frenkel, suggesting that the concentrations of defects obey laws of mass action similar to those holding for dissociation equilibria in liquid electrolytes. This concept was taken over by Schottky and Wagner, and thus equilibrium thermodynamics of point defects and their diffusion kinetics in the bulk of solids have been well studied and understood.[48-52] Therefore, the development of new materials based on the fundamental theory described above has become a central issue of Solid State Ionics.

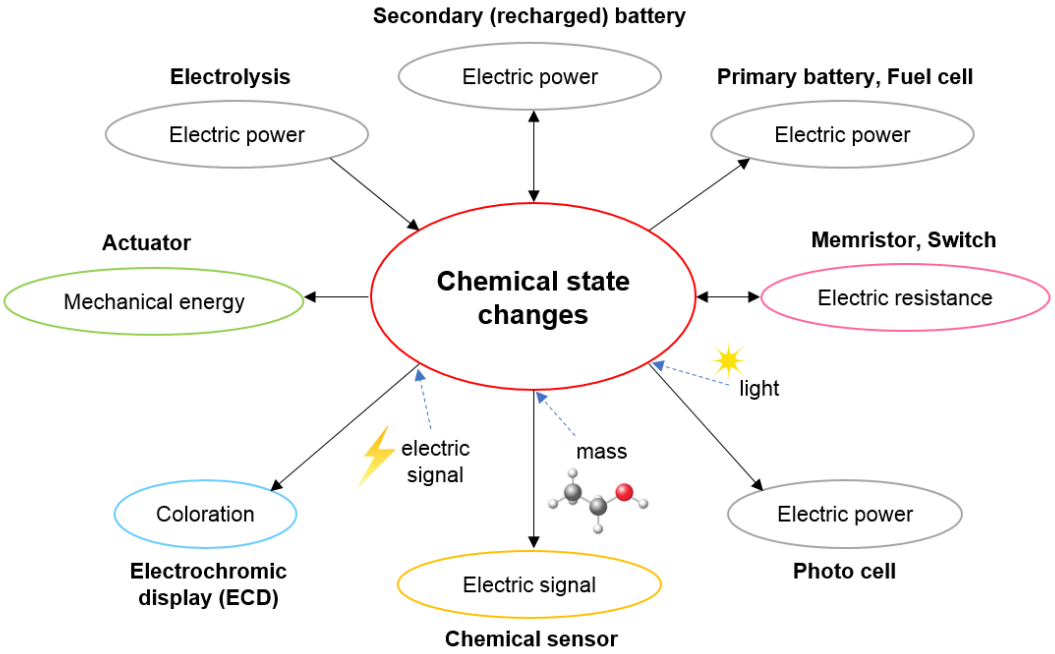


Fig. 1-1 Electrochemical devices driven by ion-conductivity of solids.[53]

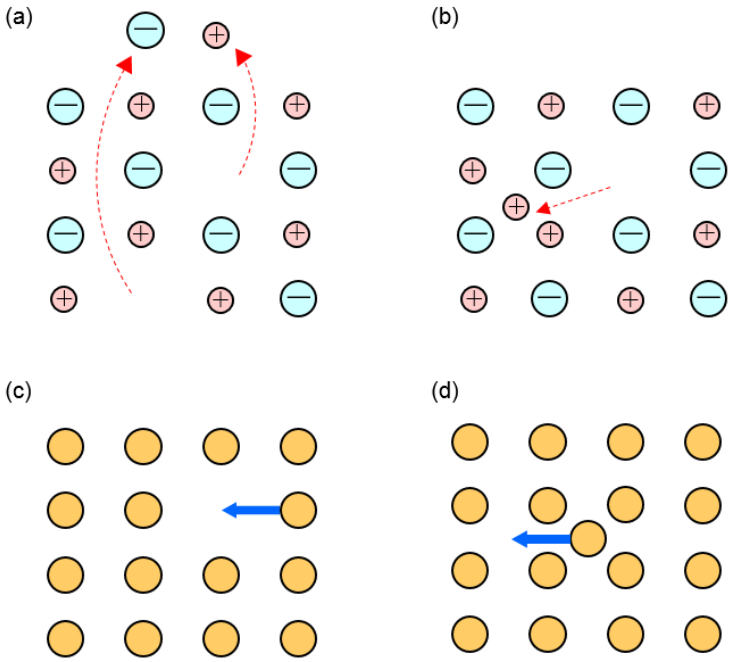


Fig. 1-2 Schematic illustrations of (a) Schottky defect, (b) Frenkel defect, (c) vacancy defect mechanism and (d) interstitial diffusion mechanism.

1-2 The issue of mixed ionic-electronic conductors

In 1960's, the theory of mixed ionic-electronic conductor (MIEC), which conduct both ions and electronic charge carriers (electrons and/or holes), was developed by Wagner, Hebb, and Yokota et al.[40-42] MIECs play a crucial role in various electrochemical devices because the density of both ionic and electronic fluxes governs the kinetics of elemental charge transfer reaction. Accordingly, it is strongly motivated to develop MIECs realizing high ionic conductivity at relatively low temperatures in order to increase efficiency and lifetime and expand the range of the applications of the solid state electrochemical devices, such as solid-state fuel cells,[54-56] all-solid-state battery,[57,58] separation membranes,[32-34] memristive switches[35-37] and photovoltalic-devices.[43,44] Table 1-1 show the summary of various MIECs and their related applications.

In the battery industry, many types of MIECs have been intensively used for the cathode/anode materials.[54-61] $LiCoO_2$ spinel is most famous cathode materials of lithium-ion secondary battery, which is the largest commercial application for solid ionic materials. This oxide conducts reversible Li insertion/desertion for the discharge/charge processes via coupled with Co redox due to the excellent Li^+ ion electron mixed conductivity, and the Li^+ ion conductivity reaches to 5.0×10^{-6} S cm^{-1} even at room temperature.[60] Recently, $LiMn_{1.5}Ni_{0.5}O_4$ has also attracted much attention as an alternative cathode because of the superior Li^+ ion conductivity at room temperature.[62,63]

Another example of room temperature MIECs is I^- conducting, p-type semiconductor $CH_3NH_3PbI_3$. Recently, this compound has attracted much attention as a key material of organic perovskite solar cells,[64-68] because the systems using $CH_3NH_3PbI_3$ in hole

injection layer achieved the high efficiency as high as Si-solar cells. Etgar et al. reported that this superior I^- conductivity makes a crucial role for the efficient hole-electron separation without abrupt recombination at the $CH_3NH_3PbI_3/TiO_2$ hetero junctions.[67,68]

Unfortunately, MIECs that exhibit fast oxide ion conductivity at room temperature have not been available yet,[69] although these materials are promising for the fuel cell electrodes, ultrapure oxygen gas separation membranes and resistive switching memory etc. A family of perovskite-type cobaltites and its derivatives, such as $Sm_{0.5}Sr_{0.5}CoO_3$ (SSC) and $La_{0.6}Sr_{0.4}Co_{0.2}Fe_{0.8}O_3$ (LSCF), has been known to exhibit pronounced oxide ion electron mixed conductivity at elevated temperatures, and thus, they are promising as a porous cathode of solid oxide fuel cells (SOFCs).[70-73]

Room-temperature proton conducting MIECs are also promising for the fuel cell electrodes, ultrapure hydrogen gas separation membranes, hydrogenation membrane reactors and so on. Unfortunately, such materials have not been discovered yet, although mass of hydrogen is much smaller than other ions such as Li^+ or O^{2-}.

Based on vacancy defect or interstitial diffusion mechanism (Fig. 1-2), West et al. listed the crystallographic-structural factors for the fast ion conductors as follows;[74]

1) A large free volume is in crystal lattice.

2) Equivalent unoccupied sites are in crystal lattice

In fact, most of fast ion conductors take crystal structures satisfying these conditions, i.e. Fluorite structure, Perovskite-related structure, Spinel-type structure and/or Layered structure.[74] Although numerous efforts have been done to develop new fast ion conductors with the crystal structural optimization, the conductors taking alternative structures to these groups are still rather few, and thus, currently, material chemists are stimulated to

explore artificial MIECs having significantly-high conductivity at ambient temperature by changing technology.

Table 1-1. Summary of MIECs and its related application at room temperature.

Mobile ion carrier	MIECs	Crystalline structure	Operating temperature	Conductivity at 25°C / S cm^{-1}	Applications
Li^+	$LiCoO_2$	Spinel	rt	5.0×10^{-6}	Cathode of Li battery
	$LiMn_{1.5}Ni_{0.5}O_4$	Spinel	rt	2.0×10^{-7}	Cathode of Li battery
	$LiFePO_4$	Alluaudite	rt	5.0×10^{-5}	Anode of Li battery
H^+	$Ni/BaCe_{1-x}Y_xO_2$	Perovskite	T>700°C	-	Dense separation membrane Fuel cell anode
O^{2-}	$La_{0.5}Sr_{0.5}CrO_3$	Perovskite	T>500°C	-	Dense separation membrane
	$La_{0.6}Sr_{0.4}Co_{0.2}Fe_{0.8}O_3$	Perovskite	T>800°C	1.0×10^{-2}	Fuel cell cathode
	$Sm_{0.5}Sr_{0.5}CoO_3$	Perovskite	T>500°C	-	Fuel cell cathode
	$BiCuVO_x$	Fluorite	T>300°C	1.0×10^{-3}	Fuel cell cathode
	TiO_x, TaO_x thin films	Amorphous	rt	-	Memristive switching
I^-	$CH_3NH_3PbI_3$	perovskite	rt	1.1×10^{-2}	Dye for solar cells

1-3 Approaches and objectives of this thesis

As mentioned before, the development of artificial ion conductors that possess significantly high ionic conductivity at room temperature is of great challenge for materials chemists. The defects in solids essentially act as an electron donor or acceptor, so that the defect concentration should be described in terms of equilibrium with electronic carrier in semiconductor materials. For instance, the formation of oxygen vacancy leaves electronic carriers into the solids for the charge neutrality as follows.

$$O_O^{\times} \rightarrow V_O^{\bullet\bullet} + 1/2O_2 + 2e^- \qquad (1\text{-}3)$$

This strongly suggest that the defect thermodynamics could strongly correlate with the concentrations and/or energy levels of the electronic carriers in MIECs. In fact, several authors reported on the enhanced ionic conductivity due to the thermodynamic interaction between electron and the corresponding defects. In 2016, proton conductivity induced by exchange between proton and ligand holes have been reported for $SmNiO_3$ systems by Zhou et al.[75] They fabricated micro-fuel cells comprising self-supporting $SmNiO_3$ electrolyte thin films with Pt cathode and Pd anode by combination of rf sputtering deposition and dry patterning processes. $SmNiO_3$ is a Mott-insulator, i.e. $SmNiO_3$ become insulator at temperatures above 400°C due to the charge ordering in NiO_6 units by the electronic transition from d^9L^1 to $d^8\underline{L}^1$ state ($\underline{L}$; a ligand hole). When such films are exposed to hydrogen atmosphere, carrier exchange between positively-charged ligand hole, $\underline{L}$, and proton, H^+, takes place, thereby the compound exhibits excellent proton conductivity.[75] The conductivity reaches to 6.3×10^{-3} S cm^{-1} at 400°C, which is similar to the fast proton-conducting $BaZr_{0.8}Y_{0.2}O_3$.

Recently, Lacorre et al. discovered that a family of $La_2Mo_2O_9$, so-called LAMOX, exhibits super oxide ion conductivity in the relatively low temperature range.[76,77] LASMOX takes same structure as β-$SnWO_4$, in which Sn^{2+} ions forms distorted nine-coordinated polyhedral with oxygen of tetrahedral WO_4^{2-} oxidations. Sn^{2+} ions take the electronic configuration of $[Kr]4d^{10}5p^2$ and its largely-expanded $(5s)^2$ lone pairs have the same diameters as that of oxide ion (O^{2-}). Hence the isomorphous $La_2Mo_{1.7}W_{0.3}O_9$ retain 'channel' to accommodate oxide ions near La^{3+} ions because La^{1+} ions have no lone pairs, despite occupying equivalent Sr^{2+} state as $SrWO_4$, and thus the oxide ion channel can be formed through vacancy of the lone pair.[77]

Recently, more and more evidences of the importance of nanoscale structure in relation to ionic conductivity have been compiled,[78-81] where not only strong variations in the conductivities are achieved but also qualitative effects such as changing the type of conductivity could be observed. Maier et al. reported that artificial thin films comprising BaF_2 and CaF_2 alternative multilayers exhibit emergent enhancement of F^- ion conductivity, achieving few orders of magnitude higher conductivity than those of BaF_2 and CaF_2 bulks.[81] In more recent year, García-Barriocanal et al. reported that colossal oxide ion conductivity in the artificial heterostructures comprising the yttria-stabilized ZrO_2 (YSZ) ultrathin epitaxial layer on a (100)-oriented $SrTiO_3$ (STO) substrate.[82] Since the lattice mismatch between YSZ and STO are relatively large (7%), the large mechanical strains are accumulated in vicinity of YSZ/STO interfaces, which could lower the bottleneck of oxygen vacancy hopping and thus encourage the oxide ion migration along the interfaces. Consequently, oxide ion conductivity of the artificial heterostructure is 8 orders of magnitude higher than that of YSZ bulk.[82]

In summary, it is concluded that the electronic and/or interfacial phenomena in solids[73-75] offer a new opportunity to develop room-temperature fast ion-conducting materials. Normally, high temperature sintering processes have been applied to fabricate ceramic ion conducting materials in order to highly-densified sintered bodies, however, those are rather unsuitable for the development of new artificial ion conductors with tailoring microstructures and/or electronic states. It is difficult to prepare the nanostructured materials retaining large volume of grain boundary interfaces by such conventional process because of significant grain growth during sintering. Furthermore, the difficulty also encounters in the preparation electronic materials because the precise controls of dopant concentrations and stoichiometry are required to tune the electronic properties of inorganic compounds.

Sputtering is a technique to deposit dense thin films uniformly over a wide area of substrates by colliding an inert gas (ex. Ar) against targets at a high speed. Especially, radio frequency (RF) sputtering has the following advantages;

1) Various kinds of materials (ex. high melting point metals, alloys, oxides, nitrides, sulfides, polymers, etc.) can be used as targets.

2) Multi-target sputtering (co-sputtering) enables the fabrication of various hybrid materials, such as oxide-metal nanocomposites, oxide alloys, ceramics nanocomposites and so on, with controlling the structure and composition in nanometer thickness precision.

3) Sputtering of metals under reactive gases, such as O_2, N_2, H_2, etc. in addition to sputtering gas (normally Ar), so-called, reactive sputtering enables facile formation of metal oxides, nitrides, hydrides and so on. In this case, it is feasible to adjust the

nonstoichiometry of the deposited materials, thereby, valence state of the metal components by controlling the reaction gas concentrations.[83-86]

4) Deposition can be carried out at low temperatures, and thus, it is easy to fabricate densely-packed films of nanostructured materials, such as nanocrystalline membranes, nanolaminates, and nanohybrids without significant grain growth.

Based on these features, it is concluded that sputtering is advantageous to fabricate artificial ion conductors with tailored nonstoichiometry, valence state and nanometer-sized morphology.

To sum up, the objective of the present thesis is to develop enhanced ion-electron mixed conducting films based on the thermodynamic interaction between ionic defects and electron carriers or the formation of interfacial ion conducting pathways. Such materials have been attempted to be fabricated by reactive sputtering techniques with precisely-controlling the stoichiometry and microstructures in a dimension of nanometer. The more detail objectives of this thesis are summarized below.

(a) Memristive switching caused by room temperature oxide ion conduction of Ga(I) suboxides

A memristor is a forth fundamental circuit element, defined as a resistive switching device that varies its internal resistance state according to the history of the applied voltage and current (Fig. 1-3(a)).[35-37] Following the definition by Chua et al.,[87,88] it can be described by a set of equations including the following current equations,

$$v = R(x)i \qquad (1\text{-}4)$$

$$\frac{dx}{dt} = f(x, i) \qquad (1\text{-}5)$$

here *V*, *I* and *R* are the voltage, current and resistance, respectively. *x* is an internal state variable, described by a time-varying function *f*, and it is crucial to the switching dynamics of the memristor. Therefore, memristor can still remember how much voltage was applied before and for how long when the applied voltage is turned off, and the feature is characterized by figure-eight pinched hysteretic *I*-*V* curves (Fig. 1-3(b)).

In principal, mixed ionic electronic conductors (MIEC) sandwiched by two blocking electrodes may show homogeneous resistive switching, if the ions are uniformly conductive throughout the film bulk, even at room temperature, since the homogeneous migration of ions will modify the electronic carrier distribution across the conductor, and thus its bulk resistivity.[35,89-91] However, there is only very few well-known bulk memristive systems[92-95] since the bulk ionic conductivity of MIECs is usually very low near room temperature. Furthermore, the direct evidence for the bulk state function of the switching system is still missing. Hence, it is a great challenge for materials scientists to establish a non-filamentary-type MIEC memristor based on the efficient, bulk ion conduction at low temperatures.

In more recent year, Aoki et al. reported enhanced oxide ion conduction in the thin films of amorphous gallium(I) suboxide at room temperature.[96] The mechanism of the oxide ion conductivity has been still unclear, however, it would be attributed to the large polarizability of Ga(I) states by the following way. Ga(I) states have electronic configuration of $[Ar](4s)^2$, thereby possessing a $(4s)^2$ lone pair. Because 4s orbital is specially expanded compared to d orbitals, coulombic interaction between Ga(I) cation and O^{2-} anion is partly shielded by the $(4s)^2$ lone pair and thus, dissociation energy of

mobile oxide ions could decrease (Fig. 1-3(c)). Since Ga(I) suboxides are not thermally stable under oxidative atmosphere at elevated temperature, it is a great challenge to prepare such oxides with tailoring their oxygen nonstoichiometry precisely.

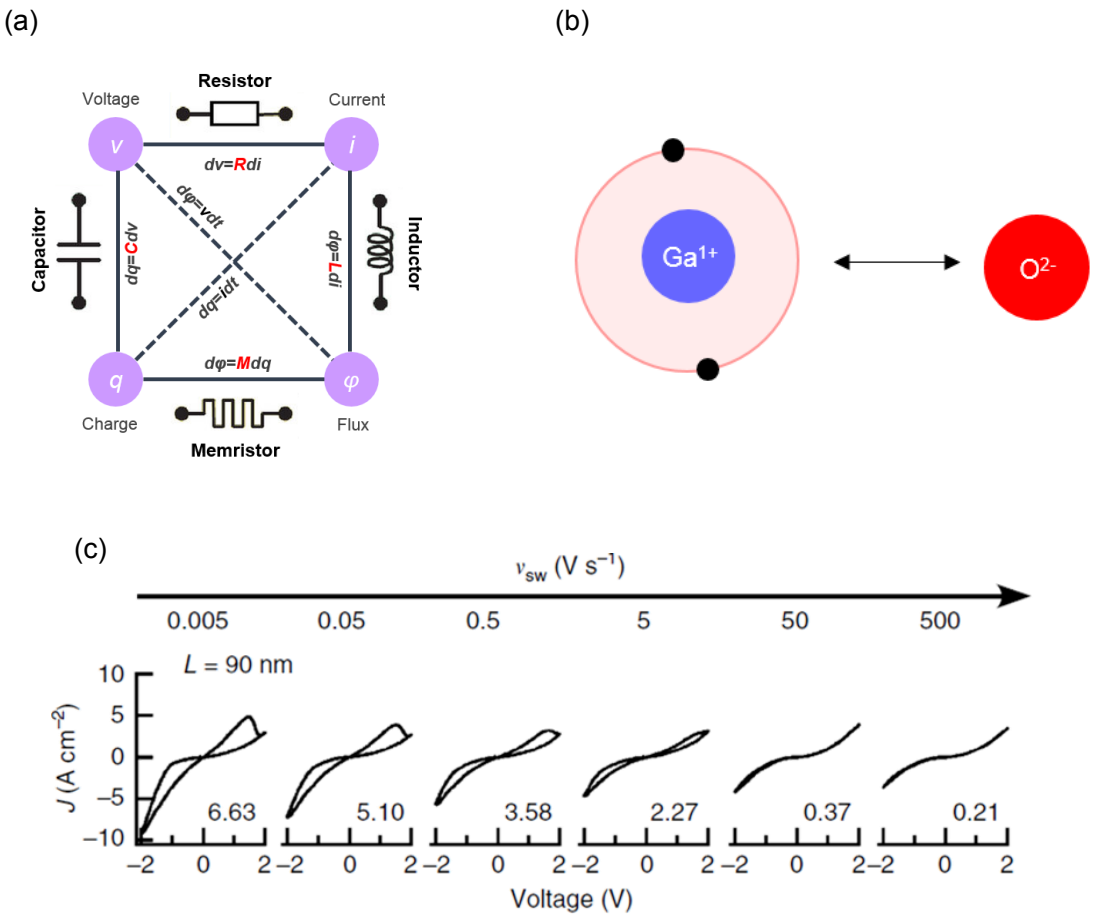


Fig. 1-3 (a) The four basic circuit elements and their relationships. (b) Coulombic interaction between O^{2-} anion and $(4s)^2$ lone pair on Ga(I) cation. (c) Strongly-time-dependent *I-V* characteristics of *a*-$GaO_{1.1}$ thin films with thickness of 90 nm. The *I-V* loops were measured at 25°C with various voltage-sweep rates v_{sw} in the range of 0.005–500 V s^{-1}. [96]

(b) Development of metal nitride nanocrystalline membranes with high hydridic conductivity

Recently, hydrogen is attractive as "clean energy" because it can be made from water electrolysis by renewable energy such as sunlight, wind or water power generation.[97,98] room temperature hydrogen ion conductors are promising as a separation membrane in order to produce ultrapure hydrogen for fuel cell systems.[99-102] $BaCeO_3$, $SrCeO_3$ (perovskite-type), $BaM_{1-x}M'_xO_{3-\delta}$ (M=Zr, Ce; M'=Y, Nd, Gb, Yb, etc) or related cermet materials (ex. Mixture of $BaZr_{1-x}Ce_{0.9-x}Y_{0.2}O_3$ and NiO) have been investigated as a hydrogen separation membrane of mixed proton-electron conductors (MPECs) (Fig. 1-4).[32, 103-109] In these oxides, protons are incorporated by association between the oxygen vacancies and water molecules in gases as follows.

$$Vo^{\bullet\bullet}+O_O^{\times\times}+H_2O \rightarrow 2OH_O^{\bullet} \qquad (1\text{-}6)$$

This means that protonic defects are incorporated to compensate the excess negative change of M'^{3+} acceptor dopants on M^{4+} sites. However, the proton migration in these MPECs requires large activation energy owing to trapping by negatively charged aliovalent dopants, and thus, these MPECs are normally operative at elevated temperature (> 600ºC).[32,108,109]

As well as oxide materials, nitride or carbide materials (ex. HfN intermediate layer or TiC_x) have been reported to form hydrogen defects easily under hydrogen gas atmosphere.[110-112] Although hydrogen in metal oxides favors to form protonic defects, one in metal nitrides tends to form hydride defects in accordance with the Fermi energy levels.[113] Van de Walle have extensively studied the behavior of hydrogen in metal nitrides by theoretical calculations and vibrational spectroscopy, and found that hydrogen

acts as a proton (H^+) or hydride ion (H^-) in metal nitrides if the Fermi energy level is low or high enough relative to ε(+/–) threshold (–4.4 eV), respectively.[113] Actually, hydride ion is more attractive than proton for the ionic conduction due to the large polarizability; the diameter of the hydride ion is 10^5 times larger than that of proton, so that hydride ion is expected to migrate more easily than proton due to the large polarization. Accordingly, hydride ion-electron mixed conductor could be alternative to the proton-electron mixed conductor[32, 98, 99, 108,109,116-124] (Fig. 1-4), resulting in the third member of dense hydrogen permeable membranes.

Based on the aforementioned model, group IV metal nitrides are expected to give rise to hydridic defects under hydrogen gas atmosphere, because the Fermi energy level of Group IV metal nitrides (ex. TiN, ZrN, HfN; around –4.2 eV vs. V. L.) is located above the ε(+/–) threshold, as shown in Fig. 1-5,[114,115] Unfortunately, despite their potential, the hydrogen diffusivity of the metal nitride systems has not been conducted extensively as much as metal oxide systems. Hence, it is strongly motivated to investigate the hydrogen defect formation behavior and its transport properties of metal Group IV metal nitride systems in order to realize hydride ion-electron mixed conducting materials.

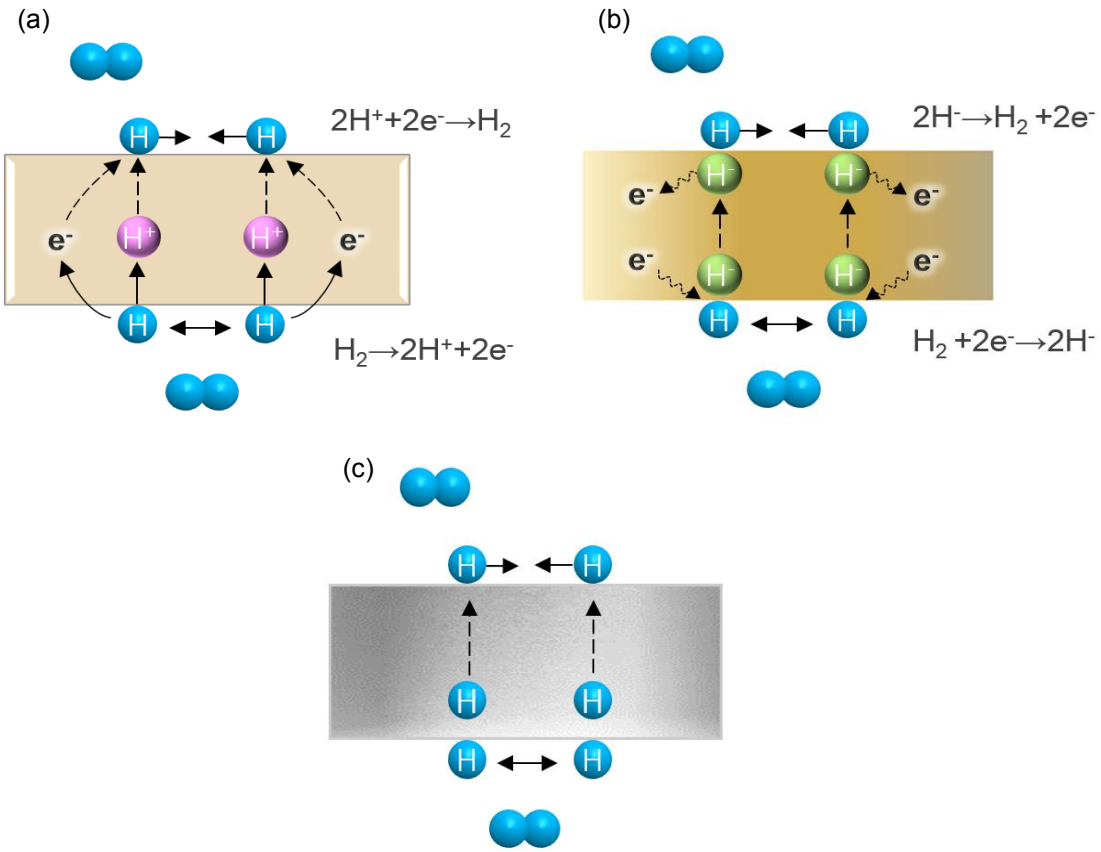


Fig. 1-4 Schematic representation of the hydrogen permeable membranes due to (a) mixed proton-electron conductor, (b) hydride ion-electron conductor and (c) hydrogenation of alloys.

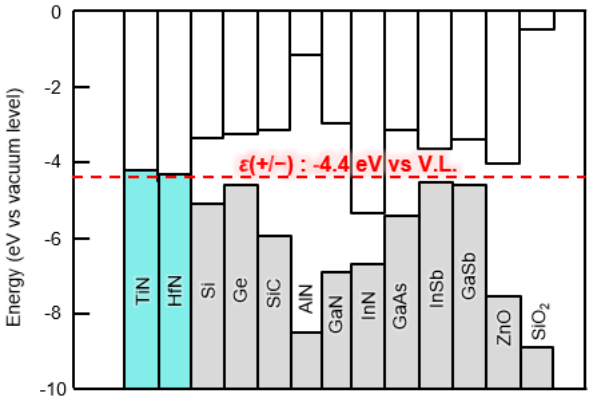


Fig. 1-5 Band line-ups of various compounds and position of the $\varepsilon(+/-)$ level of hydrogen. For each material, the green and gray bars indicate the position of the valence-band maximum, the white bars indicate the position of the conduction-band minimum.[117]

1-4 Contents of this thesis

This thesis consists of a total of six chapters.

In Chapter 1, the history and past studies of mixed ionic-electronic conductors are overviewed and objectives in these studies are described.

In Chapter 2, in order to design a room-temperature oxide ion conductor based on the electronic-ion correlation, oxide glass alloys including Ga(I) suboxides were fabricated by RF cosputtering with Cr and Ga_2O_3 targets. The resultant films show strongly-time dependent switching attributed to the pronounced oxide ion conductivity at room temperature.

In Chapter 3, nanocrystalline TiN_x membranes were fabricated by RF reactive sputtering. TiN_x membranes exhibit excellent hydrogen permeability due to the fast hydride ion-electron mixed conductivity. The hydrogen permeability is higher than that of state-of-the-art Pd membranes at room temperature by several orders of magnitude, and thus these findings lead new concept to develop Pd-alternative hydrogen membranes that can be operative at room temperature.

In Chapter 4, the detailed hydride ion conduction mechanism in TiN_x is established. Their hydrogen fluxes increase with decreasing the nanocrystalline size, revealing that the hydride ions diffuse through the grain boundary region without entering the bulk.

In Chapter 5, hydrogen permeability of the other group IV metal nitride, HfN_x were investigated. It has been demonstrated that nanocrystalline HfN_x membranes have also excellent hydrogen permeability as well as TiN_x due to the interfacial mixed hydride ion conductivity, confirming that the hydride diffusion pathway in HfN_x is same as in TiN_x.

Combined with the results of TiN_x (Chapter 3 and 4), a general guideline to develop Pd-alternatives by transition metal nitrides is established; nanocrystalline metal nitrides with relatively high Fermi energy can show the excellent hydrogen permeability due to interfacial hydridic conduction.

Finally, all the results and achievements in this study are summarized in Chapter 6.

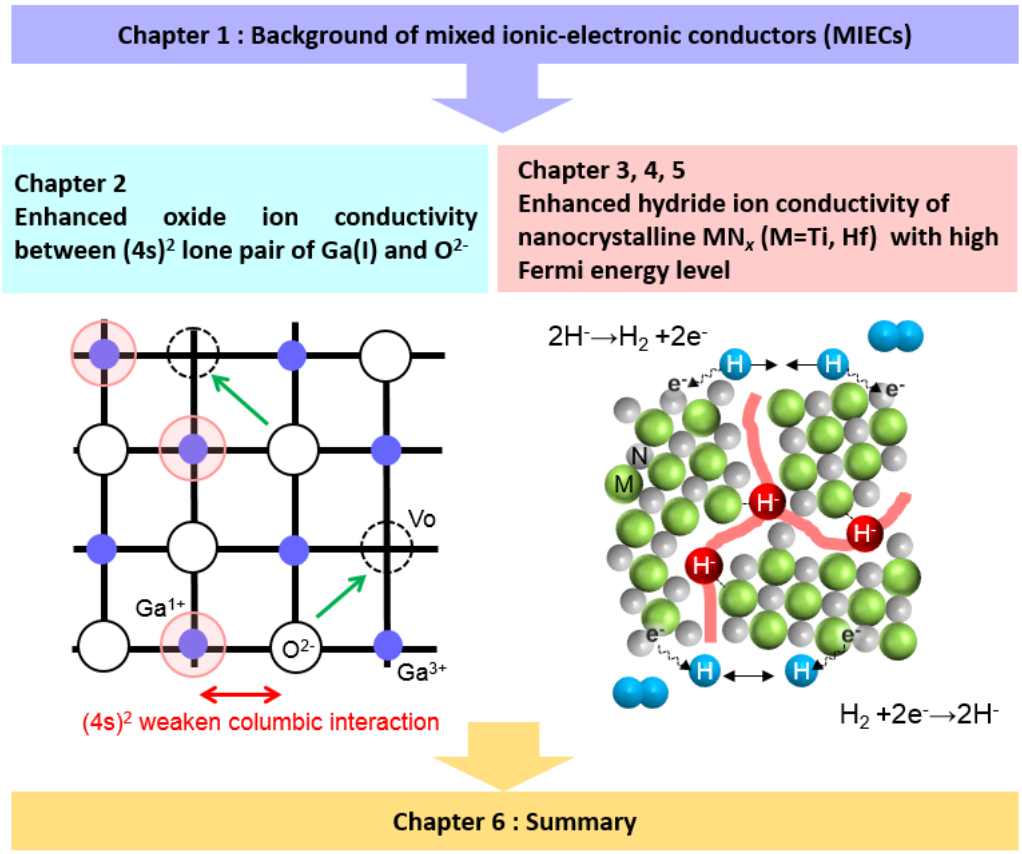


Fig. 1-6 Schematic illustrations of contents in this thesis.

1-5 References

1. Rickert, H. *Electrochemistry of Solids: An Introduction (Inorganic Chemistry Concepts 7)*; Springer-Verlag Berlin, Heidelberg, 1982.
2. Armand, M. B. *Annu. Rev. Mater. Sci.* **1986**, 16, 245-261.
3. Bruce, P. G.; Vincent, C. A. *Faraday Discuss. Chem. Soc*. **1989**, 88, 43-54.
4. Bruce, P. G.; Vincent, C. A. *J. Chem. Soc. Faraday. Trans.* **1993**, 89, 3187-3203.
5. Lazzari, M.; Scrosati, B. *J. Electrochem. Soc.* **1980**, 127, 773-774.
6. Mohri, M.; Yanagisawa, N.; Tajima, Y.; Tanaka, H.; Mitate, T.; Nakajima, S.; Yoshida, M.; Yoshimoto, Y.; Suzuki, T.; Wada, H. *J. Power Sources.* **1989**, 26, 545-551.
7. Nagaura, T.; Tazawa, K. *Prog. Batteries Sol. Cells.* **1990**, 9, 20-22.
8. Dunn, B.; Schwarz, B. B.; Thomas, J. P.; Morgan, P. E. D. *Solid State Ionics.* **1988**, 28-30, 301-305.
9. Duncan, G. K.; West, A. R. *Solid State Ionics.* **1988**, 28-30, 338-343.
10. Abraham, K. M.; Jiang, Z. *J. Electrochem. Soc.* **1996**, 143 1-5.
11. Ogasawara, T.; D´ebart, A.; Holzapfel, M.; Nov´ak, P.; Bruce, P. G. *J. Am. Chem. Soc.* **2006**, 128 1390-1393.
12. Peng, Z.; Freunberger, S. A.; Chen, Y.; Bruce, P. G. *Science.* **2012**, 337, 563-566.
13. Armand, M.; Tarascon, J. M. *Nature.* **2008**, 451, 652-657.
14. Steele, B. C. H.; Middleton, P. H.; Rudkin, R. A. *Solid State Ionics.* 1990, 40-41 388-393.
15. Mogensen, M.; Skaarup, S. *Solid State Ionics.* **1996**, 86-88, 1151-1160.

16. Fleig, J.; Baumann, F. S.; Brichzin, V.; Kim, H. R.; Jamnik. J.; Cristiani, G.; Habermeier, H. U.; Maier, J. *Fuel Cells.* **2006**, 6, 284-292.
17. Schuster, M.; Kreuer, K. D.; Andersen, H. T.; Maier, J. *Macromolecules.* **2007**, 40 598-607.
18. Kreuer, K. D. *Solid State Ionics.* **1999**, 125, 285-302.
19. Norby, T. *Solid State Ionics.* **1999**, 125, 1-11.
20. Alberti, G.; Casciola, M. *Solid State Ionics.* **2001**, 145, 3-16.
21. Kreuer, K. D. *J. Memb. Sci.* **2001**, 185 29-39.
22. Conway, B. E. *Electrochemical Supercapacitors: Scientific Fundamentals and Technological Applications*; Kluwer Academic/Plenum publisher: New York, 1999.
23. Burke, A.; Miller, M. *Supercapacitor Technology—Present and Future Advanced Capacitor World Summit 2006*; *CA*: *San Diego*, 2006.
24. Nernst, W. *Z. Electrochem.*, **1899**, 6, 41-43.
25. Kiukkola, K.; Wagner, C. *J. Electrochem. Soc.* **1957**, 104, 308-379.
26. Kiukkola, K.; Wagner, C. *J. Electrochem. Soc.* **1957**, 104, 379-387.
27. Binder, H.; Köhling, A.; Richter, K.; Sandstede, G. *Electrochim. Acta.* **1963**, 8, 781-793.
28. Fischer, W.; Kleinschmager, H.; Rohr, H. J.; Steiner, R.; Eysel, H. H. *Chem -Ing. -Tech.* **1971**, 43, 1227-1232.
29. Fischer, W.; Kleinschmager, H.; Rohr, H. J.; Steiner, R.; Eysel, H. H. *Chem -Ing. -Tech.* **1972**, 44, 726-732.
30. Weissbart, J.; Ruka, R. *Rev. Sci. Instrum.* **1961**, 32, 593-595.
31. Takahashi, T.; Yamamoto, O. *J. Appl. Electrochem.* **1973**, 3. 129-135.

32. Rebollo, E.; Mortalò, C.; Escolástico, S.; Boldrini, S.; Barion, S.; Serra, J. M.; Fabrizio, M. *Energy Environ. Sci.* **2015**, 8, 3675-3686.

33. Verbraeken, M. C.; Cheung, C.; Suard, E.; Irvine, J. T. S. *Nature Mater*. **2014**, 14, 95-100.

34. Kobayashi, G.; Hinuma, Y.; Matsuoka, S.; Watanabe, A. *Science*, **2016**, 351, 1314-1317.

35. Strukov, D. B.; Snider, G. S.; Gregory, S. Stewart, D. R.; Williams, S. R. *Nature*. **2008**, 453, 80-83.

36. Pickett, M. D.; Strukov, D. B.; Borghetti, J. L.; Yang, J. J.; Snider, G. S.; Stewart, D. R.; Williams, R. S. *J. Appl. Phys.* **2009**, 106, 074508.

37. Wedig, A.; Luebben, M.; Cho, D. Y.; Moors, M.; Skaja, K.; Rana, V.; Hasegawa, T.; Adepalli, K. K.; Waser, R.; Valov, I. *Nature nanotech*. **2016**, 11, 67-74.

38. Alibart, F.; Gao, L.; Hoskins, B. D.; Strukov, D. B. *Nanotechnology*. 2012, 23, 075201.

39. Waser, R.; Aono, M. *Nature Mater*. **2007**, 6, 833-840.

40. Wagner, C. *Z. Electrochem.* **1956**, 60, 4.

41. Hebb, M. H. *J. Chem. Phys.* **1952**, 20, 185-190.

42. Yokota, I. *J. Phys. Soc. Japan*, **1961**, 16, 2213-2223.

43. Terabe, K.; Haegawa, T.; Nakayama, T.; Aono, M. *Nature*. **2005**, 433, 47-50.

44. Tennakone, K.; Kumura, G. R. R. A.; Kottegoda, I. R. M.; Wijayantha, K. G. U.; Perera, V. P. S. *J. Phys. D: Appl. Phys.* **1998**, 31, 1492-1496.

45. Warburg, E. *Wiedemann Ann. Phys*. **1884**, 21, 622-646.

46. Warburg, E.; Tegetmeier, F.; *Wiedemann Ann. Phys*. **1888**, 32, 455

47. Haber, F.; Tolloczko, A. *Z. Anorg. Chem.* **1904**, 41, 407-441.

48. Joffé, A. L. *Ann. Phys. (Leipzig)* **1923**, 72, 461-500.

49. Frenkel, J. *Z. Phys.* **1926**, 35, 652-669.

50. Wagner, C.; Schottky, W. *Z. Phys. Chem.* **1930**, B11, 163-210.

51. Schottky, W. *Z. Phys. Chem*. **1935**, B29, 335-355.

52. Wagner, C. *Z. Phys. Chem.* **1933**, B21, 25-41.

53. 工藤徹一，笛木和雄；固体アイオニクス，講談社サイエンティフィク，1991

54. Yang, J.; Molouk, A. F. S.; Okanishi, T.; Muroyama, H.; Matsui, T.; Eguchi, K. *ACS Appl.Mater.Interfaces*. **2015**, 7, 7406-7412.

55. Mohri, M.; Yanagisawa, N.; Tajima, Y.; Tanaka, H.; Mitate, T.; Nakajima, S.; Yoshida, M.; Yoshimoto, Y.; Suzuki, T.; Wada, H. *J. Power Sources.* **1989**, 26, 545-551.

56. Lin, Y.; Ran, R.; Guo, Y.; Zhou, W.; Cai, R.; Wang, J.; Shao, Z. *Int. J. Hydrogen Energy,* **2010**, 35, 2637-2642.

57. Aoki, Y.; Kobayashi, S.; Yamaguchi, T.; Tsuji, E.; Habazaki, H.;Yashiro, K.; Kawada, T.; Ohtsuka, T. *J. Phys Chem. C.* **2016**, 120, 15975-15985.

58. Kamaya, N.; Yamakawa, Y.; Hirayama, M.; Kanno, R.; Yonemura, M.; Kamiyama, T.; Kato, Y.; Kawamoto, K.; Mitsui, A. *Nature Materials*. **2011**, 10, 682-686.

59. Kato, Y.; Hori, S.; Saito, T.; Suzuki, K.; Hirayama, M.; Mitsui, A.; Yonemura, M.; Iba, H.; Kanno, R. *Nature Energy*, **2016**, 1, 16030.

60. Park, M.; Zhanga, X.; Chunga, M.; Lessa, G. B.; Sastry, A. M. *J. Power. Sources*. **2010**, 195, 7904-7929.

61. Nagaura, T.; Tazawa, K. *Prog. Batteries Sol. Cells.* **1990**, 9, 20-25.

62. Rana, J.; Glatthaar, S.; Gesswein, H.; Sharma, N.; Binder, J. R.; Chernikov, R.; Schumacher, G.; Banhart, J. *J. Power Sources.* **2014**, 255, 439-449.

63. Manthiram, A.; Chemelewski K.; Lee, E. S. *Energy Environ Sci.* **2014**, 7, 1339-1350.

64. Qu, J.; Wang, W.; Cheng, J.; Zhang, S.; Ding, J.; Yuan, N. *Int. J. Electrochem. Soc.* **2016**, 11, 10320-10328.

65. Eames, C.; Frost, J. M.; Barnes, P. R. F.; O'Regan, B. C.; Walsh, A.; Saiful, M. *Nature Commun*. **2015**, 6,8497.

66. Stranks, S. M.; Eperon, G. E.; Grancini, G.; Menelaou, C.; Alcocer, M. J. P. Leijtens, T.; Herz, L. M.; Petrozza, A.; Snaith H. J. *Science*, **2013**, 18, 341-344.

67. Geng, W.; Tong, C. J.; Liu, J.; Zhu, W.; Lau, W. M.; Liu, L. M. *Scientific Reports*, **2016**, 6, 20131.

68. Etgar, L.; Gao, P.; Xue, Z.; Peng, Q.; Chandiran, A. K.; Liu, B.; Nazeerudding, M. L.; Gratzel, M. *J. Am. Chem. Soc*. **2012**, 134, 17396-17399.

69. Tubandt, C.; Leitfähigkeit and Überführungszahlen in festen Elektrolyten. In: *Handbuch der Experimentalphysik.*; Akademische Verlagsgesell schaft: 1932. p. 383-469.

70. Koyama, M.; Wen, C.; Masuyama, T.; Otomo, J.; Fukunaga, H.; Yamada, K.; Eguchi, K.; Takahashi, H. *J. Electrochem. Soc.* **2001**, 148, A795-A801.

71. Yang, J.; Molouk, A. F. S.; Okanishi, T.; Muroyama, H.; Matsui, T.; Eguchi, K. *ACS Appl.Mater.Interfaces*. **2015**, 7, 7406-7412.

72. Simner, S.P.; Anderson M. D.; Engelhard, M.H.; Stevenson, J. W. *Electrochem Solid-State Lett.* **2006**, 9, A478-A481.

73. Digiuseppe, G.; Sun, L. *J. Hydrogen Energy.* **2011**, 36, 5076-5087.

74. West, A. R.; *Solid State Chemistry and its applications, 2nd edition, student edition*.; Willey: 2014.

75. Zhou, Y.; Guan, X.; Zhou, H.; Ramaoss, K.; Adam, S.; Liu, H.; Lee, S.; Shi, J. Tsuchikawa, M.; Fong, D. D.; Ramanathan, S. *Nature*, **2016**, 534, 231-234.

76. Goutenoire, F.; Isnard, O.; Retoux, R.; Lacorre, P. *Chem. Mater*. **2000**, 12, 2575-2580.

77. Marozau, I. P.; Marrero-López, D.; Shaula, A. L.; Kharton, V. V.; Tsipis, E. V.; Núñez, P. Frade, J. R. *Electrochim Acta*, **2004**, 49, 3517-3524.

78. Maier, J. *Nature Mater*. **2005**, 4, 805-815.

79. Maier, J. *Z. Phys. Chem*. **2003**, 217, 415.

80. Liang, C. C. *J. Electrochem. Soc.* **1973**, 120, 1289-1292.

81. Sata, N.; Eberman, K.; Eberl, K.; Maier, J. *Nature.* **2000**, 408, 946-949.

82. Garcia-Barriocanal, J.; Rivera-Calzada, A.; Sefrioui, Z.; Iborra, E.; Leon, C.; Pennycook, S. J.; Santamaria, J. **2008**, *Science*, 321, 676-680.

83. Tang, Z. Z.; Hsieh, J. H.; Zhang, S. Y.; Li, C.; Fu, Y. Q. *Surf. Coat. Tech.* **2005**, 198, 110-113.

84. Suhail, M. H.; Rao, G. M.; Mohan, S. *J. Appl. Phys*. **1992**, 71, 1421.

85. Vasu, K.; Krishna, M. G.; Padmanabhan, K. A. *Appl. Sur. Sci*. **2011**, 257, 3069-3074.

86. 和佐清孝，早川茂；薄膜化技術(第 3 版)，共立出版，2002.

87. Chua, L.; Kang, S. M. *Proc. IEEE*. **1976**, 64, 209-223.

88. Gao, X.; Xia, Y.; Ji, J.; Xu, H.; Su, Y.; Li, H.; Yang, C.; Guo, H.; Yin, J.; Liu, Z. *Appl. Phys. Lett.* **2010**, 97, 193501.

89. Strukov, D. B.; Borghetti, J. L.; Williams, R. S. *Small* **2009**, 5, 1058-1063.

90. Rosenstock, Z.; Feldman, I.; Gil, Y.; Riess, I. *J. Electroceram. Soc.* **2005**, 14, 205–

212.

91. Gil, Y.; Umurhan, O. M..; Tsur, Y.; Riess, I. *Solid State Ionics* **2008**, 179, 24-32.

92. Meyer, R.; Liedtke, R.; Waser, R. *Appl. Phys. Lett*. **2005**, 86, 112904.

93. Nian, Y. B.; Strozier, J.; Wu, N. J.; Chen, X.; Ignatiev, A. *Phys. Rev. Lett.* **2007**, 98, 146403.

94. Rozenberg, M. J.; Sánchez, M.; Weht, R.; Acha, C.; Gimez-Marlasza, F.; Levy, P. *Phys. Rev. B* 2010, 81, 115101.

95. Meyer, R. et al. in IEEE Proceed NVMTS2008 (Oxide Dual-Layer Memory Element for Scalable Non-Volatile Cross-Point Memory Technology) 1–5 (PacificGrove, CA, USA, 2008).

96. Aoki, Y.; Wiemann, C.; Feyer, V.; Kim, H. S.; Schneider, C. M.; Yoo, H. I.; Martin, M. *Nature Commun.* **2014**, 5, 3473.

97. Adams, B. D.; Chen, A. *Mater. Today*. **2011**, 14, 282-289.

98. Cornaglia, L.; Múnera, J.; Lombardo, E. *Int. J. Hydrogen Energy*. **2015**, 40, 3423-3437.

99. Ito, N.; Iijima, M.; Kimura, K.; Iguchi, S. *J. Power Sources*, **2005**, 152, 200-203.

100. Ito, N.; Aoyama, S.; Matsui, T.; Matsumoto, S.; Matsumoto, H.; Ishihara, T. *J. Power Sources*, **2008**, 185, 922-926.

101. Aoki, Y.; Kobayashi, S.; Yamaguchi, T.; Tsuji, E.; Habazaki, H.; Yashiro, K.; Kawada, T.; Ohtsuka, T. *J. Phys. Chem. C*, **2016**, 120, 15976-15985.

102. Aoki, Y.; Yamaguchi, T.; Kobayashi, S.; Zhu, C.; Habazaki, H. *J. Electrochem. Soc.* **2017**, 164, F577-F581.

103. Oishi, M.; Akoshima, S.; Yashiro, K.; Sato, K.; Mizusaki, J.; Kawada, T. Solid State

Ionics. 2009, 180, 127-131.

104. Oishi, M.; Akoshima, S.; Yashiro, K.; Sato, K.; Mizusaki, J.; Kawada, T. Solid State Ionics. 2008, 179, 2240-2247.

105. Barison, S.; Battagliarin, M.; Cavallin, T.; Doubova, L.; Fabrizio, M.; Mortalò, C.; Boldrini, S.; Malavasi L.; Gerbasi, R. *J. Mater. Chem.* **2008**, 18, 5120-5128.

106. Ryu, K. H.; Haile, S. M. *Solid State Ionics*. **1999**, 125, 355-367.

107. Matsumoto, H.; Shimura, T.; Higuchi, T.; Tanaka, H.; Katahira, K.; Otake, T.; Kudo, T.; Yashiro, K.; Kaimai, A.; Kawada, T.; Mizusaki, J. *J. Electrochem. Soc.* **2005**, 152, A488-A492.

108. Song, S.; Wachsman, E. D.; Rhodes, J.; Dorris, S. E.; Balachandran, U. *Solid State Ionics*, **2004**, 167, 99-105.

109. Zhu, Z.; Sun, W.; Dong, Y.; Wang, Z.; Shi, Z.; Zhang, Q.; Liu, W. *Int. J. Hydrogen. Energy*. **2014**, 39, 11683-11621.

110. Nozaki, T.; Hatano, Y. *Int. J. Hydrogen. Energy*. **2013**, 38, 11983-11987.

111. Nozaki, T.; Hatano, Y.; Yamakawa, E.; Hachikawa, A.; Ichinose, K. *Int. J. Hydrogen. Energy*. **2010**, 35, 12454-12460.

112. Gringoz, A.; Glandut, N.; Valette, S. *Electrochem. Commun.* **2009**, 11, 2044-2047.

113. Van De Walle, C. G. *Nature*. **2003**, 423, 626-628.

114. Fujii, R.; Gotoh, Y.; Liao, M. Y.; Tsuji, H.; Ishikawa, J. *Vacuum*, **2006**, 80, 832.

115. Gotoh, Y.; Tsuji, H.; Ishikawa, J. *J. Vac. Sci. Technol. B.* **2003**, 21, 1607.

116. Oishi, M.; Akoshima, S.; Yashiro, K.; Sato, K.; Mizusaki, J.; Kawada, T. Solid State Ionics. 2009, 180, 127-131.

117. Oishi, M.; Akoshima, S.; Yashiro, K.; Sato, K.; Mizusaki, J.; Kawada, T. Solid State

Ionics. 2008, 179, 2240-2247.

118. Barison, S.; Battagliarin, M.; Cavallin, T.; Doubova, L.; Fabrizio, M.; Mortalò, C.; Boldrini, S.; Malavasi L.; Gerbasi, R. *J. Mater. Chem.* **2008**, 18, 5120-5128.

119. Ryu, K. H.; Haile, S. M. *Solid State Ionics*. **1999**, 125, 355-367.

120. Matsumoto, H.; Shimura, T.; Higuchi, T.; Tanaka, H.; Katahira, K.; Otake, T.; Kudo, T.; Yashiro, K.; Kaimai, A.; Kawada, T.; Mizusaki, J. *J. Electrochem. Soc.* **2005**, 152, A488-A492.

121. K. D. Kreuer, *Annu. Rev. Mater. Res.*2003, 33, 333-359.

122. Al-Mufachi, N. A.; Rees, N. V.; Steinberger-Wilkens, R. *Renew. Sustain. Energy. Rev*. **2015**, 47, 540-551.

123. Luo, W.; Ishikawa, K.; Aoki, K. *J. Alloys. Compd.* **2006**, 407, 115-117.

124. Hashi, K.; Ishikawa, K.; Matsuda, T.; Aoki, K. *J. Alloys. Compd.* **2006**, 425, 284-290.

Chapter 2

Development of resistive switching gallium oxide thin film with tailoring gallium valence state and oxygen deficiency

2-1 Introduction

As the potential next generation for nonvolatile memory, resistive random access memory (RRAM) with a simple metal/oxide/metal sandwich structure has been studied intensively during the past decades.[1-2] In case of the well-established Pt/TiO_2/Pt memristor devices, the switching between high resistance state (HRS) and low resistance state (LRS) is triggered by the modification of the tunnel barrier width between a top electrode (TE) and the preformed conductive filament due to the ionic drift within a few nanometer-thick space charge layer in vicinity of the interface with electrode within sub-μs time scale.[3-11]

Gallium oxide devices are considered as one of ideal candidates for RRAM because of its intrinsic high resistance characteristic and extraordinarily sensitive conductivity to the oxygen concentration.[12-20] In a previous study, Aoki et al. found resistive switching in highly-nonstoichiometric, amorphous gallium oxide thin films, *a*-$GaO_{1.1}$ was originated from the bulk mixed oxide ion-electron conductivity.[19] The homogeneous migration of oxygen vacancy donors modify the electronic carrier distribution across

films and thus resistance states of film bulk varies by applied fields.[19] Such a bulk-conduction mechanism memristor could realize multilevel states of resistance and a large on/off current ratio due to the continuous tunability of the internal state variable, and therefore is expected to be a dynamical memristor system to emulate synaptic memory behaviour.[21,22] To develop feasible homogeneous resistive switching devices for future neuromorphic application, it is beneficial to design amorphous gallium oxides with enhanced ion conductivity. The oxide ion conductivity of *a*-GaO_x must be related with interstitial spaces and local Ga environments of the mixed valence state Ga(III)-Ga(I) amorphous oxide. Therefore, it is of fundamental and of technological importance to develop the precise fabrication process with tailoring the oxygen deficiency, namely, Ga(I) fractions in the oxide matrices in order to tune the resistive switching properties of film devices.

Highly-nonstoichiometric amorphous GaO_x thin films have been fabricated by pulse laser deposition (PLD) with a Ga_2O_3 target under low p_{O2} conditions.[12,19,20] Unfortunately, it is difficult to control the yields of Ga(I) suboxides by the method because Ga_2O_3 is not easily reduced under extremely low O_2 pressure at elevated temperature.[23] Lee et al. reported the fabrication of oxygen deficient gallium oxide films by high temperature vacuum annealing of Ga_2O_3/Cr/Ga_2O_3 three-layer laminates.[13] Gallium oxide is efficiently reduced through the interdiffusion reaction because of relatively large negative energy of Cr-O bonding (-1053 kJ mol^{-1}) in comparison to Ga-O bonding (-998.3 kJ mol^{-1}).[24] Such a redox reaction must be useful to prepare the Ga(I)-Ga(III) mixed valence gallium oxide. Herein, we successfully fabricated Cr-doped gallium oxide films with a controlled amount of Ga(I) and oxygen deficiency by depositing a homogeneous mixture

of Ga(III) oxide moieties and Cr(0) metal atoms. The chromium atoms scavenge the oxygen atoms of Ga(III) oxide moieties and thus Ga(I)-Ga(III) mixed valence state homogeneous amorphous oxide was prepared. The films with optimal amount of Ga(I) fractions revealed remarkable bulk resistive switching with large on/off ratio according to the efficient oxide ion conductivity, which enables incremental change of the bulk resistance state by increasing bias duration or applied short pulse numbers. The switching behavior was compared to the well-established TiO_x thin film base filamentary mechanism switching devices.

2-2 Experimental

A 20 nm-thick Pt deposited Si wafer (100) was used as a bottom electrode (BE). Nonstoichiometric TiO_x and Cr-doped GaO_x thin films were deposited on a Pt BE by rf sputtering at room temperature. TiO_x thin films were deposited by using a Ti target (purity: 99.9%) in a mixed argon and oxygen atmosphere (the ratio of Ar/O_2 was 5:1) at a total pressure of 0.4 Pa at substrate temperature of 150°C. Cr-doped GaO_x films (Cr-GaO_x) were deposited by cosputtering with Ga_2O_3 and Cr targets in pure argon atmosphere at a pressure of 1 Pa. The sputtering power of Ga_2O_3 was fixed at 50 W and that of Cr was adjusted at 30, 40, 60 and 70 W in order to change Ga/Cr molar ration in the resultant film. The substrate was kept at ambient temperature. Circular metal top electrodes (TE) with a diameter of 100-800 μm and a thickness of 50 nm were sputter-deposited on the films through a metal shadow mask. The *I-V* characteristics of the

devices were measured at room temperature using source-measure units (KEITHLEY 2601B). In all cases, Pt TE is firstly swept from 0 V to anodic region (+ 1 V), swept back to cathodic region (-1 V) and returned to 0 V so as to complete one cycle of voltage sweep. The voltage steps are fixed at 0.1 V (Fig. 2-1).

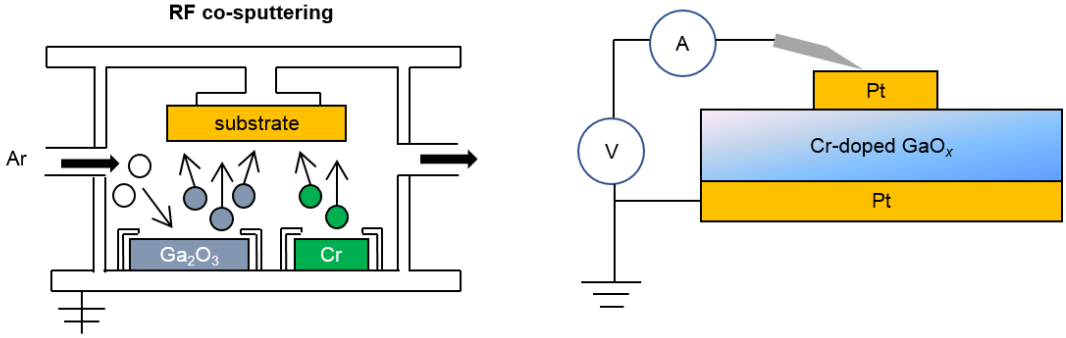


Fig. 2-1 schematic illustration of (a) RF co-sputtering and (b) Cr-doped GaO_x device.

The chemical composition of Cr-GaO_x films was examined by wave-length dispersive X-ray analysis (WDX) with a JEOL JXA-8530F. For WDX measurements, 800 nm-thick films were deposited on the Pt/Si wafer by sputtering under the same atmospheric, rf power and temperature conditions as those for the corresponding switching device films. The cross-sectional transmission electron microscopy (TEM) and energy dispersive X-ray fluorescent analysis (EDX) were carried out in a HITACHI HD-2000. The specimens for TEM observation were prepared by a focused ion beam microfabrication (FIB; HITACHI FB-2100). X-ray photoelectron spectroscopy (XPS) was carried out in JEOL JPS-9010MC with Mg Kα radiation. The depth profile was applied by *in situ* Ar^+ ion sputtering. The curve fitting was carried out with Lorenz-Gaussian function.

2-3 Results

Firstly, GaO_x films are fabricated by sputtering a single Ga_2O_3 target. The resulting films are transparent, indicating amount of oxygen deficiency in the film is quite small. On the other hand, the uniform, dark-colored thin film can be obtained by cosputtering of Cr and Ga_2O_3. The chemical composition of the films deposited with a Cr sputtering power of 30, 40, 60 and 70 W is $Ga_{0.96\pm0.02}Cr_{0.04\pm0.02}O_{1.4\pm0.1}$, $Ga_{0.91\pm0.04}Cr_{0.09\pm0.05}O_{1.3\pm0.1}$, $Ga_{0.82\pm0.2}Cr_{0.18\pm0.02}O_{1.2\pm0.1}$ and $Ga_{0.78\pm0.06}Cr_{0.22\pm0.03}O_{1.2\pm0.1}$ respectively, as determined by WDX measurements (Table 2-1). These films are hereafter called as Ga96Cr4, Ga91Cr9, Ga82Cr18 and Ga78Cr22, respectively, based on the average metal composition. Fig. 2-2(a) shows cross-sectional TEM of Ga82Cr18 thin films. The densely-packed films (120 nm thickness) are uniformly formed over a wide area of a Pt/Si wafer substrate. Apparent pinholes and clacks are not observed. STEM-EDX shows chromium is homogeneously distributed throughout the film bulk (Fig. 2-2(c-d)) without segregation, indicating homogeneous mixtures of chromium and gallium oxide are prepared by the cosputtering. The Ga82Cr18 thin films show only a halo ring, indicating an amorphous phase (Fig. 2-2(b)).

Fig. 2-3 shows Ga 3*d* and Cr 2*p* XPS spectra of 120 nm-thick Cr-GaO_x thin films. In all cases, Ga 3*d* peak is deconvoluted into two peaks; a peak at 20.7 eV due to the Ga(III) state and a peak at 19.6 eV due to Ga(I) state (Fig. 2-3(a)).[19,25,26] Ga(III)/Ga(I) molar

ratios in Ga96Cr4, Ga91Cr9, Ga82Cr18 and Ga78Cr22 are 90/10, 77/23, 69/31 and 64/36, respectively (Table 2-1). These values of the molar ratios are consistent with ones calculated from chemical composition by accounting charge compensation between cations (Ga^{3+}, Ga^{+} and Cr^{3+}) and anion (O^{2-}). On the other hand, Cr 2*p* XPS spectral features are not changed by chemical composition (Fig. 2-3(b)). All films reveal apparent spectral feature of Cr(III) with Cr $2p_{1/2}$ and $2p_{3/2}$ peaks at 587.5 eV and 577 eV, respectively[27] while the features of lower valence state Cr, such as Cr(0) (574.2 eV of $2p_{3/2}$)[16] and Cr(I) (576.3 eV of $2p_{3/2}$)[28] does not appear (Fig. 2-3(b)).

Ga 3*d* XPS spectra of Ga82Cr18 were also measured in the depth of about 50 nm (middle) and 100 nm (near bottom edge) by Ar^{+} ion milling (Fig. 2-3(c)). The spectra show similar features at any depths (Fig. 2-3(c)), indicating Ga(I) states are homogeneously distributed through film.

Guo et al. reported the switching properties of *a*-$GaO_{1.2}$ thin film device are strongly dependent on the electrode materials.[12] Pt is used as a top electrode material in this study in order to avoid oxidation of electrode by contacting with the oxide films.

Resistive switching behavior of Cr-GaO_x films is strongly dependent on the composition (Fig. 2-4). The Ga96Cr4 thin films give two orders of magnitude smaller current than those of other composition and the hysteretic *I*-*V* curves do not appear at any sweep rates (Fig. 2-4(a)). The others, Ga91Cr9, Ga82Cr18 and Ga78Cr22, involves resistive switching at a sweep rate of 1 and 0.01 V s^{-1} (Fig. 2-4(b-d)), revealing a pinched

hysteresis *I-V* loop in counter eight-figure clockwised polarity when the voltage on TE was swept in the way of 0→+1→0→-1→0 V in every composition (Fig. 2-4). A positive voltage RESET the film from the low resistance state (LRS) to the high resistance state (HRS), and with negative bias the film SET to the LRS, indicating bipolar resistive switching behavior of the films. Electroforming process by applying high voltage is not required to initiate the switching. These results are consistent with the previous studies of *a*-$GaO_{1.1}$ thin film devices.[12,19]

The hysteretic shape of *I-V* curves is strongly dependent on the voltage sweep rate, see e.g. Fig. 2-4(b-d). The films do not reveal hysteresis loops at fast sweep rate (100 V s^{-1}) but tend to reveal wider hysteretic loops at slower rate. The switching behavior is stationary and is not decayed for a few 10's voltage sweep cycles.

The Ga82Cr18 thin film is distinct from other composition films. The films reveal the large hysteresis loop at a sweep rate of 1 and 0.01 V s^{-1} and possess the highest HRS/LRS resistance ratio (on/off ratio) which is about 20 at 0.7 V (Fig. 2-5(a)). The ratios decrease to about 2 if Cr dopant concentrations, namely, Ga(I) fractions are decreased or increased as Ga91Cr9 or Ga78Cr22, respectively.

The area dependence of current level in Ga82Cr18 film shows linear scaling (Fig. 2-5(b)). This feature discloses that the resistance state of the film below TE is homogeneously changed by responding to applied field or a number of conducting filaments are uniformly distributed over the electrode area.

In a separate experiment, Pt/TiO_x/Pt thin film devices were fabricated by the similar sputtering deposition processes as reported elsewhere.[29,30] Rutile-type TiO_x thin films with a 100-nm thickness was uniformly formed on Pt electrode, as confirmed by TEM and ED patterns (Fig. 2-6(a)). The TiO_x thin film prepared here reveal the similar switching behavior as the filamentary mechanism switching TiO_x devices reported previously.[3-11] *I-V* hysteretic shape is not varied by decreasing the voltage sweep rate (Fig. 2-6(b)) in the range of less than 100 V s^{-1}. The current level is independent on Pt TE area (Fig. 2-5(b)). This is peculiar to the resistive switching triggered by variation of local states such as formation and deformation of the conductive filament.

It is evident that resistive switching of Cr-GaO_x is quite different from TiO_x. The strongly time-dependent switching events and area dependent current level is incompatible with the filamentary mechanism as operating in TiO_x devices. It is concluded the resistive switching of Cr-GaO_x films is driven by variation of bulk states.[19,31]

The bulk switching mechanism suggests the film resistance can be incrementally adjusted by tuning the duration and sequence of the applied bias.[32] Unlike the devices with abrupt switching characteristics where the programming bias control the final device state,[33,34] each programming pulse controls the relative change of the film resistance in case of Cr-GaO_x devices because donor concentration profiles across film can be varied sequentially by the migration at each programing bias. Fig. 2-7 shows the resistance state change of Ga82Cr18 films when a series of 70 identical negative (-0.95 V, 500 μs) pulses

was applied on the films, followed by a series of 70 identical positive voltage pulses (0.95 V, 500 μs). The large pulse bias (namely -0.95 V or 0.95 V) programs the resistance state of the films and a small read bias of 0.1 V measures a response current to represent the resistance state. As expected from the DC characteristics of the device, the application of negative voltage pulses (-0.95 V) incrementally decreases the film resistance, and the application of positive voltage pulses (+0.95 V) incrementally increases the resistance.

Table 2-1 List of the sputtering power of Cr for Cr-Ga_2O_3 cosputtering deposition and composition and Ga(III) /Ga(I) molar ratios of the corresponding Cr-GaO_x thin films.

Rf power / W	**Name**	**Composition** [#]	**Ga(III) / Ga(I)**[ϒ]	**Ga(III) /Ga(I)**[∀]
70W	Ga78Cr22	$Ga_{0.78\pm0.06}Cr_{0.22\pm0.03}O_{1.2\pm0.1}$	61/39	58/42
60 W	Ga82Cr18	$Ga_{0.82\pm0.2}Cr_{0.18\pm0.02}O_{1.2\pm0.1}$	69/31	67/33
40 W	Ga91Cr9	$Ga_{0.91\pm0.04}Cr_{0.09\pm0.05}O_{1.3\pm0.1}$	77/23	85/15
30 W	Ga96Cr4	$Ga_{0.96\pm0.02}Cr_{0.04\pm0.02}O_{1.4\pm0.1}$	90/10	93/7

determined by WDX. ϒ determined by XPS. ∀ calculated by Eq. (2-3).

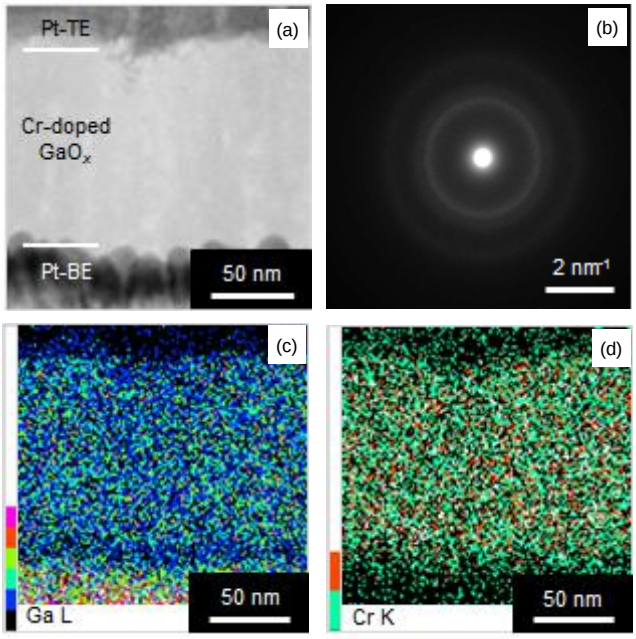


Fig. 2-2 (a) Cross-section TEM image and (b) ED pattern of Ga82Cr18 thin films. Corresponding elemental EDX mapping of (c) Ga and (d) Cr.

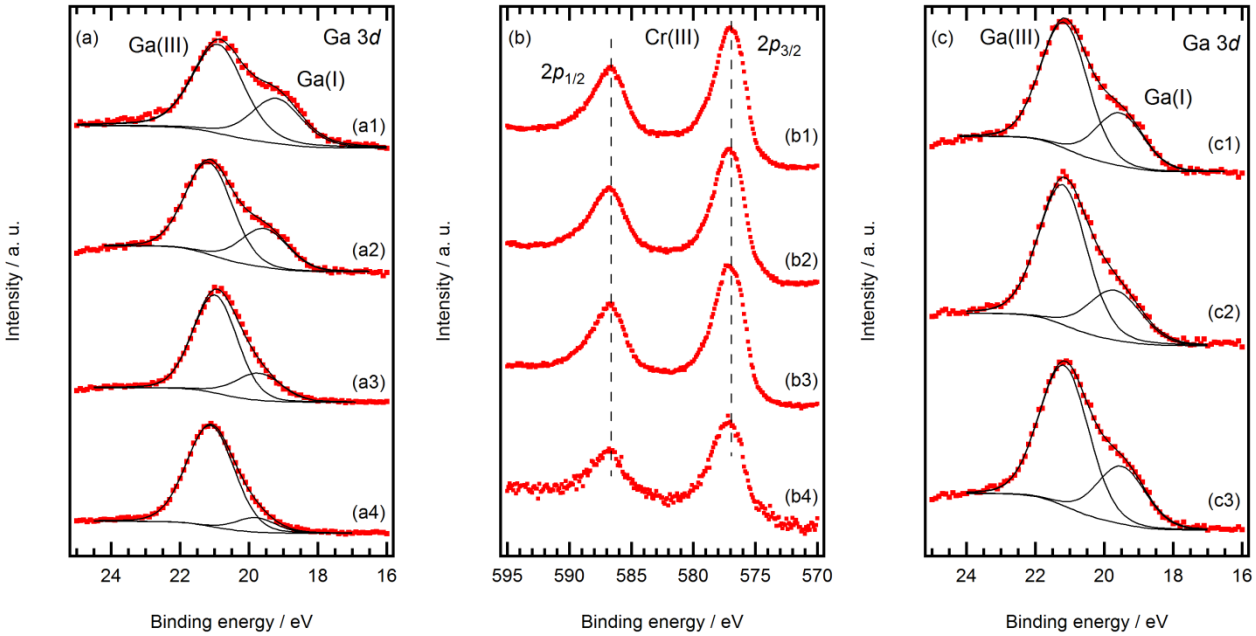


Fig. 2-3 (a) Ga 3d and (b) Cr 2*p* XPS spectra of 120 nm-thick thin films of (a1&b1) Ga78Cr22, (a2&b2) Ga82Cr18, (a3&b3) Ga91Cr9 and (a4&b4) Ga96Cr4. (c) Ga 3*d* XPS depth profile of 120 nm-thick Ga82Cr18 thin films. The spectra were stored at the surface (c1) and at the points in 60 nm (c2) and 100 nm depth (c3). Red dots are the observed and black lines the simulated.

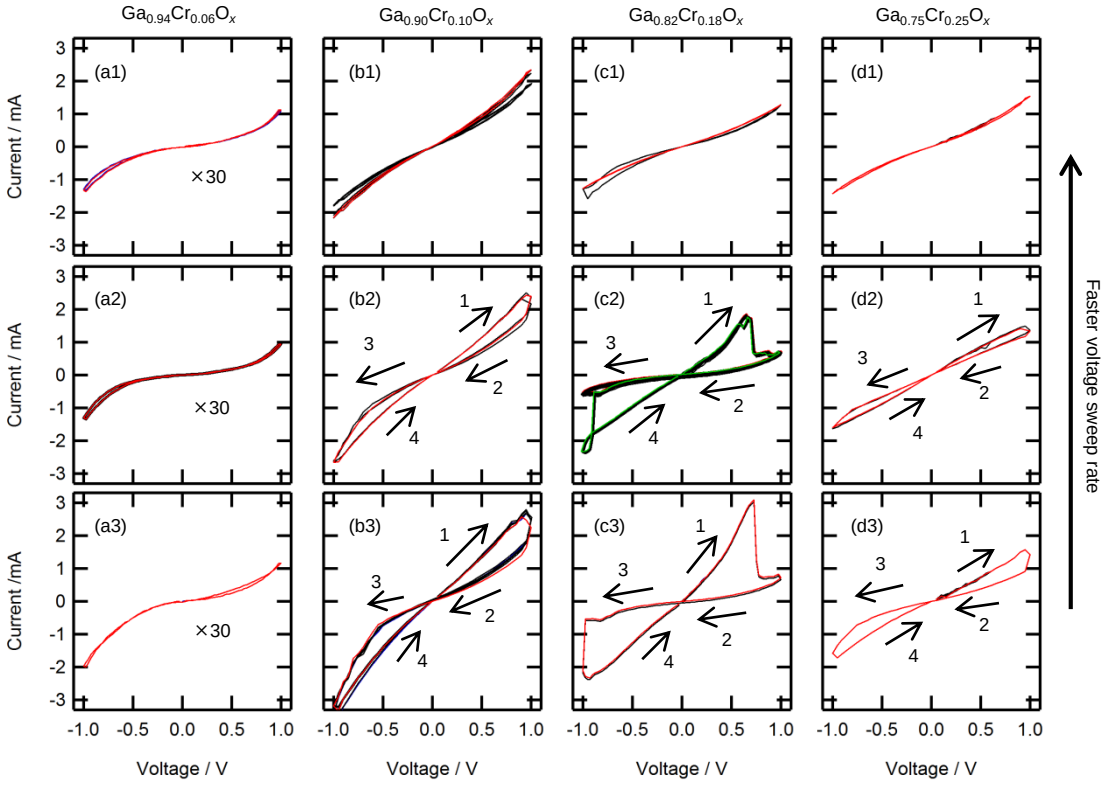


Fig. 2-4 *I-V* characteristics of Pt(TE)/Cr-GaO_x film/Pt(BE) devices thickness during a repeated voltage sweep cycle of 0 → +1 → -1 → 0 V at different voltage sweep rates. (a1)-(a3) Ga92Cr4, (b1)-(b3) Ga91Cr9, (c1)-(c3) Ga82Cr18 and (d1)-(d3) Ga78Cr22 thin films with 120 nm thickness. The sweep rate is 100 V s^{-1} in (a1), (b1), (c1) and (d1), 1 V s^{-1} in (a2), (b2), (c2) and (d2) and 0.01 V s^{-1} in (a3), (b3), (c3) and (d3). The cycles are repeated 20 time in (c2) and 10 time in others. The numbered arrows indicate the direction of the switching cycles (counter-figure-eight loops). 1st, 10th and 20th curves are shown by blue, red and green, respectively. The curves of other cycles are shown by black. The current levels in (a1)-(a3) are multiplied by 30.

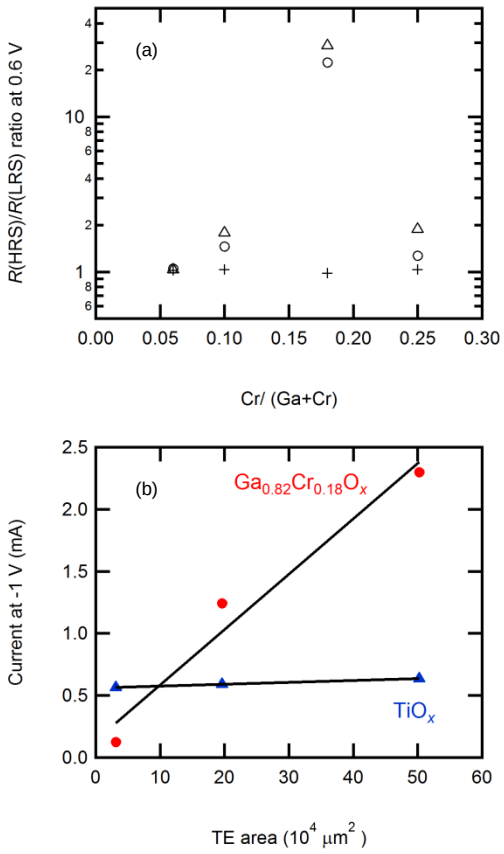


Fig. 2-5 (a) On/Off switching ratio vs Cr content at 0.7 V, measured at a voltage sweep rate of 100(+), 1(○) and 0.01(△) V s^{-1}. (b) TE area scaling of the current of LRS Ga82Cr18 and TiO_x thin films at -0.5 V.

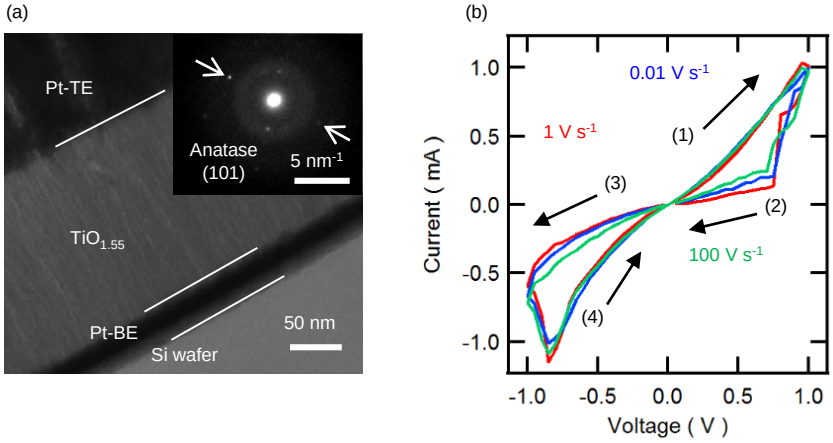


Fig. 2-6 (a) Cross-section TEM image and ED pattern of rutile-type TiO_x thin films. (b) *I-V* characteristics of 100 nm-thick TiO_x thin films, measured at a voltage sweep rate of 100 V s^{-1} (green line), 1 V s^{-1} (red line) and 0.01 V s^{-1} (blue line).

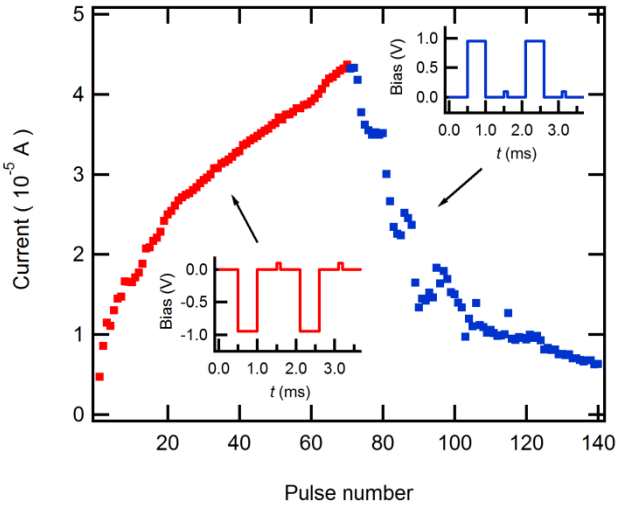


Fig. 2-7 Current response transients of Ga82Cr18 thin films, measured by applying 500 μs programming bias (+0.95 or -0.95 V) and 100 μs read bias (+0.1 V). Red is the current measured at 0.1 V read pulse after programmed by a -0.95 V pulse and blue is the one after programmed by a 0.95 V pulse. The insets show pulse patterns used for the measurements.

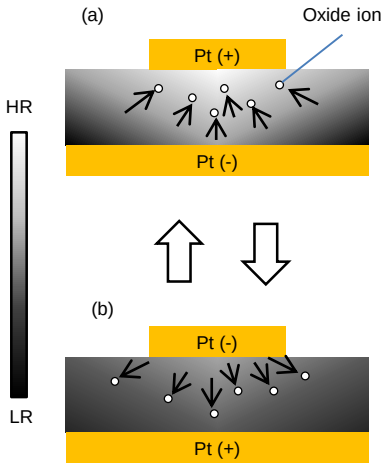


Fig. 2-8 Schematic representation of bulk mechanism resistive switching in Cr-GaO_x thin film devices. (a) Positive bias and (b) negative bias on TE.

2-4 Discussion

It is clear from the results of XPS and STEM-EDX measurements (Fig. 2-2 and Fig. 2-3) that co-sputtered Cr(0) metallic atoms scavenge oxygen from adjacent Ga(III) oxide moieties by the following redox reaction

$$2Cr(0) + 3Ga(III) \rightarrow 2Cr(III) + 3Ga(I) \quad (2\text{-}1)$$

The chemical composition of the resultant film can be given by

$$(1\text{-}x)Ga^{III}O_{1.5} + xCr^{0} \leftrightarrows (Ga^{III}_{1\text{-}y}Ga^{I}_{y})_{1\text{-}x}Cr^{III}_{x}O_{1.5(1\text{-}x)} \quad (2\text{-}2)$$

Then the charge balance yields:

$$y = 1.5x\,(1\text{-}x)^{-1} \quad (2\text{-}3)$$

The reaction (2-3) clarify the amount of oxygen deficiency ($1.5x$) is related to Ga(I) fraction (y). The molar fractions of Ga(I) of the films prepared here are in agreement with the values calculated by reaction (2-3) (Table 2-1). It is apparent that oxygen deficiency is involved by the reaction (2-2) during cosputtering.

The switching performance of Cr-GaO_x thin films is drastically changed by Ga(I) fractions (Fig. 2-4). The schematic model of bulk mechanism switching of gallium oxide base thin films is shown in Fig. 2-8. The positive bias on small area TE accumulates negatively-charged oxide ions in vicinity of TE blocking electrode by extinguishing electron carriers so as to form highly-resistive, oxygen-rich layer near TE as follows (Fig. 2-8(a)).

$$Ga(I)O_{0.5} + 2e' + O \leftrightarrows Ga(III)O_{1.5} \quad (2\text{-}4)$$

The opposite bias can enrich the electron carriers in the layer again by driving oxide ions towards large area BE (Fig. 2-8(b)). At fast voltage sweep rate, the resistance ratio between HRS and LRS, namely the hysteretic width of *I-V* loop tends to be small because the shift of oxygen vacancy donor distribution cannot be largely changed due to the relatively short bias duration. However, the hysteresis becomes wider at slower sweep rate due to the large shift in donor distribution by longer bias duration.

Based on the mechanism, the poor resistive switching performance of low Ga(I) fraction films, such as Ga96Cr4, can be related to the poor oxide ion conductivity because the low oxygen deficiency may not afford sufficient space for the pathway of oxide ion migration. The Cr(III) contents is not beneficial for the oxide ion conduction, since the dissociation of Cr-O bonding require relatively large energy. This might be one of the reasons for the deteriorated switching performance of the high chromium content films, Ga78Cr22 (Fig. 2-4(d)). The current results suggest that the optimal molar fraction of Cr/Ga is nearly 18/82 in the relation to fast oxide ion conduction in highly oxygen deficient glass matrices.

The resistive switching performance of 120 nm-thick Ga82Cr18 thin films is superior to that of the GaO_x films (x = 1.1-1.2) given by PLD in previous studies.[12,19] The former exhibits the on/off ratio of 20 at 0.7 V, however, the ratios of the later is about 2 at the same voltage. These results reveal the oxide glass network of the cosputtered Ga82Cr18

films retain the efficient oxide ion conductivity as much as the PLD films. The Ga82Cr18 film exhibits remarkable multiple resistance states as responding to short pulse biasing (Fig. 2-7), indicating that the significant shift of oxygen vacancy donors for resistance change can be induced by the bias duration of 100's μs.

The oxide ion mobility in M-doped GaO_x thin films may be largely varied by choice of dopant cations as is the case with various ceramic oxide ion conductors.[35,36] Except for chromium, various metals such as Mg, Ti, Al etc. are potential candidates as oxygen scavenging dopant of Ga_2O_3 from the view point of M-O bond formation energy. Recently, Chang et al. reported oxygen-deficient, amorphous WO_x thin film also shows multiple resistive switching probably due to oxide ion conduction.[37,38] This suggests that not only the gallium oxide but also other nonstoichiometric metal oxide systems can be considered as a possible candidate of bulk oxide ion conducting thin films. Most of metals and binary metal oxides can be used as a target material of rf sputtering techniques. It is concluded that the cosputtering with a pair of resistive switching oxides and oxygen scavenging metal dopant affords a strong tool to tune the oxide ion conductivity of the highly-nonstoichiometric, resistive switching metal oxide thin films.

2-5 Conclusion

In summary, the fabrication method of Cr-doped gallium oxide thin films with tailored gallium valence state and oxygen deficiencies has been established, based on the reactive cosputtering with Ga_2O_3 and Cr targets. The Ga(I)-Ga(III) mixed valence state homogeneous oxide glass can be formed from a homogeneous mixture of Cr(0) metal atoms and Ga(III) oxides moieties deposited by cosputtering, because Cr(0) scavenges oxygen of Ga(III) oxide due to the relatively large negative energy of Cr-O bonding in comparison to Ga-O bonding. The Ga82Cr18 thin film with optimal Ga(I) contents can reveal remarkable homogeneous resistance switching due to the efficient bulk oxide ion conduction. The on/off ratio of the film is similar to that of the highly-nonstoichiometric $GaO_{1.1}$ thin films prepared by PLD. The film clearly involves multiple resistance state switching where the final device state is determined by bias history, since the oxygen vacancy donor profiles can be incrementally modified by bias duration or number of the applied short pulse biasing. The current results open up a new way to design the bulk mechanism resistive switching metal oxide thin films with tailored oxide ion conductivity.

2-6 References

1. Strukov, D. B.; Snider, G. S.; Stewart, D. R.; Williams, R. S. *Nature*. **2008**, 453, 80-83.
2. Waser, R.; Dittmann, R.; Staikov, G.; Szot, K. *Adv. Mater.* **2009**, 21, 2632-2663.
3. Yang, J. J.; Pickett, M. D.; Li, X.; Ohlberg, D. A. A.; Stewart D. R.; Williams, R. S. *Nature Nanotechnol.* **2008**, 3, 429-433.
4. Min, K. K.; Seok, J. D.; Seong, H. C. *Nanotechnol.* **2011**, 22, 254002.
5. Kwon, D. H.; Kim, K. M.; Jang, J. H.; Jeon, J. M.; Lee, M. H.; Kim, G. H.; Li, X. S.; Park, G.S.; Lee, B.; Han, S.; Kim, M.; Hwang, C. S. *Naure Nanotechnol.* **2010**, 5, 148-153.
6. Sato, Y.: Kinoshita, K.; Aoki, M.; Sugiyama, Y. *Appl. Phys. Lett.*, 2007, **90**, 033503.
7. Strachen, J. P.; Pickett, M. D.; Yang, J. J.; Aloni, S.; Kilcoyne, A. L. D.; Ribeiro, G. M.; Williams, R. S. *Adv. Mater.* **2010**, 22, 3573-3577.
8. Hur, J. H.; Lee, M.J.; Lee, C. B.; Kim, Y. B.; Kim, C. J. *Phys. Rev. B.* **2010**, 82, 155321.
9. Muenstermann, R.; Menke, T.; Dittmann, R.; Waser, R. *Adv. Mater.* **2010**, 22, 4819-4822.
10. Pickett, M. D.; Strukov, D. B.; Borghetti, J. L.; Yang, J. J.; Snider, G. S.; Stewart, D. R.; Williams, R.S. *J. Appl. Phys.* **2011**, 106, 074508.

11. Alibert, F.; Gao, L.; Hoskins, B. D.; Strukov, D. B. *Nanotechnol.* **2012**, 23, 075201.

12. Gao, X.; Xia, Y.; Ji, J.; Xu, H.; Su, Y.; Li, H.; Yang, C.; Guo, H.; Yin, J.; Liu, Z. *Appl. Phys. Lett.* **2010**, 97, 193501.

13. Lee, D. Y.; Tseng, T. Y. *J. Appl. Phys.* **2010**, 110, 114117.

14. Guo, D. Y.; Wu, Z. P.; An, Y. H.; Li, P. G.; Wang, P. C.; Chu, X. L.; Guo, X. C.; Zhi, Y. S.; Lei, M.; Li, L. H.; Tang, W. H. *Appl. Phys. Lett.* **2015**, 106, 042105.

15. Yan, X. B.; Hao, H.; Chen, Y. F.; Li, Y. C.; Banerjee, W. *Appl. Phys. Lett.* **2014**, 105, 093502.

16. Guo, D. Y.; Wu, Z. P.; Zhang, L. J.; Yang, T.; Hu, Q. R.; Lei, M.; Li, P. G.; Li, L. H.; Tang, W. H. *Appl. Phys. Lett.* **2015**, 107, 032104.

17. Yang, J. B.; Chang, T. C.; Huang, J. J.; Chen, S. C.; Yang, P. C.; Chen, Y. T.; Tseng, H. C.; Sze, S. M.; Chu, A. K.; Tsai, M. J. *Thin Solid Films*. **2013**, 529, 200-204.

18. Hsu, C. W.; Chou, L. J. *Nano Lett.* **2012**, 12, 4247-4253.

19. Aoki, Y.; Wiemann, C.; Fayer, C.; Kim, H. S.; Schneider, C. M.; Yoo, H. I.; Martin, M. *Nature Commun.* **2014**, 5, 4473.

20. Nagarajan, L.; De Souza, R. A.; Samuelis, D.; Valov, I.; Borger, A.; Janek, J.; Becker, K. D.; Schmidt, P. C.; Martin, M. *Nature Mater.* **2008**, 7, 391-398.

21. Yang, J. J.; Strukov, D. B.; Stewart, D. R. *Nature Nanotechnol.* **2013**, 8, 13-24.

22. Chang, T.; Jo, S. H.; Kim.; Sheridan, P.; Gaba, S.; Lu, W. *Appl. Phys. A*. **2011**, 102, 857-863.

23. Kolman, D. G.; Taylor, T. N.; Park, Y. S.; Stan, M.; Butt, D. P.; Maggiore, C. J.; Tesmer, J. R.; Havrille, G. J. *Oxidat. Metal*. **2001**, 56, 347-374.

24. Lide, D. R. *Handbook of Chemistry and Physics, 84th ed.*; CRC Press, 2003.

25. Carli, R.; Bianchi, C. L. *Appl. Surf. Sci.***1994**, 74, 99-102.

26. Surdu-Bob, C. C.; Saied, S. O.; Sullivan, J. L. *Appl. Surf. Sci.* **2001**, 183, 126-136.

27. Petkov, K.; Krastev, V.; Marinova, T. *Surf. Interf. Anal.* **1992**, 18, 487.

28. Sainio, J.; Aronniem, M.; Pakarinen, O.; Kauraal, K.; Airaksine, S.; Krause. O.; Lahtinen, J. *Appl. Surf. Sci.* **2005**, 252, 1076-1083.

29. Jeong, D. S.; Schroeder, H.; Waser, R. *Appl. Phys. Lett.* 2006, 89, 082909.

30. Jeong, D. S.; Schroeder, H.; Waser, R. *Electrochem. Solid State Lett.* **2007**, 10, G51-G53.

31. Meyer, R.; Schloss, L.; Brewer, J.; Lambertson, R.; Kinney. W.; Sanchez, J.; Rimerson, D. *IEEE Proceed. NVMTS2008*. **2008**, 1.

32. Nian, Y. B.; Strozier, J.; Wu, N. J.; Chen, X.; Ignatiev, A. *Phys. Rev. Lett.* **2007**, 98, 146403.

33. Lee, M. J.; Han, S.; Jeon, S. H.; Park, B. H.; Kang, B. S.; Ahn, S. E.; Kim, K. H.; Lee, C. B.; Kim, C. J.; Yoo, I. K.; Seo, D. H.; Li, X. S.; Park, J. B.; Lee, J. H.; Park, Y. *Nano Lett.*, **2009**, 9, 1476-1481.

34. Jo, S. H.; Kim, K. H.; Lu, W. *Nano Lett.* **2009**, 9, 496-500.

35. Grieshammer, S.; Grope, B. O. H.; Koettgen, J.; Martin, M. *Phys. Chem. Chem. Phys.*

2014, 16, 9974-9978.

36. Kang, S. G.; Sholl, D. S. *RSC. Adv.* **2013**, 3, 3333-3341.

37. Chang, T.; Jo, S. H.; Lu, W. *ACS Nano*. **2011**, 5, 7669-7676.

38. Jo, S. H.; Chang, T.; Ebong, I.; Bhadviya, B. B.; Muzumder, P.; Lu, W. *Nano Lett.* **2010**, 10, 1297-1301.

Chapter 3

Hydrogen separation by nanocrystalline titanium nitride membranes with high hydride ion conductivity

3-1 Introduction

The use of clean energy that does not use fossil fuels is required under the regulatory efforts to release CO_2 gas (global warming gas) that began in the 1990's.[1] The increasing demand for "clean" and efficient energy has resulted in an increased global willingness to embrace the proposed "hydrogen economy" as a potential long term solution to the growing energy crisis. Advent of hydrogen economy, however, cannot be realized until technical issues related to hydrogen production, separation and a storage infrastructure must be clear. Since hydrogen is normally produced by steam reforming of methane gases or water electrolysis by a use of renewable energy sources, contaminations such as CO, CO_2 and O_2 gases are remained.[2,3] Meanwhile, polymer electrolyte fuel cells, which is one of major application for hydrogen fuels, require an ultrapure grade (99.995%) and can only tolerate contaminants of ppm orders within hydrogen streams due to poisoning of Pt catalysts.[4] While physical processes such as pressure swing adsorption (PSA) and fractional/cryogenic distillation systems are in commercial operation, they are generally not cost effective and are quite energetically demanding for the separation and

purification of H_2.[5,6] In addition, neither of these methods provides sufficient purity for the targeted applications. Alternatively, membrane separation, is currently considered to be the most promising because of low energy consumption, possibility for continuous operation, its ease of operation, and ultimately cost effectiveness.

Nowadays, palladium and its silver alloys are extensively used for hydrogen separation membranes due to the outstanding permeability combining high solubility of hydrogen and excellent tolerance to hydrogen embrittlement.[7,8] Because of the natural resource scarcity of Pd metals, however, for sustainability, the development of non-Pd-containing alternatives has spurred considerable interest in both academia and industry. Although Nickel and groups III–V metallic elements have the ability to dissociate and dissolve hydrogen, they suffer serious hydrogen embrttlement,[9,10] because hydrogen dissolution in the metal matrix aids its deformation,[11,12] with the corresponding embrittlement progressing with increasing hydrogen solubility. Hence, materials scientists are challenged with finding new strategies for designing hydrogen separation membranes that do not rely on hydrogen solubility in the metal matrix.[13-17]

Mixed proton-electron conductors (MPECs) are viable alternatives to dense separation membranes,[15-20] featuring ambipolar diffusion of H^+ and e^- and thus achieving hydrogen transport driven by chemical potential gradients.[21] Perovskite-type proton-conducting ceramics of the type $BaM_{1-x}M'_xO_{3-\delta}$ (M = Ce, Zr; M' = Y, Yb, etc.) are one example of MPECs; however, they are normally utilised at elevated temperatures (T > 600°C),[15,17,18] since the abovementioned migration features high activation energies (50–60 kJ mol^{-1}) due to trapping by negatively charged aliovalent dopants[22-24] or defect-induced structure distortion.[25]

Herein, pronounced hydride ion-electron conductivity of nanocrystalline titanium nitride (TiN_x) were reported, attributed to interfacially controlled diffusion aided by hydridic Ti–H terminal groups on the hydrogenated grain surface. Such materials allow much faster hydrogen permeation than that observed for Pd metal at close-to-ambient temperatures.

3-2 Experimental

3-2-1 Hydrogen permeability tests

(a) Preparation of aluminum porous support

For hydrogen permeability testing, TiN_x membranes were fabricated on a porous alumina support prepared using a previously described method.[26,27] In brief, α-Al_2O_3 powder (BAIKALOX 1.0R) was uniaxially pressed at 20 MPa and sintered in air at 1200°C for 12 h to afford macroporous α-Al_2O_3 pellets (diameter = 12 mm, thickness = 1.0 mm) with 40% porosity[26] (Fig 3-1). Thus, the obtained pellets were coated with a mesoporous γ-Al_2O_3 layer using sol-gel spin coating. 8.4 g of Aluminium-tri-*sec*-butoxide was dissolved in hot water (50 mL) at 90°C to obtain a white sol. After vigorous stirring for 20 min and addition of hot water, the reaction mixture was treated with 0.1 M HNO_3 (1 mL) to obtain a 1 M boehmite (γ-AlOOH) clear sol. Polyvinyl alcohol (PVA) solutions were prepared by dispersing PVA (1.05 g; PolyScience, M_w = 78000) in boiling water (50 mL) under vigorous stirring. A viscous boehmite precursor sol (0.6 M) was prepared by pouring the above PVA solution (20 mL) into the 1 M boehmite sol (30 mL)

(Fig. 3-2). A 1.2-μm mesoporous γ-Al_2O_3 layer was deposited by spin casting the precursor sol on sintered α-Al_2O_3 at 3000 rpm for 20 s, drying for 3 h at room temperature, and 3-h annealing at 700°C in air at a rump rate of 1.5°C min^{-1} [27](Fig. 3-3).

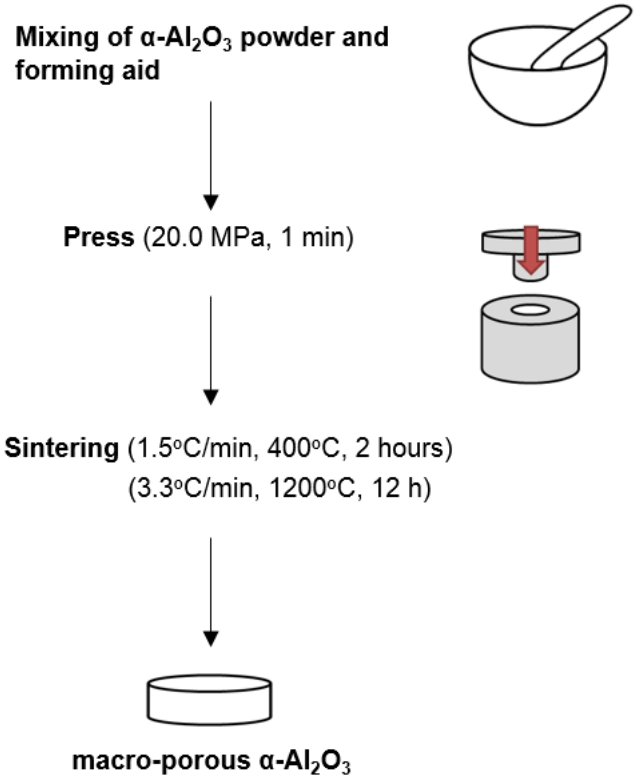


Fig. 3-1 Preparation procedure of macroporous α-Al_2O_3 sintered disk.

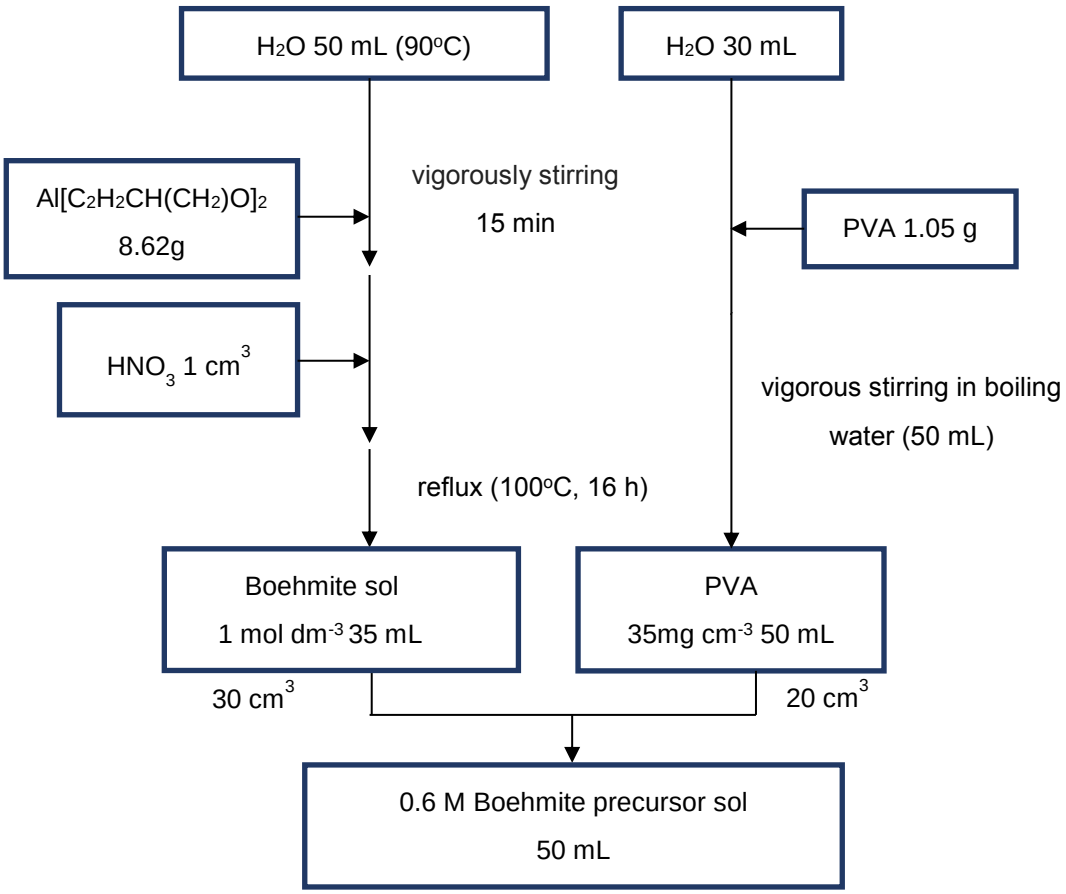


Fig. 3-2 Preparation procedure of Boehmite precursor sol

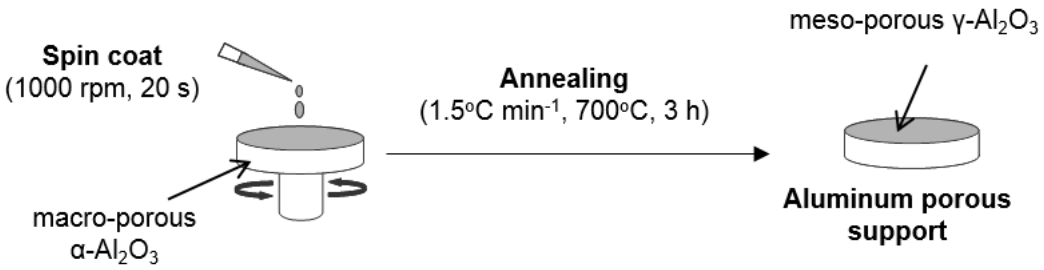


Fig. 3-3 Spin-coating of mesoporous γ-Al_2O_3 layer on α-Al_2O_3 disk.

(b) RF sputtering deposition of TiN_x membranes

TiN_x membranes (x = 0.7 - 1.0) were deposited by reactive sputtering on a two-inch-diameter Ti (99.99% purity) disk at a base pressure of less than 2×10^{-5} Pa, performed in an ultrahigh vacuum chamber system (ULVAC S-3000). Typically, TiN_x films were deposited in an Ar/N_2 atmosphere at a total pressure of 0.9 Pa, substrate temperature of 500 and 200°C, and a sputtering power of 195 W. The Ar/N_2 gas flow ratio was controlled by a mass flow controller, with the total gas flow rate ($Ar + N_2$) fixed at 20 sccm (Fig. 3-4).

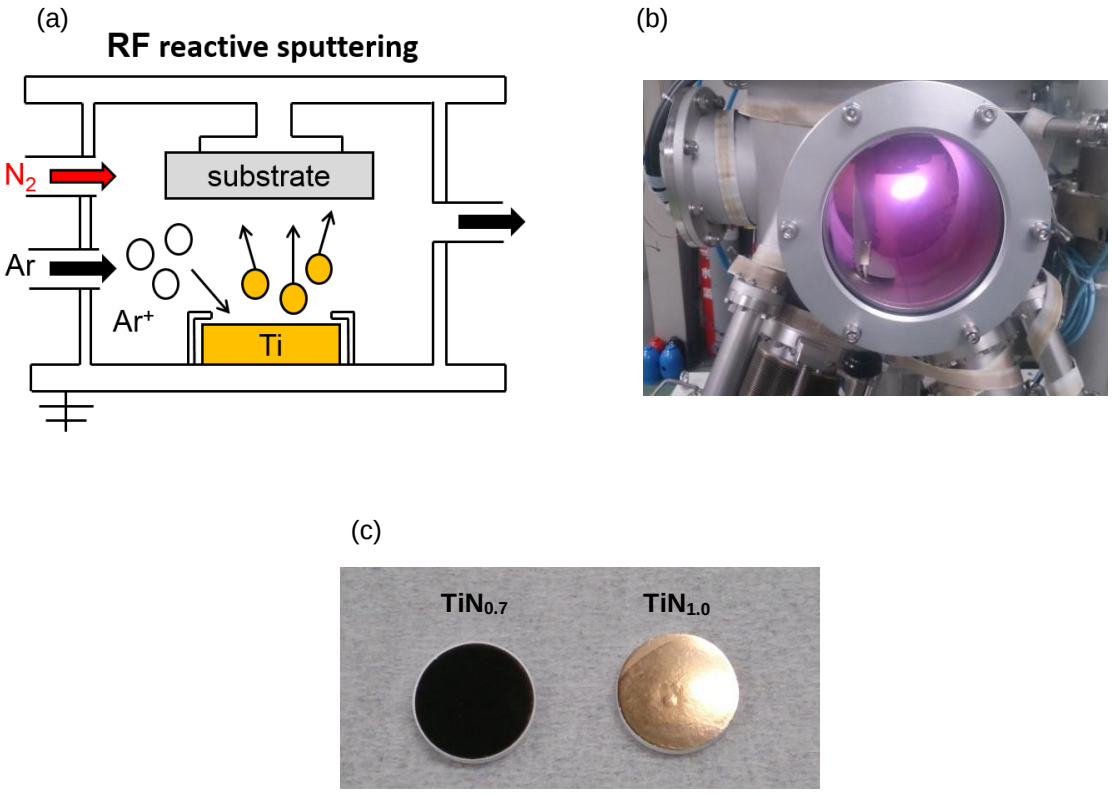


Fig. 3-4 (a) Schematic view of TiN_x film deposition by RF reactive sputtering. (b) Picture of RF sputtering apparatus (MB06-1049-0). (c) Optical images of $TiN_{0.7}$ and $TiN_{1.0}$ deposited on Al_2O_3 support.

(c) Hydrogen permeation tests of TiN_x membranes

Hydrogen permeabilities of TiN_x membranes were determined using an in-house-made gas-tight chamber equipped with a gas chromatograph (Variant Micro GC-4000). H_2 and N_2 gases were detected by a thermal conductivity detector using Ar and He as reference gases, respectively. A TiN_x membrane sample was immobilised in a specially designed sample holder using carbon sheet gaskets and placed in an electrical furnace with controlled temperature. Pure Ar gas was supplied to the porous support side at 25 sccm, and H_2/N_2 mixtures (typically 1:1) were supplied to the membrane side at 100 sccm, with all flows regulated by mass flow controllers (Fig. 3-5 and Table 3-1).

The H_2 and N_2 concentrations in the out gas were analyzed by a micro gas chromatography (micro-GC Varian 400) for hydrogen permeation tests of the TiN_x membranes. The micro GC was equipped with two thermal conductivity detector (TCD) where one is used for the analysis of H_2 and He gas with a flow of an Ar reference gas and the other is used for N_2 with a flow of a N_2 reference gas. The micro GC was calibrated by using 10, 1 and 0.01% standard gases of H_2, N_2 and He gases balanced by Ar or He base gases. Hence concentrations of H_2 and N_2 gases can be determined by extrapolated to the calibration curve. The permeation tests were carried out by a homemade gas permeation system (Fig. 3-5). Normally, a 1:1 mixed gas of H_2/N_2 or He/N_2 was supplied to the surface side of a TiN_x membrane at 100 sccm and a pure Ar was supplied to the porous support side at 25 sccm. The permeation gases across the membranes were carried with the Ar flow into micro GC and the concentrations were determined.

The hydrogen fluxes J_{H2} are determined from the H_2 concentrations in the permeation

gas as follows,

$$J_{H2} = \frac{C_H J_{Ar}}{C_{Ar}} \tag{3-1}$$

where C_H and C_{Ar} are the concentration of H_2 and Ar in the out gases and J_{Ar} is the Ar flow (25 sccm) supplied to the alumina support side (Fig. 3-5(b)). The fluxes of N_2 and He were also determined by the same way.

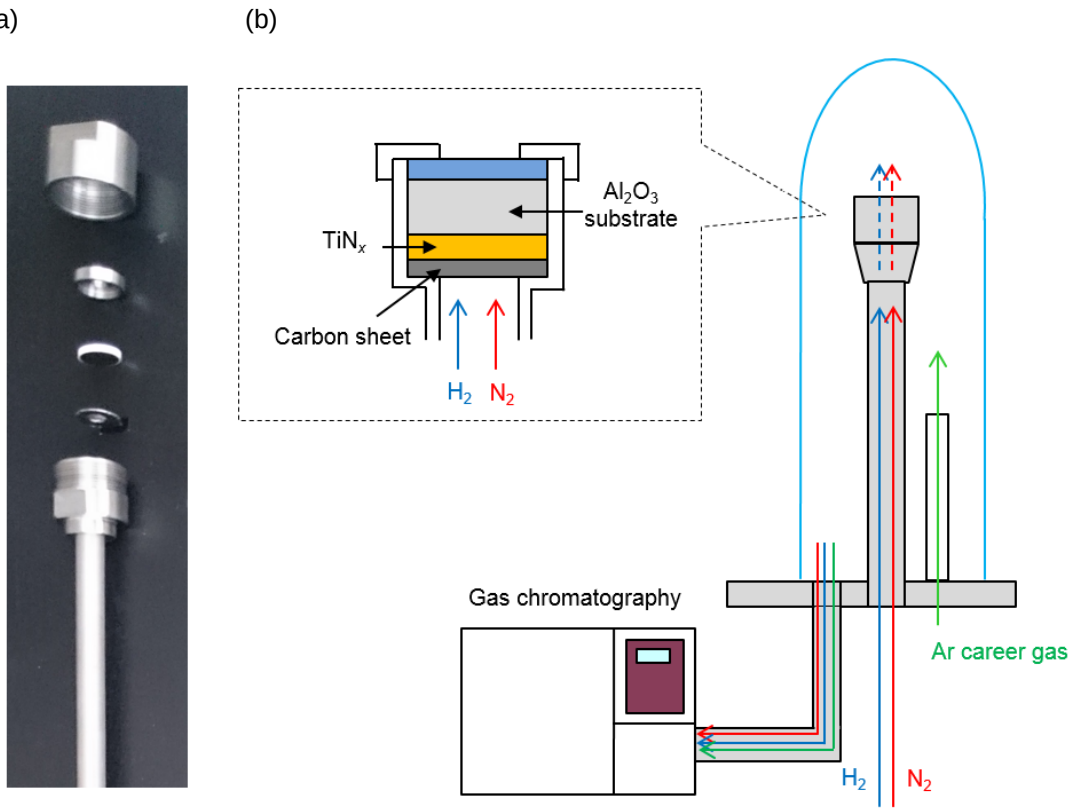


Fig. 3-5 Apparatus for hydrogen permeation measurements. (a) The sample holder to seal the TiN_x membrane devices. (b) Schematic illustration of a home-made chamber system equipped with GC.

Table 3-1 The concentrations of H_2, N_2 and Ar gases in the out gases of TiN_x (x = 0.7-1.0) membranes at 25°C, measured by GC during the permeation tests with supplying an 50%-H_2/N_2 gas at an entrance side.

Samples	Concentrations / %		
	H_2	N_2	Ar
$TiN_{0.7}$	1.80	0.0906	98.1
$TiN_{0.9}$	1.14	0.0945	98.8
$TiN_{1.0}$	0.373	0.0945	99.5

(d) Method to determine the p_{H2} at TiN_x/support interface

When hydrogen permeates through TiN_x/Al_2O_3 support structure, the resulting pressure profiles depend on the properties of each layer. At steady state, the hydrogen flux of TiN_x membrane, J_1 is equivalent to one of Al_2O_3 support, J_2 (Fig. 3-6). Here, the hydrogen partial pressure at entrance and exit sides are defined as p_{H2}' and p_{H2}''', respectively, as shown in Fig. 3-6(a). p_{H2}' and p_{H2}''' are known, so that the pressures p_{H2}'' at interface between TiN_x and porous alumina can be determined with the flux calibration curve of porous supports by the following way.

The flux J_2 through the Al_2O_3 support is given by Eq. (3-2) [27],

$$J_2 = \frac{F_H}{A} \tag{3-2}$$

where F_H is the hydrogen flow and A is the surface area. The hydrogen permeance of Al_2O_3 support, φ_2, has been given by Eq. (3-3),[28]

$$\varphi_2 = \frac{J_2}{(p_{H2}'' - p_{H2}''')} = \alpha + \beta \times \frac{(p_{H2}'' + p_{H2}''')}{2} \tag{3-3}$$

where (p_{H2}”+ p_{H2}”’)/2 gives an ‘average’ pressure of Al_2O_3 support. Accordingly, the plots of φ_2 vs. (p_{H2}”+ p_{H2}”’)/2 must show a linear relationship.

Fig. 3-6(b) is the calibration curve of our Al_2O_3 support, indicating clear linear relationship between φ_2 and (p_{H2}”+ p_{H2}”’)/2. Accordingly, p_{H2}” can be determined by reading the average pressure corresponding to the flux J_2 from the calibration curve. Hence, p_{H2}” is determined by

$$p_{H2}'' = \frac{-\alpha + \sqrt{\alpha^2 + 2\alpha\beta p_{H2}''' + \beta^2 p_{H2}''^2 + 2\beta J_2}}{\beta} \tag{3-4}$$

The hydrogen permeances, P_H, were determined from J_{H2} by the following.

$$P_H = J_{H2} (p_{H2}'\text{-}p_{H2}''') \tag{3-5}$$

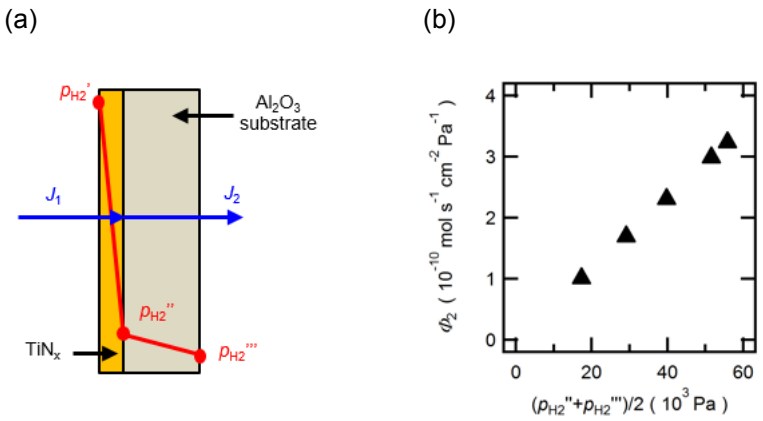


Fig. 3-6 (a) Schematic representation of hydrogen chemical potential gradients across TiN_x/porous-Al_2O_3-support membrane devices. (b) φ_2 vs (p_{H2}”+p_{H2}”’)/2 calibration curve of porous alumina support.

3-2-2 Characterization techniques

(a) Material characterization

Phase purities were determined by X-ray diffraction (XRD; RIGAKU RINT2200) under these conditions; Cu Kα radiation, in the 2θ range of 20 to 80 degree with a monochromator under the conditions; Cu Kα radiation, 40 kV, 20 mA. For XRD measurements, a Si wafer spin-coated with mesoporous γ-Al_2O_3-layer (100 nm thickness) was used as an alternative substrate to γ-Al_2O_3/α-Al_2O_3 bilayer porous supports used for permeation tests, because most of XRD patterns of TiN_x were overlapped with those of α-Al_2O_3 and influence of crystallographic orientation of Si wafer should be precluded. The spin-coating of γ-Al_2O_3 were conducted by the similar methods as mentioned above with a 0.1 M boehmite sol.

Chemical compositions were examined by wavelength-dispersive X-ray analysis (WDX; JEOL JXA-8530F). The above measurements were performed for 0.5–1.0-μm-thick TiN_x films deposited on a Si wafer.

Rutherford backscattering spectrometry (RBS) was carried out utilising 600-nm-thick films deposited on glassy carbon using a 2.0-MeV He^+ beam (Tohoku University). To preclude the increase of background signal by using heavy elements for substrates, the films for RBS measurements were deposited on glassy carbon plates. The obtained spectra were fitted using the RUMP software package.[29]

The morphologies of TiN_x membranes prepared on porous alumina supports were characterised by transmission electron microscopy (TEM; JEOL JFM-ARM-200F), with the corresponding specimens prepared by focused ion beam microfabrication (FIB; HITACHI FB-2100).

Field emission scanning electron microscopy (FE-SEM) imaging was carried out using a JEOL JSM-6500F instrument.

Fourier transform infrared (FT-IR) spectroscopy was conducted for 600-nm-thick TiN_x films on porous alumina supports utilising a JASCO FT/IR-350 spectrometer. In situ measurements were performed in a gas-sealed optical cell with an antireflective glass window under controlled atmospheric and thermal conditions.

H, D and O impurity profiles were measured by time-of-flight secondary ion mass spectroscopy (ToF-SIMS; Ulvac-PHI ADEPT1010), equipped with a Cs^+ ion gun for first ion beam. The measurements were conducted in dynamic mode with irradiating 5 keV Cs^+ ion at a beam current of 100 nA on analysis area of 100 μm × 100 μm by a cycle of 20 μs. For the calibration of D and O species, deuterium and oxygen ion-implanted TiN_x films (1 μm thickness) fabricated on a Si wafer was used as a standard sample, which was prepared by MST Foundation, Japan. Calibration of H species was prepared from D signal intensity by using isotope sensitivity factor.

Magic-angle-spinning nuclear magnetic resonance (MAS-NMR) spectroscopy was performed using a JEOL JNM-ECAII spectrometer. The measurements were operated at a resonance frequency of 598.97 MHz equipped with a magic angle spinning probe with a diameter of 3.2 mm. The MAS frequency was 10 kHz. For each sample, spectra were acquired with two kind of pulse sequence, single pulse with 30 deg pulse with a length of 1.5 μs, and DEPTH background suppression pulse sequence with 90 deg pulse. The measured frequency range was 10 kHz. Repetition times were 5 s for single pulse experiments, and 8 s for DEPTH experiments. The numbers of scans were 318 for single pulse experiments and 256 for DEPTH experiments. Chemical shifts were externally

referenced to tetramethylsilane (TMS). For NMR measurements, 2.5 μm-thick TiN_x films were deposited on a Si wafer modified with a 100-nm-thick γ-Al_2O_3 buffer layer and then were detached from the wafer by scratching with sacrificing the γ-Al_2O_3 layer. The powder specimens thus obtained were filled into a sample tube under H_2 atmosphere.

Amount of the hydrogen absorbed are measured with a home-made gas flow chamber system equipped with a 5 MHz quartz crystal microbalance (QCM) device (USI System) at 25°C. AT-cur quartz crystal resonator (1.0 cm∅) have an Au film electrode (1.32 cm^2). The TiN_x films are deposited directly on the Au film electrode through a shadow mask at 200°C by the similar methods as mentioned above. The amount absorbed are determined by the shift of the resonance frequency as switched from pure Ar to 50%-H_2/Ar gases at 25°C.

(b) Density-functional theory (DFT) calculations

The electronic states and energies of hydrogen adatoms on TiN (100) surfaces were characterized by first-principle calculation. The calculations were based on the spin-polarized density-functional theory (DFT) with Heyd-Scuseria-Ernzerhof (HSE06) hybrid functions[30] or the generalized gradient approximation (GGA) using Perdew-Wang 91 (PW91) exchange-correlation functions,[31] which are implemented in the plane-wave and projector augmented wave method, the Vienna Ab-initio Simulation Package (VASP).[32-37] The supercells were consists of 2×2×2 TiN unit cells (~ 64 atoms) with neutrally charged defects. Cutoff energy for the plane-wave basis was set to 600 eV. A Γ-centered 3×3×3 Monkhorst-Pack special k-point grid[38] for the first Brillouin zone using Gaussian smearing model of σ=0.05 eV was used. Atomic positions were optimized until

the forces on each atom were smaller than 0.02 eV/Å.

The defect-formation energies (ΔE_{def}) for N or H defects in rock salt type TiN phases were calculated by DFT with Heyd-Scuseria-Ernzerhof (HSE06) hybrid functions.[30] The ΔE_{def} can be defined as the change in total energy according to the incorporation of a defect into a supercell.[39,40] ΔE_{def} for H defects in $TiN_{1-\delta}$ supercells can be expressed by

$$\Delta E_{def} = E^{tot}[\mathrm{TiN}_{1-\delta}\mathrm{H}] - E^{tot}[\mathrm{TiN}_{1-\delta}] - 1/2\mu_{H2} \qquad (3\text{-}6)$$

where E^{tot}[supercell] represents the total energy of each supercell. The chemical potential of H denoted by μ_H is derived from hydrogen enthalpy.[40] ΔE_{def} is calculated for stoichiometric TiN phase with one H interstitials, H_i: $TiN(H_i)_{1/32}$ ($Ti_{32}N_{32}H$) and N-deficient $TiN_{0.75}$ with one H on N vacancy, H_N: $TiN_{0.75}(H_N)_{1/32}$ ($Ti_{32}N_{24}H$). The calculated equilibrium lattice parameters of TiN, $TiN(H_i)_{1/32}$, $TiN_{0.75}$ and $TiN_{0.75}(H_N)_{1/32}$ are 4.215, 4.222, 4.197 and 4.199 Å, respectively.

For $TiN(H_i)_{1/32}$, three type of H interstices are considered; i) $^{tet}H_i$: tetrahedral site of fcc Ti sublattice, ii) $^{Ti-N}H_i$: center of the closest Ti–N bond and iii) $^{Ti-Ti}H_i$: center of the closest Ti–Ti bond (Fig.3-24). ΔE_{def} for all interstitial defect models, however, fall into large positive values (> 2 eV) even after lattice relaxation, and so the formation of the H interstitials is not favorable for TiN_x. On the other hand, ΔE_{def} for hydrogen defects on N vacancy sites, H_N, is converged to negative value (–0.75 eV) (Fig.3-24). Fig.3-24(b) and (c) show partial density of states (p-DOS) for $TiN_{0.75}$ and $TiN_{0.75}(H_N)_{1/32}$.

The adsorption energies (ΔE_{ad}) were calculated by DFT using Perdew-Wang 91 (PW91) exchange-correlation functions.[31] The calculations were performed for the adsorption of hydrogen monoatoms, H_{ad}, onto (100) surface of rock salt TiN. The ΔE_{ad} is defined by

$$\Delta E_{ad} = E^{tot}[\mathrm{TiN}(H_{ad})] - E^{tot}[\mathrm{TiN}] - 1/2\mu_{H2} \qquad (3\text{-}7)$$

A slab containing five (100) layers with frozen two bottom layers was considered as a surface model to study adsorption of hydrogen on (100) surface. The 1 × 1 unit cell surface was chosen in a way that H_{ad} in next cell are separated by 4.22 Å. These slabs include 10 Ti atoms and 10 N atoms. A vacuum size of 20 Å is used to keep the slabs from interacting each other.

3-3 Results and Discussion

3-3-1 Fabrication of TiN_x membranes

First, with the aim of fabricating TiN_x films with tailored nitrogen content (x), a broad survey of deposition conditions for reactive sputtering of a pure Ti target were performed by changing the Ar and N_2 mixing ratio in the process gas (at 0.9 Pa pressure). The substrate temperature was typically set at 500°C. Single-phase NaCl-type TiN_x films were obtained with $0.7 < x < 1.0$, as confirmed by X-ray diffraction (XRD; Fig. 3-7), wavelength-dispersive X-ray spectroscopy (WDX; Fig. 3-8) and Rutherford back scattering (RBS; Fig. 3-9) analyses. All films contain small amounts of oxygen impurities (O/Ti < 0.04) (Table 3-2). Consequently, stoichiometric ($TiN_{1.02}O_{0.02}$), slightly N-deficient ($TiN_{0.95}O_{0.04}$) and highly N-deficient ($TiN_{0.74}O_{0.04}$) films were prepared with 100%, 10% and 2.5%-N_2/Ar process gases, respectively. These films were subjected to further investigations, and for brevity are denoted by $TiN_{1.0}$, $TiN_{0.9}$ and $TiN_{0.7}$.

Hydrogen-permeable membranes were fabricated by depositing dense 600 nm-thick

TiN_x layers on porous alumina supports modified by a 1-μm-thick mesoporous γ-Al_2O_3 top layer.[26,27] As a result, columnar TiN_x layers are uniformly formed over a wide γ-Al_2O_3 area (Fig. 3-10(a-b)) with no significant oxidation observed at the TiN_x/Al_2O_3 interface (Fig. 3-10(c)). Each column comprises rectangular nanograins with an average size (d_{av}) of a few tens of nanometers (Fig. 3-10(d-e) and Fig. 3-11), with similar microstructural features reported elsewhere for sputter-deposited TiN_x films.[41]

3-3-2 Hydrogen permeability

To determine hydrogen permeability and selectivity, 50 vol%-H_2/N_2 mixtures were supplied to the surface side of the membranes, and the exit gases from the support side were analysed (for details, see 3-2-1(c)). It is noted that the diffusion of hydrogen and nitrogen through the pores of the bare alumina supports resulted in temperature-independent permeation fluxes (J_{H2} and J_{N2}, respectively) of 1-3 × 10^{-6} mol cm^{-2} s^{-1} (Fig. 3-12).

Surprisingly, TiN_x membranes exhibit a pronounced hydrogen permeability in a wide temperature range above 25°C. For all x, J_{H2} increases considerably with temperature, reaching values above 7 × 10^{-7} mol cm^{-2} s^{-1} at 500°C, whereas J_{N2} is temperature independent and ca. 2 × 10^{-8} mol cm^{-2} s^{-1}. Hence, J_{H2} is at least 30 times higher than J_{N2} at 500°C. The non-zero value of J_{N2} observed for TiN_x is evidently due to a small leak in the seal, the value being identical to the J_{N2} measured for a thick stainless plate as a dummy specimen (Fig. 3-12(a)). The flux of helium through $TiN_{0.7}$ roughly equals that of nitrogen, despite of the fact that He molecules are smaller than those of H_2 (see J_{He} in Fig. 3-12(a)), strongly suggesting that hydrogen transport in TiN_x membranes does not

rely on pore diffusion through the pinholes or cracks.

In N-deficient films (x = 0.7 and 0.9), J_{H2} shows an Arrhenius-type linear temperature dependence at $T \geq 250$°C, which becomes, however, much less pronounced at $T \leq 200$°C (Fig. 3-12(a)). The corresponding activation energies (E_a) of hydrogen permeation through $TiN_{0.7}$ and $TiN_{0.9}$ at $T \geq 250$°C are determined as 5.8 and 6.3 kJ mol^{-1}, respectively (Table 3-3). Although the hydrogen permeation flux of $TiN_{1.0}$ is several times smaller than those of N-deficient samples (x = 0.7 and 0.9) at T < 100°C, the gap between these values decreases at T > 300°C because of the relatively large E_a (12 kJ mol^{-1}) of $TiN_{1.0}$. In fact, these E_a values of TiN_x systems are much smaller than that of hydrogen diffusion in Pd metal (26 kJ mol^{-1}).[8] Thus, J_{H2} value of 600 nm-thick $TiN_{0.7}$ is at least two orders of magnitude higher than that of a Pd membrane with a technologically limited thickness of 5 μm at 25°C (Fig. 3-12(b)). Morphological changes are not evident in the membranes after the hydrogen permeation tests in the temperature range of 25-500°C (Fig. 3-13).

The hydrogen permeability of TiN_x membranes increases monotonically with decreasing membrane thickness (L), indicating that the overall permeability is controlled by hydrogen diffusivity rather than by surface kinetics (Fig. 3-12(b)). Importantly, the 200-nm-thick $TiN_{0.7}$ membrane achieves a J_{H2} value of 1×10^{-6} mol cm^{-2} s^{-1} at 25°C, being as high as that observed for mesopore diffusion through the alumina support.

For mass transfer based on thermally-activated jumps of hydrogen atoms or ions, the ratio between hydrogen and deuterium fluxes, J_{H2}/J_{D2}, should be close to $\sqrt{M_D}/\sqrt{M_H} \sim 1.4$ due to the $M^{-0.5}$-dependency of the jump rate.[42] Fig. 3-15 shows the relaxation of the permeation flux observed upon switching the supplied gases between H_2 and D_2 at a fixed temperature. The above fluxes abruptly decrease upon switching from H_2 to D_2, followed

by equilibration to an overall decrease of 24%, and subsequently quickly recovering to the original level upon switching back to H_2. Thus, the observed J_{H2}/J_{D2} ratios exceed 1.3 at temperatures above 25°C, with similar behaviour observed for $TiN_{1.0}$ films. Therefore, hydrogen diffusion in TiN_x is attributed to thermally-assisted mass jumps.

The hydrogen permeability of TiN_x membranes is significantly improved by reducing the grain size (Fig. 3-14). TiN_x membranes (x = 0.7 and 1.0) comprising smaller grains could be successfully fabricated by lowering the deposition temperature from 500 to 200°C and adjusting process gas composition. d_{av} of $TiN_{0.7}$ films deposited at 500 and 200°C were found to be 23 and 14 nm, respectively, as confirmed by XRD analysis of (111) peaks (with the Scherrer equation (Fig. 3-7)) and by TEM imaging (Fig. 3-10(d-e) and Fig. 3-11). Decreasing d_{av} from 23 to 14 nm increased J_{H2} by a factor of 1.4 at all temperatures (Fig. 3-14), with this factor being roughly equivalent to the inversed ratio of the d_{av} which is $(14\text{ nm}/23\text{ nm})^{-1}$~1.6. Similarly, the ratio of J_{H2} values obtained for $TiN_{1.0}$ deposited at 200°C (d_{av} = 12 nm, calculated based on the (200) peak) and 500°C (d_{av} = 22 nm) is approximately equal to 1.7-2.5, which is in agreement with the inversed d_{av} ratio, $(12\text{ nm}/22\text{ nm})^{-1}$~1.8. According to the brick layer model,[43,44] the grain-boundary volumes of nanocrystalline materials are proportional to their volumetric surface areas, which are correlated with d_{av}^{-1}. The linear scalability of J_{H2} vs d_{av}^{-1} thus provides clear evidence of interfacially controlled diffusion.

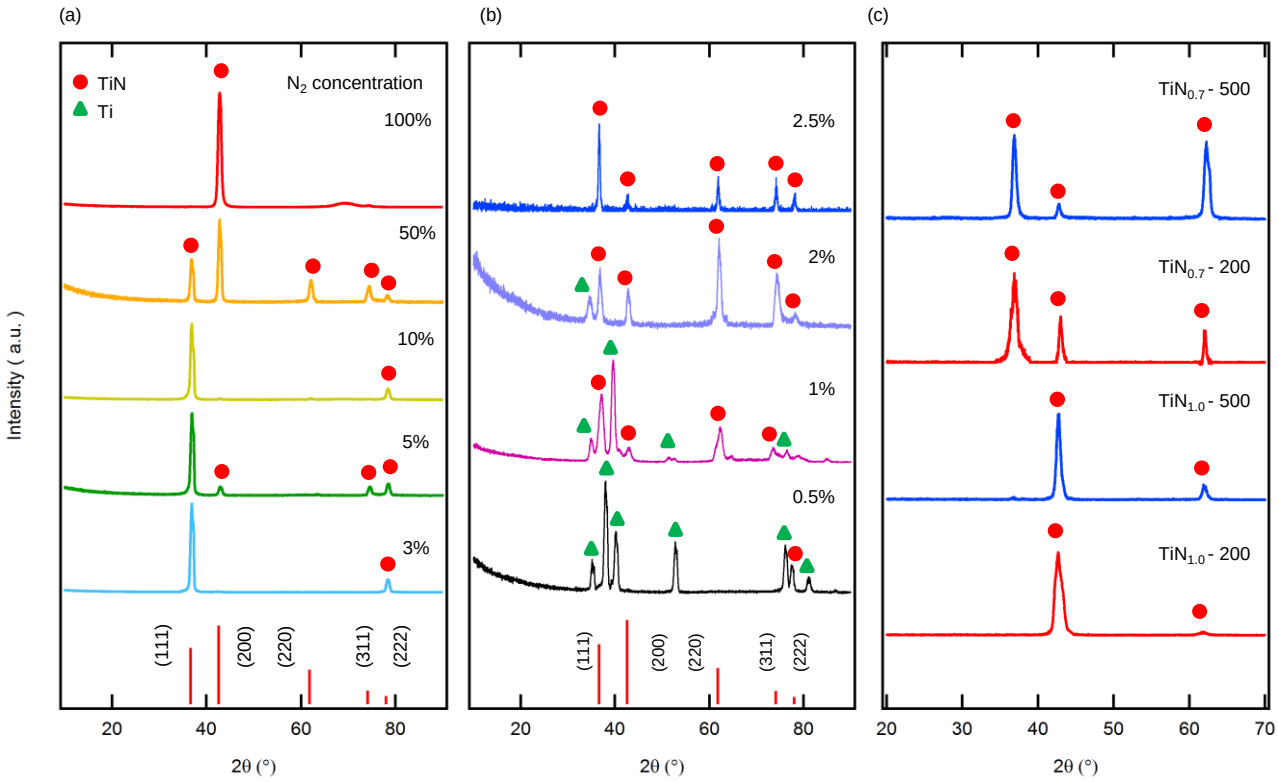


Fig. 3-7 XRD patterns of TiN_x films. (a), (b) TiN_x films deposited on a Si wafer (100) by RF sputtering in reactive gases with various N_2 concentrations. Chamber pressure and substrate temperature were fixed at 0.9 Pa and 500°C, respectively. (c) 600 nm-thick TiN_x (x = 0.7 and 1.0) films deposited on a Si wafer modified by γ-Al_2O_3 mesoporous layer (100 nm thickness). Sputtering was performed at 200 and 500°C.

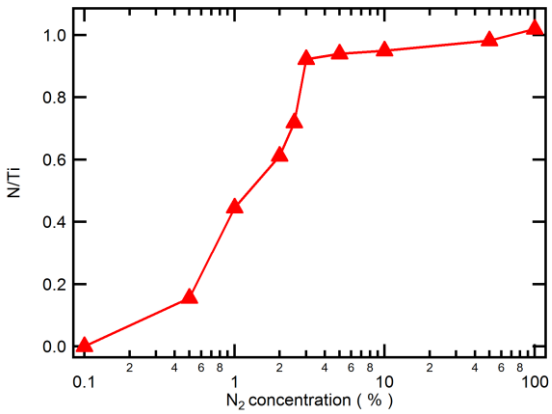


Fig. 3-8 Nitrogen stoichiometry of sputter-deposited TiN_x thin films as a function of N_2 concentrations in reactive sputtering gases. *x* is determined by WDX.

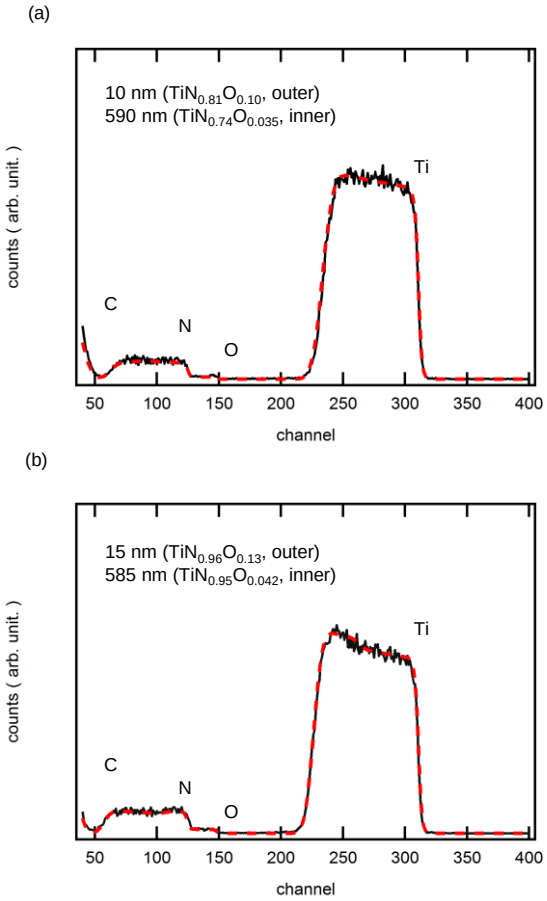


Fig. 3-9 RBS depth profiles of $TiN_{0.7}$ and $TiN_{0.9}$ films prepared on glassy carbon substrates. The film thickness is 600 nm. Black lines are the observed and red dots the simulated. The film deposited in (a) 2.5%- and (b) 10%-N_2 gases have homogeneous matrices, and the corresponding chemical composition is (a) $TiN_{0.74}O_{0.035}$ ($TiN_{0.7}$) and (b) $TiN_{0.95}O_{0.042}$ ($TiN_{0.9}$), respectively. The N/Ti ratios are in agreement with the WDX analysis (see Table 3-1 and Fig. 3-8). The surfaces of both films are oxidized by air, forming 10 nm-thick outerlayer with composition of $TiN_{0.81}O_{0.10}$ for 2.5%-N_2 and $TiN_{0.96}O_{0.13}$ for 10%-N_2, respectively.

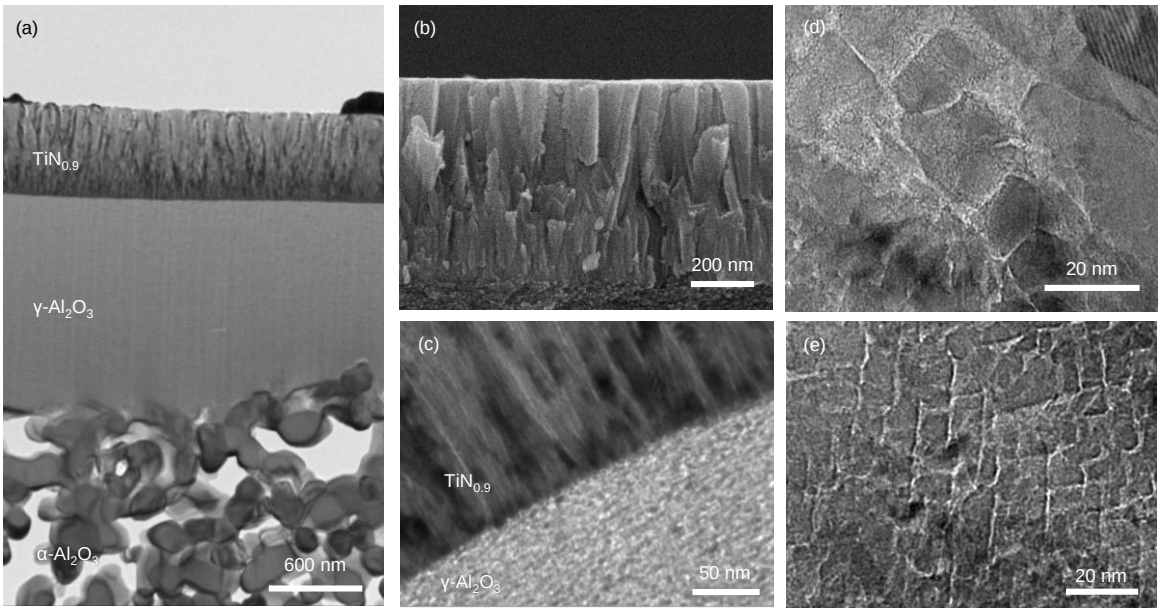


Fig. 3-10 Electron microscopy images showing nanocrystalline, dense TiN_x membranes formed over the porous alumina support. (a) Cross-sectional TEM image of a composite membrane comprising sputter-deposited $TiN_{0.9}$ (top layer, 600 nm), sol-gel-derived mesoporous γ-Al_2O_3 (middle layer, 1 µm), and macroporous α-Al_2O_3 (support). (b) Cross-sectional SEM image illustrating the columnar morphology of $TiN_{0.9}$ membranes. (c) Cross-sectional TEM image of an area close to the $TiN_{0.9}$/γ-Al_2O_3 interface. (d), (e) High-resolution TEM image revealing the nanogranular morphology of $TiN_{0.7}$ membranes deposited at (d) 500°C and (e) 200°C.

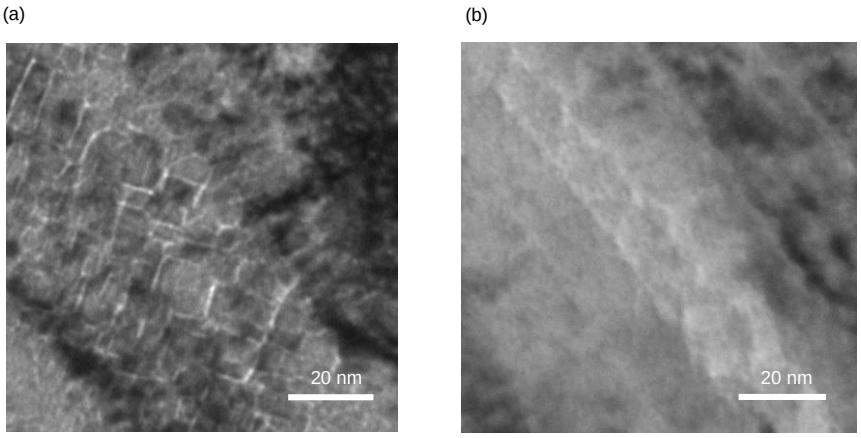


Fig. 3-11 Cross-section TEM images showing nanogranular morphology. (a)$TiN_{0.9}$ and (b) $TiN_{1.0}$.

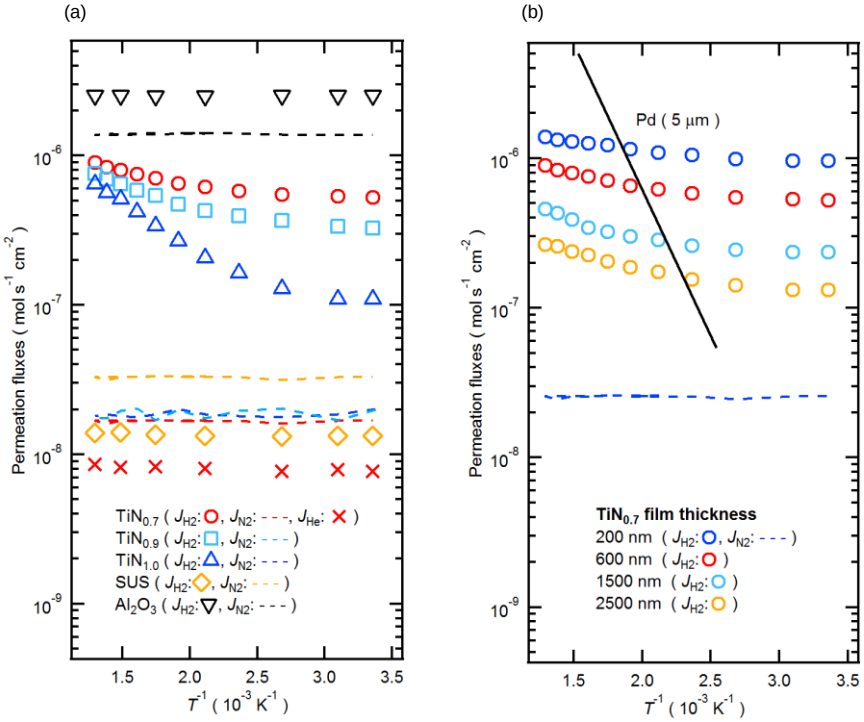


Fig. 3-12 Hydrogen permeability of TiN_x membranes at temperatures between ambient and 500°C. (a) Arrhenius plots of hydrogen (J_{H2}, open symbols) and nitrogen (J_{N2}, dashed lines) fluxes through 600-nm-thick $TiN_{0.7}$, $TiN_{0.9}$, and $TiN_{1.0}$ membranes for 50 vol% H_2/N_2 mixtures supplied at 100 sccm. J_{H2} and J_{N2} of the bare porous alumina support were also measured under identical conditions, along with the helium flux (J_{He}) through $TiN_{0.7}$ for a 50 vol% H_2/He mixture. To calibrate the contribution of background gas leakage from the sample holder, J_{H2} and J_{N2} were measured for a 0.3-mm-thick stainless plate. (b) J_{H2} of $TiN_{0.7}$ membranes of various thicknesses, with J_{N2} of a 200-nm membrane indicated by blue dashed line. The flux of hydrogen through 5-μm-thick Pd foil at ΔP = 50 kPa was calculated using tabulated permeability values.[8]

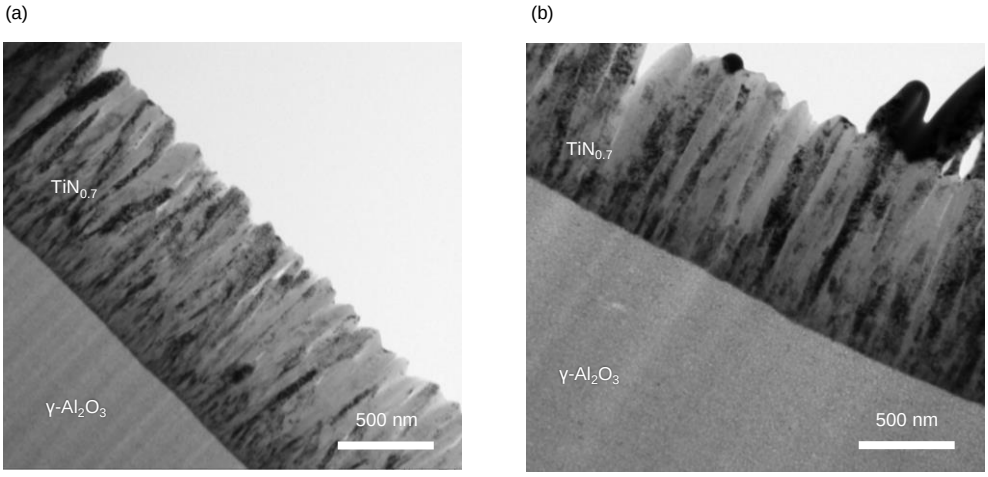


Fig. 3-13 Cross-sectional TEM images of $TiN_{0.7}$ samples (a) before and (b) after hydrogen permeation test.

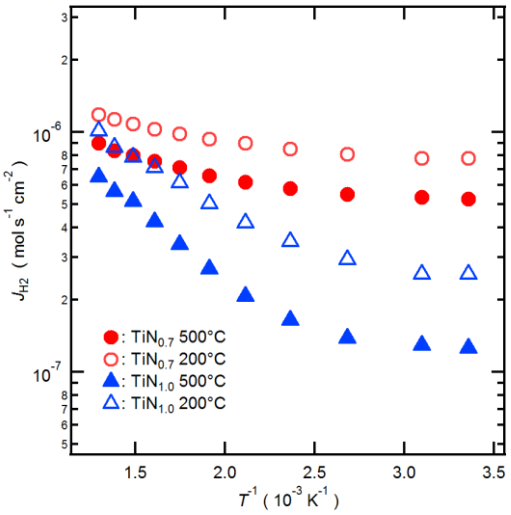


Fig. 3-14 Enhanced hydrogen permeability of nanocrystalline TiN_x membranes with reducing grain sizes. Arrhenius plots of hydrogen flux (J_{H2}) of 600 nm-thick $TiN_{0.7}$ and $TiN_{1.0}$ films prepared at 500 and 200°C. Average grain size (d_{av}) of the films prepared at 500 and 200°C is 23 and 14 nm, respectively, for $TiN_{0.7}$ and is 22 and 12 nm, respectively, for $TiN_{1.0}$.

3-3-3 Hydrogen solubility in TiN_x

To verify the presence of hydrogen in the TiN_x membranes, secondary ion mass spectrometry (SIMS) depth profiling was carried out for $TiN_{0.7}$ films hydrogenated in H_2 or D_2 at 500°C (Fig. 3-16). The analysis revealed flat distributions of H, D and O impurities. Moreover, exposure of pristine films to hydrogen increases their H content from 2×10^{21} to 4×10^{21} atoms cm^{-3}. Heating in D_2 gases resulted in a homogeneous D distribution (~0.9×10^{21} atoms cm^{-3}) and an H concentration of 1×10^{21} atoms cm^{-3}, which confirmed that TiN_x was hydrogenated upon heating in an atmosphere of hydrogen. Similarly, hydrogenation of $TiN_{1.0}$ also occurs by exposure to H_2 or D_2 atmosphere (Fig. 3-17).

Further confirmation of hydrogen solubility in the TiN_x films was obtained by monitoring at room temperature with a 5-MHz quartz crystal microbalance (QCM) hydrogen sorption of TiN_x films deposited at 200°C (Fig. 3-18).[45,46] Upon exposure of $TiN_{0.7}$ and $TiN_{1.0}$ films to H_2, their QCM frequencies dropped abruptly, stabilising at –30.1 and –19.7 Hz, respectively, which corresponds to the incorporation of 1.41 and 0.93 μg of hydrogen, respectively, at p_{H2} = 50 kPa and 25°C. With geometric film volumes and with an ideal molar density (8.44×10^{-2} mol cm^{-3}),[47] the hydrogen sorption capacity, {H/Ti}, for $TiN_{0.7}$ and $TiN_{1.0}$ is calculated to be 0.15 and 0.11, respectively. Stoichiometric $TiN_{1.0}$ can absorb as much hydrogen as $TiN_{0.7}$ despite not being N-deficient, indicating that most of the hydrogen moieties occupy sites other than nitrogen vacancies.

Table 3-2. Phase purity and chemical composition of TiN_x films on a Si wafer.

N_2 concentration / %	Phase	Composition by WDX	Composition by RBS
0.5	TiN, Ti	$TiN_{0.15}O_{0.017}$	
1	TiN, Ti	$TiN_{0.45}O_{0.017}$	
2	TiN, Ti	$TiN_{0.63}O_{0.023}$	
2.5	TiN	$TiN_{0.71}O_{0.015}$ ($TiN_{0.7}$)	$TiN_{0.81}O_{0.10}$ (10 nm, outer)/ $TiN_{0.74}O_{0.035}$ (590 nm, inner)
3	TiN	$TiN_{0.92}O_{0.012}$	
5	TiN	$TiN_{0.94}O_{0.014}$	
10	TiN	$TiN_{0.95}O_{0.020}$ ($TiN_{0.9}$)	$TiN_{0.96}O_{0.13}$ (15 nm, outer)/ $TiN_{0.95}O_{0.042}$ (585 nm, inner)
50	TiN	$TiN_{0.98}O_{0.014}$	
100	TiN	$TiN_{1.02}O_{0.019}$ ($TiN_{1.0}$)	

Table 3-3. Hydrogen fluxes and corresponding activation energies of hydrogen permeability of TiN_x (x = 0.7, 0.9, 1.0) membranes. J_{H2} are the values for 600 nm-thick membranes.

Samples	J_{H2} at 500°C / mol cm^{-2} s^{-1}	J_{H2} at rt / mol cm^{-2} s^{-1}	E_a of permeability / kJ mol^{-1}
$TiN_{0.7}$	9.0×10^{-7}	5.3×10^{-7}	3.1 ($T \leq 200$°C)
			5.8 ($T \geq 250$°C)
$TiN_{0.9}$	7.6×10^{-7}	3.3×10^{-7}	4.5 ($T \leq 200$°C)
			6.3 ($T \geq 250$°C)
$TiN_{1.0}$	6.5×10^{-7}	1.3×10^{-7}	6 ($T \leq 100$°C)
			12 ($T \geq 150$°C)

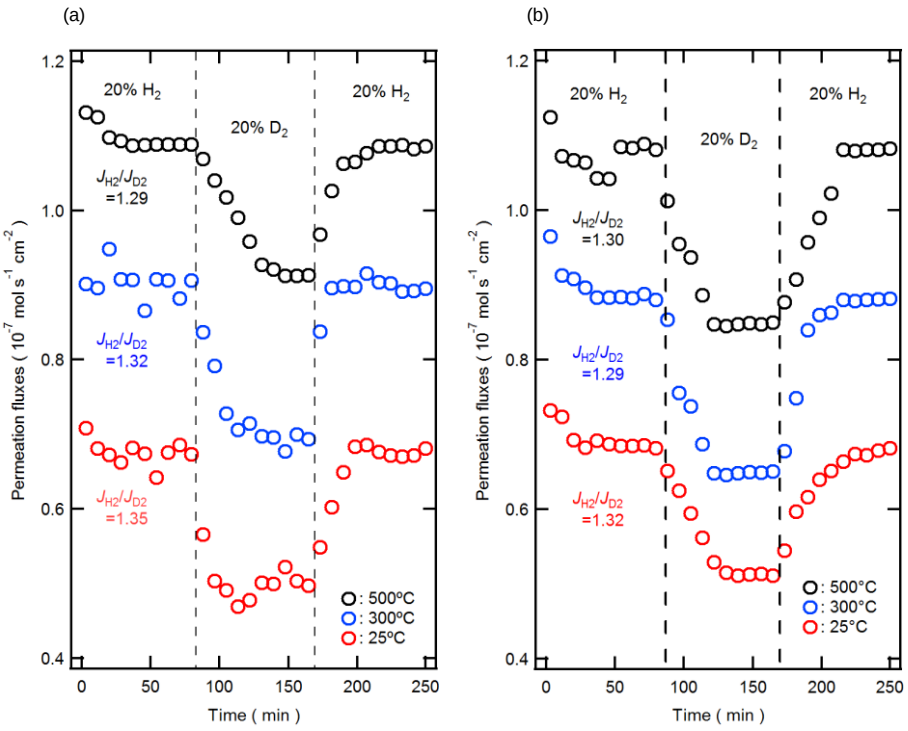


Fig. 3-15 H/D isotope effect on hydrogen fluxes through a 1.5-μm-thick (a) $TiN_{0.7}$ and (b) $TiN_{1.0}$ membrane at 25, 300, and 500°C determined by switching between 20 vol% H_2 and 20 vol% D_2 in N_2.

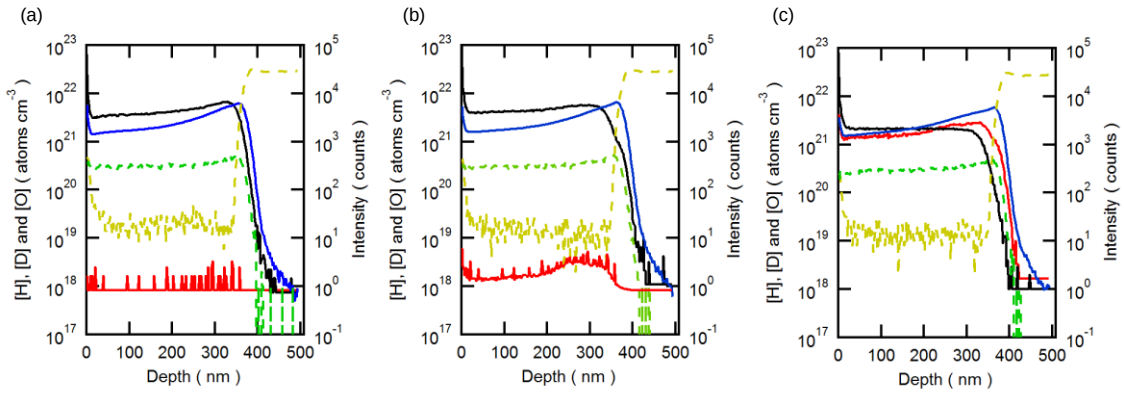


Fig. 3-16 SIMS depth profiles of $TiN_{0.7}$ films (400 nm) on a Si wafer: (a) as-prepared, (b) heated in 50 vol% H_2/Ar at 500°C for 1 h, and (c) heated in 50 vol% D_2/Ar at 500°C for 1 h. The concentrations of H (black line), D (red line), and O (blue line) impurities are plotted in left axis and the signal intensity of constituent TiN (green dashed line) and Si (yellow dashed line) is plotted in right axis.

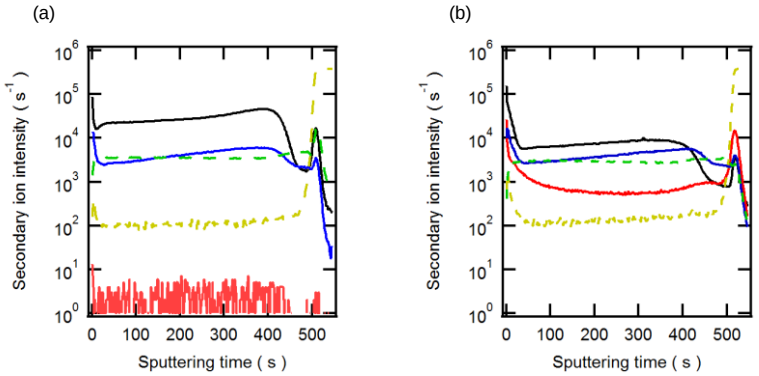


Fig. 3-17 SIMS depth profiles of $TiN_{1.0}$ films (400 nm) on a Si wafer. (a) Heated in 50 vol% H_2/Ar at 500°C for 1 h, and (b) heated in 50 vol% D_2/Ar at 500°C for 1 h, showing the signal intensity of H (black line), D (red line), and O (blue line) impurities and the signal intensity of constituent TiN (green dashed line) and Si (yellow dashed line).

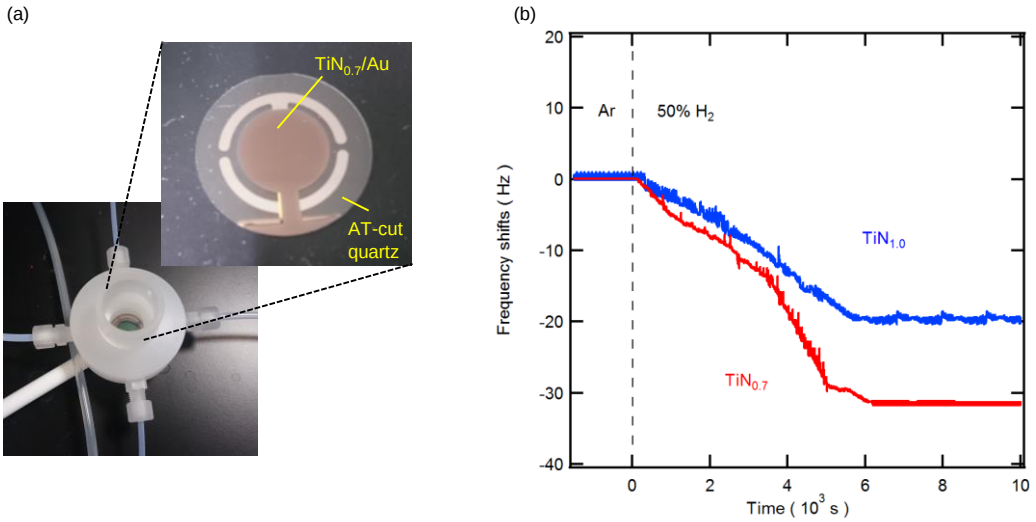


Fig. 3-18 (a) Optical image of homemade gas-tight chamber equipped with QCM and a quartz resonator with Au electrode deposited by $TiN_{0.7}$ film. (b) Response transient of QCM frequency shifts due to hydrogen adsorption on $TiN_{0.7}$ (1050 nm) and $TiN_{1.0}$ films (850 nm) deposited at 200°C on a gold film electrode (1.32 cm^2) of quartz resonator. Measurements were performed by switching from pure Ar to 50 vol% H_2/Ar at 25°C at the time of 0 s. The black dashed line shows a guide for eye of 0 s.

3-3-4 Mobile hydrogen species

Transport and absorption measurements unequivocally demonstrate that nanocrystalline TiN_x membranes realize fast diffusion of hydrogen along grain-boundary pathways. If H_2 dissociates into monoatomic hydrogen upon dissolution in TiN_x, the permeation fluxes driven by diffusion of these monoatomic species should be proportional to the difference of $\sqrt{p_H}$ at the entrance (p_{H2}') and exit (p_{H2}'') sides.[48] The obtained plots of J_{H2} vs (p_{H2}'$^{0.5}$– p_{H2}''$^{0.5}$) deviate significantly from linearity (Fig. 3-19), indicating the atomic hydrogen is not the major mobile species in TiN_x.

The behaviour of hydrogen in metal nitride semiconductors has been extensively studied in the past decades,[49-54] revealing that it acts as a shallow donor (H^+) or acceptor (H^-) if the Fermi energy level is low or high enough relative to ε(+/–) threshold (–4.4 eV vs V. L.), respectively.[54] Protonic hydrogen defects (H^+) are dominant in *p*-type nitride semiconductors, usually forming amide-like defect complexes through association with N anions.[49-52] In Kröger-Vink notation, the above reaction is denoted as

$$N_N^{\times} + H_2(g) \rightarrow (NH_2)_N^{\bullet\bullet} + 2e' \qquad (3\text{-}8)$$

On the other hand, hydridic hydrogen defects (H^-) prevail in *n*-type semiconductors with relatively high Fermi energies due to association with metal (M) cations.[53-56]

$$M_M^{\times} + 1/2\ H_2\ (g) + e' \rightarrow (MH)_M' \qquad (3\text{-}9)$$

Reaction (2) can be rewritten in redox form as:

$$M_M^{\times} + 1/2\ H_2\ (g) \rightarrow (M^{\bullet}H')_M^{\times} \qquad (3\text{-}10)$$

Thus, hydridic hydrogen defects are favoured in TiN, since the Fermi energy level (around –4.1 eV vs. V. L.)[57] is located above the ε(+/–) threshold.

In order to evaluate the chemical states of doped hydrogen, $TiN_{0.7}$ and $TiN_{1.0}$ were

probed by ^{1}H nuclear magnetic resonance (NMR) spectroscopy (Fig. 3-20). Both films show a sharp peak at δ = 1.98 p.p.m., which is assigned to hydrogen as it is more pronounced for samples hydrogenated at 500°C. A broad band centered at δ = 6 p.p.m. is assigned to hydroxyl groups of sacrificial mesoporous γ-Al_2O_3 layers (Fig. 3-20). Fluorite-type TiH_2 is known to take a Ti^{2+}–H^- ionic configuration because of inevitable electron transfer from Ti 3d to H 1s orbitals.[58,59] Interestingly, the chemical shift of doped hydrogen was identical to that of H^- ions of TiH_2 (1.93 p.p.m.)[60] but is much smaller than that of Ti–NH (3.9 p.p.m.)[61] or Ti–NH_2 (13.5 p.p.m.)[62] protons. Moreover, it has been reported that H^- ions in various inorganic metal hydrides typically resonate below 5 p.p.m.[63] These spectroscopic features clarify that the doped hydrogen in TiN_x is present as H^- ions coupled to Ti cations.

The formation of hydridic Ti–H groups is also confirmed by *in situ* Fourier transform infrared reflectance (FT-IR) spectroscopy during H/D isotopic exchange (Fig.3-21 and Fig. 3-22). Pristine $TiN_{0.7}$ films showed Ti–N stretching bands at 1037 cm^{-1} [64] with background signals from adsorbed hydrocarbons, water, and carbon dioxide observed at ~2900, 1650, and 2350 cm^{-1}, respectively.[65] Although amide-like $(NH_2)_N^{\bullet\bullet}$ defect complexes in metal nitrides have been reported to exhibit N–H and N–D stretches at 3000-3300 cm^{-1} and 2100-2300 cm^{-1} streches,[50-52] these bands were not observed for $TiN_{0.7}$. Additionally, the N 1s X-ray photoelectron spectroscopy (XPS) of $TiN_{0.7}$ hydrogenated at 500°C do not provide evidence for the presence of N–H states[66] (Fig. 3-23). Therefore, the combined results of NMR, XPS and FT-IR spectroscopy indicate that protonic H defects do not dominate in TiN_x.

Furthermore, FT-IR measurements during H/D isotopic exchange with H_2 or D_2 gases

(Fig. 3-21) confirm the results above that only hydridic moieties are involved. Switching from H_2 to D_2 at 400°C results in the quick growth of the Ti–D stretching band[67,68] at ~1180 cm^{-1}, with equilibrium being established within 10 min (Fig. 3-21(b)). Although the Ti–H stretch (1600-1650 cm^{-1})[67,68] is masked by the overlap with the background from adsorbed H_2O, the Ti–D band quickly disappears upon switching back to H_2, revealing that D^- ions associated with Ti cations are replaced by H^-. This H/D exchange is observed even at 25°C (Fig. 3-21(c)) and a similar trend is seen by $TiN_{1.0}$ (Fig. 3-22). Thus, all obtained experimental data indicate that the hydride ions of Ti–H groups are the main mobile hydrogen species in TiN_x.

3-3-5 Hydride ion conduction mechanism

The above findings unambiguously demonstrate that nanocrystalline TiN_x membranes exhibit hydride ion conduction due to the formation of Ti–H groups by matrix hydrogenation (a physical model for hydrogen transport in TiN_x is proposed and discussed later). Defect-formation energies (ΔE_{def}) for H_2–TiN systems were calculated by density functional theory (DFT), which yields negative enthalpy for H intake into nitrogen vacancy (V_N) while large positive ones (> 2 eV) for various H–interstitials even after lattice relaxation (Fig. 3-24), indicating that hydrogen introduced into V_N sites, if available, does not migrate fast due to the large potential for jumping through interstitial region between V_N sites. Moreover, QCM-determined {H/Ti} indicates that hydrogen absorbed is not inserted into nitrogen vacancies (Fig. 3-18). Thus, these experimental and theoretical findings imply that the incorporated hydrogen is mainly located outside the crystallites, i.e. near grain boundaries, without being inserted into grain interiors.

To support this hypothesis, the energy of hydrogen adsorption (ΔE_{ad}) on TiN (100) surfaces was calculated by DFT, using $a \times a \times 2\ a$ supercell (Fig. 3-25(a-b), and see 3-2-2(c) for detailed procedures). ΔE_{ad} for H adatoms (H_{ad}) on Ti, N and hollow sites equal –0.16, +1.4 and +0.23 eV, respectively, revealing that hydrogen preferentially chemisorbed on Ti cations to produce terminal Ti–H groups. The above values agree with the results of similar calculations reported elsewhere.[31,69] Ti–H_{ad} bond length is 1.74 Å, being identical to that of the ionic bond between Ti^{3+} and H^-.[31] The corresponding partial density-of-states (p-DOS) reveal that the H impurity level lies just below the Fermi energy level (Fig. 3-25(b)), indicating that H adatoms induce the formation of negatively charged hydridic H defects by electron transfer from Ti 3d to H 1s states, as shown in Eq. (3-10).

The QCM-measured sorption capacity is in close agreement with the hydrogen content needed to fully cover internal grain surfaces by terminal Ti–H groups, with the fractions of surface Ti (F_{Ti}) for (100)-orientated TiN nanocubes with lengths of 14 and 12 nm equalling 0.091 and 0.11, respectively. It has been reported that site occupancy of the Li intercalation in layered materials is roughly described by Langmuir monolayer chemisorption theory.[70] Assuming that the occupation of the surface Ti sites by hydrogen obeys the same behaviour, the 'coverage' of the internal grain surfaces by terminal Ti–H groups is calculated by using calculated ΔE_{ad} to be close to unity under the effective p_{H2} inside membranes equilibrated with gas phase. In this case, {H/Ti} should be close to F_{Ti}. The observed {H/Ti} of $TiN_{0.7}$ (d_{av} = 14 nm) and $TiN_{1.0}$ (d_{av} = 12 nm), are 0.15 and 0.11, respectively, being comparable to the corresponding F_{Ti} values. This analysis dose not account for other crystallographic surfaces and the shape of grains, however, revealing that nanocrystalline films retains enough internal grain interfaces to accommodate the

incorporated hydrogen in the form of terminal Ti–H groups.

Moreover, the temperature and composition dependence of the hydrogen permeability can be explained with the aforementioned model. The concentrations of Ti–H groups are expected to decrease with increasing temperature due to the negative ΔE_{ad} for bonding. Based on data presented in Fig. 3-12(a), the weak thermal activation of J_{H2} at $T \leq 100$°C is ascribed to a decrease of [Ti–H], with the plot slope at $T \geq 250$°C allowing hydride ion conduction diffusion barriers to be estimated, since diffusivity activation is expected to dominate the reduction of [Ti–H] in that region. Based on this framework, the diffusion energy of TiN_x (E_a at $T \geq 250$°C) is found to be much smaller than those of the recently-discovered hydride ion-conductors, such as $La_{2-x-y}Sr_{x+y}LiH_{1-x+y}O_{3-y}$ (68.4 kJ mol^{-1})[71] and BaH_2 (50.1 kJ mol^{-1})[72].

Fig. 3-12(a) and Fig. 3-7 clearly show the E_a values are significantly reduced as the growth orientation is varied from the (100) direction for $x = 1$ to the (111) direction for $x = 0.9$ and 0.7. The diffusion barriers along the Ti–N–Ti and diagonal Ti–Ti paths on a (100) surface are estimated as 1.6 and 0.39 eV from the difference of ΔE_{ad} for Ti and N/hollow sites. Although these values are still larger than the E_a of $TiN_{1.0}$ (0.12 eV), this calculation reveals that Ti–Ti paths are much more favourable than the Ti–N–Ti one. In rock salt structure, the (100) surface features equal amounts of Ti and N, but the (111) surface expose alternatively pure Ti or N closed-packed-layer (Fig. 3-25(c)). Therefore, diffusion along (111) Ti cationic surfaces is much easier than that along (100) ones, because close-packed Ti arrays create a shallow potential at hollow sites because of the short Ti–Ti distances and absence of N anions. At this point, it is not clear whether this difference is solely due to the properties of each crystal surface or to a possible change in

the nature of the grain boundary region, including the space charge layer.[73,74] Both experimental and theoretical results clearly indicate that the grain boundary hopping transport of hydride ions in TiN_x takes place by a bond exchange process between Ti–H terminal groups covering internal grain surfaces. Thus, nanocrystalline TiN_x membranes realise hydrogen permeability by combining hydride ion diffusion along internal grain interfaces with metallic conductivity of the grain bulk.

3-4 Conclusion

Nanocrystalline TiN_x membranes were demonstrated to exhibit room-temperature hydrogen permeability due to enhanced grain boundary diffusion of hydride ions mediated by terminal Ti–H groups on internal grain surfaces with a low activation energy of ~5 kJ mol^{-1}. Hence, the flux of hydrogen through $TiN_{0.7}$ membranes (1×10^{-6} mol cm^{-2} s^{-1} at 25°C) exceeded that observed for Pd membranes at ambient temperature.

The current results propose a guideline for designing hydrogen separation membranes based on hydride ion-electron mixed conductivity of metal nitride nanomaterials. Metallic nitrides which possess Fermi energy levels above the $\varepsilon^+/\varepsilon^-$ threshold[54] are promising hydride ion conductors. These nanocrystalline materials with preferred grain orientation and significantly reduced grain sizes could realise ultrafast hydrogen permeation due to grain-boundary diffusion of hydride ions and metallic conduction of the grain bulk.

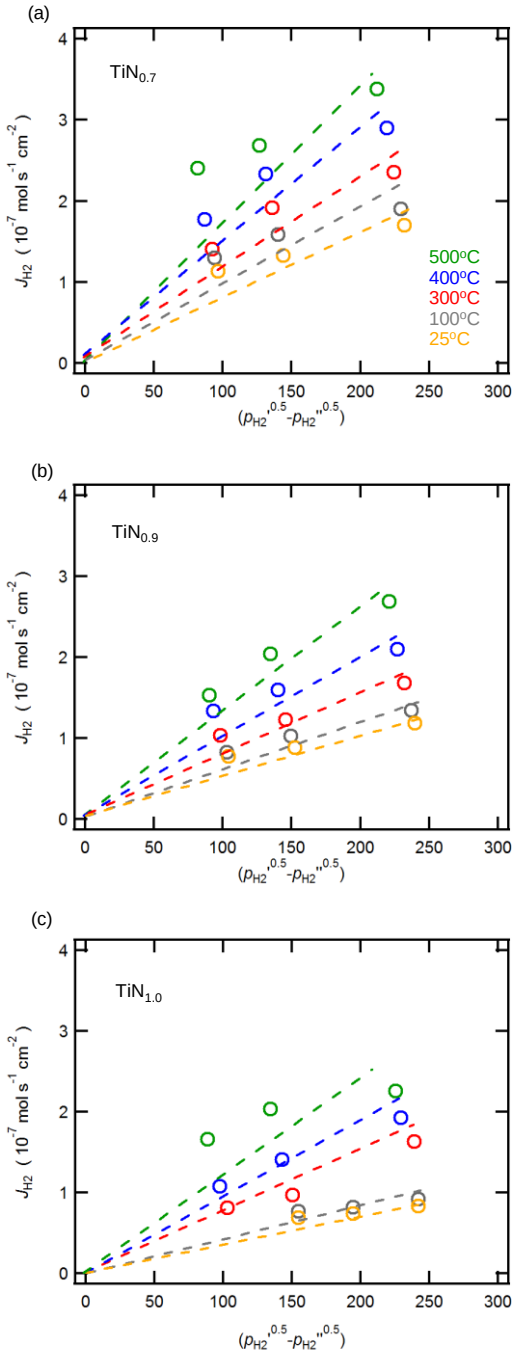


Fig. 3-19 J_{H2} vs p_{H2} plots of TiN_x membranes. (a)-(c) J_{H2} of 2.5 μm-thick TiN_x membranes (x = 0.7 (a), 0.9 (b) and 1.0 (c)), plotted by the way of Sieverts' solubility model.

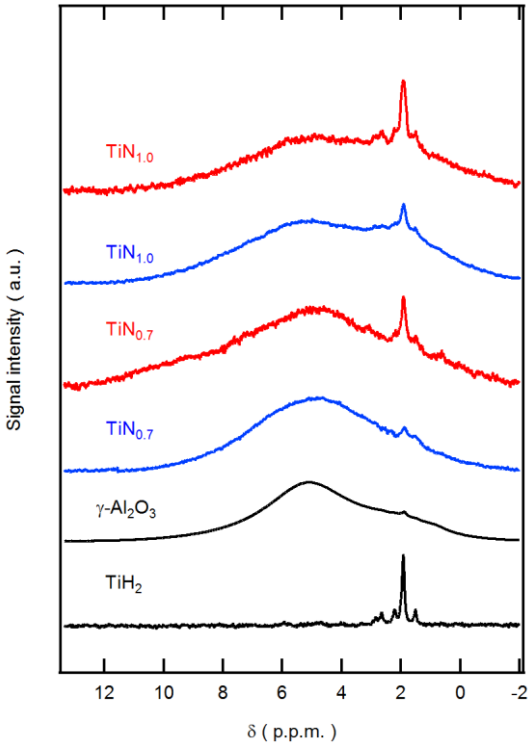


Fig. 3-20 Identification of mobile hydrogen species in TiN_x membranes. ^1H NMR spectra of $TiN_{0.7}$ and $TiN_{1.0}$ films (1 μm) detached from the Si substrate with 100-nm-thick γ-Al_2O_3 sacrificial coating. Red lines represent as-prepared films, and blue lines represent those heated in 50 vol% H_2/Ar at 500°C for 1 h. The black line shows the spectrum of the sacrificial γ-Al_2O_3 layer, with the spectrum of commercial TiH_2 powder also shown as a reference.

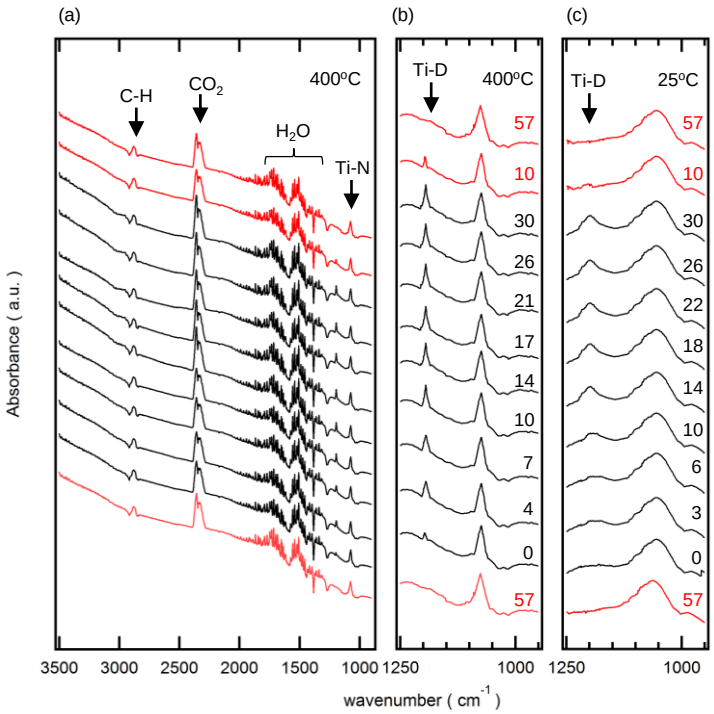


Fig. 3-21 *In situ* FT-IR spectra of $TiN_{0.7}$ membranes (600-nm-thick). The films were initially exposed to a 20 vol% H_2/Ar atmosphere for 1 h, followed by switching to 20 vol% D_2/Ar for 30 min and reverting to 20 vol% H_2/Ar for 1 h. Spectra recorded for H_2 are shown in red, and those obtained for D_2 are shown in black. (a) FT-IR survey spectra (650-3500 cm^{-1}) and (b) expansion of the Ti–D stretching region at 400ºC. (c) The spectra measured at 25ºC. The numbers in (b) and (c) indicate the time (min) to start measuring each spectrum with the time to switch atmosphere being defined by 0 min. The measurement time of a spectrum is about 2.5 min.

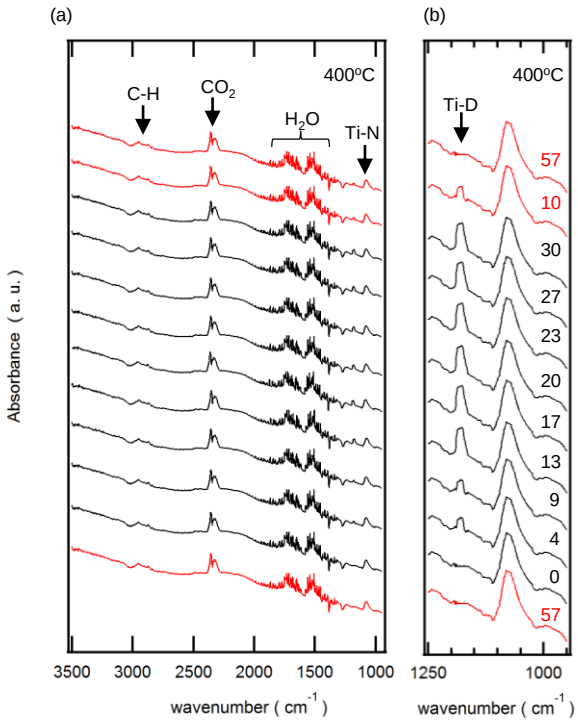


Fig. 3-22 Identification of mobile hydrogen species in $TiN_{1.0}$ by *in situ* FT-IR. (a) *in situ* FT-IR spectra of the 650-3500 cm^{-1} region in 100% H_2 atmosphere at 100-400°C and in 20% D_2 atmosphere at 400°C. (b) expansion of the Ti–D stretching region at 400°C. The numbers in (b) indicate the time (min) to start measuring each spectrum with the time to switch atmosphere being defined by 0 min. The measurement time of a spectrum is about 2.5 min.

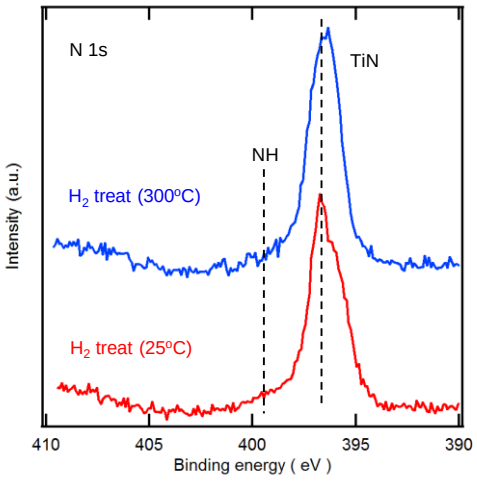


Fig. 3-23 N 1s XPS spectra of 600 nm-thick $TiN_{0.7}$ films treated in 50%-H_2/Ar atmosphere at 25°C and 300°C.

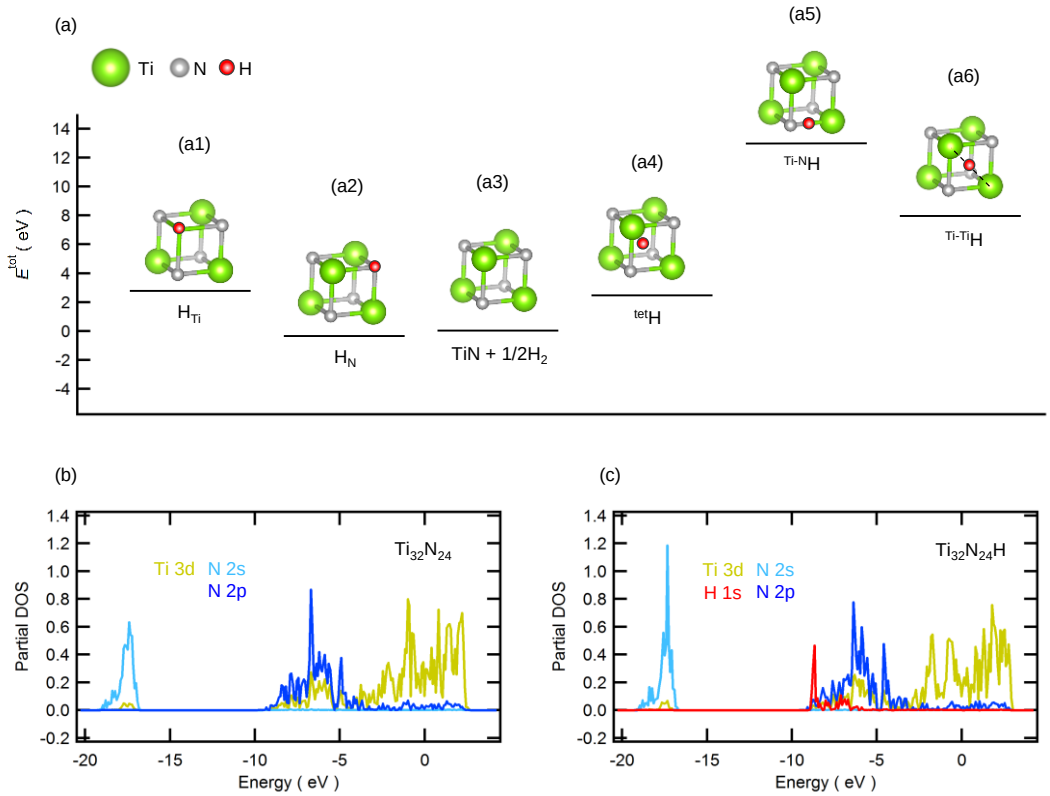


Fig. 3-24 Energy diagrams for rock salt type titanium nitride phases with various nitrogen and hydrogen point defects. (a) The DFT energies calculated for 2×2×2 supercells of various hydrogen defect models. (a3) shows the total energies of the system comprising stoichiometric TiN phase ($Ti_{32}N_{32}$) and 1/2 H_2 gas. (a1) $Ti_{31}N_{32}(H_{Ti})$: H defect occupying a Ti vacancy of Ti-deficient $Ti_{31/32}N$ phase. (a2) $Ti_{32}N_{24}(H_N)$: H defect occupying a N vacancy of N-deficient $TiN_{24/32}$ phase. (a4, a5, a6) $Ti_{32}N_{32}H_1$: TiN phase with an H interstitial at (a4) tetrahedral site of fcc Ti sublattice (^{tet}H), (a5) center of the closest Ti-N bond ($^{Ti-N}$H) and (a6) center of the closest Ti-Ti bond ($^{Ti-Ti}$H). (b), (c) Partial DOS of $Ti_{32}N_{24}$ and $Ti_{32}N_{24}H$. H 1s state is offset by ×2.

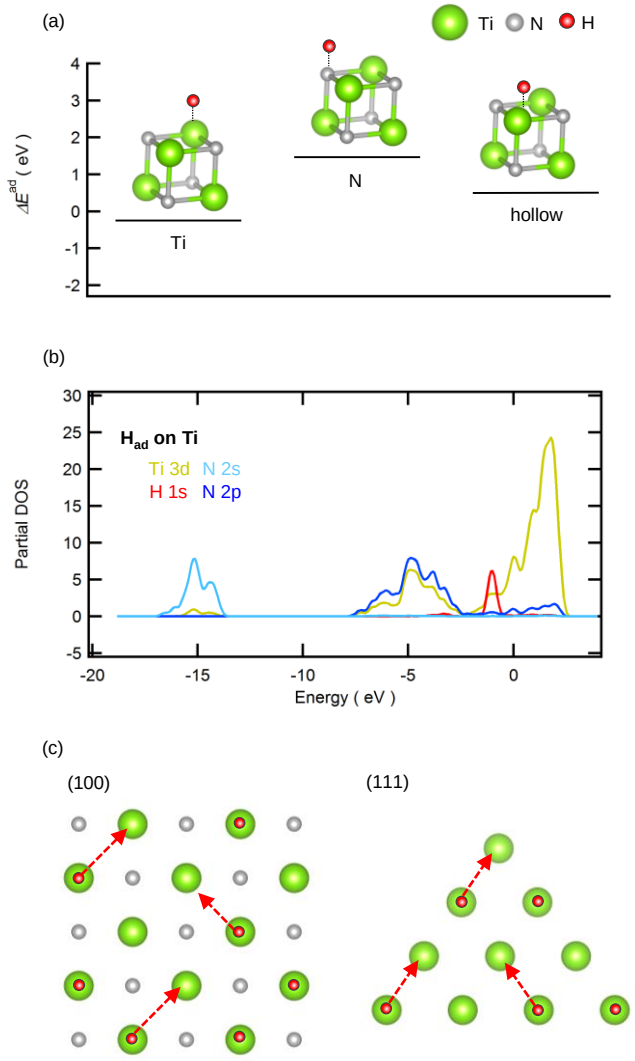


Fig. 3-25 DFT calculations for hydrogen adsorption on TiN surface. (a) DFT energies of hydrogen chemisorption on Ti, N and hollow sites of TiN (100) surfaces. (b) The corresponding partial density-of-states (p-DOS) of TiN supercell with hydrogen chemisorbed on Ti site of (100) surface. (c) Schematic representation of hydride ion hopping on (100) surface built up by alternative stacking of Ti cations and N anions and (111) surface comprising pure Ti closed-packed-layer. Red arrows indicate jump of hydrogen of terminal Ti-H group to neighbor Ti coordination sites.

3-5 References

1. Canonico, S.; Sellman, R.; Preist, C. *Proceedings of the 2009 IEEE International Symposium on Sustainable Systems and Technology, IEEE,* **2009**, ISBN 978-1-244-3456-5.
2. Adams, B. D.; Chen, A. *Mater. Today*. **2011**, 14, 282-289.
3. Cornaglia, L.; Múnera, J.; Lombardo, E. *Int. J. Hydrogen Energy*. **2015**, 40, 3423-3437.
4. Tingelöf, T.; Hedström, L.; Holmström, N.; Alvfors, P.; Lindbergh, G. *Int. J. Hydrogen Energy*. **2008**, 33, 2064-2072.
5. Ockwig, N.W.; Nenoff, T.M. *Chem. Rev*, **2007**, 107, 4078-4110.
6. Saeed, F.; Alsyouri, H. M.; Al-Ghandoor, A.; Al-Husban, Y.; Abdelhadi1, A.; Al-Weissi, S. *Int. J. Electrochem. Sci.* **2013**, 8, 6311-6320.
7. Peters, T. A.; Stange, M.; Bredesen, R. *J. Memb. Sci.* **2011**, 378, 28-34.
8. Holleck, G. L. *J. Phys. Chem*. **1970**, 74, 503-511.
9. Luo, W.; Ishikawa K.; Aoki, K. *J. Alloys. Compd.* **2006**, 407, 115-117.
10. Hashi, K.; Ishikawa, K.; Matsuda T.; Aoki, K. *J. Alloys. Compd*. **2006**, 425, 284-290.
11. Al-Mufachi, N. A.; Rees, N. V.; Wilkens, R. S. *Renew. Sust. Energ. Rev*. **2015**, 47, 540-551.
12. Yun, S.; Oyama, S. T. *J. Memb. Sci*. **2011**, 375, 28-45.
13. Dolan, M. D. *J. Memb. Sci.* **2010**, 362, 12-28.
14. Escolastico, S.; Solis, C.; Kjølseth, C.; Serra, J. M. *Energy Environ. Sci.* **2014**, 7, 3736-3746.

15. Rebollo, E.; Mortalò, C.; Escolástico, S.; Boldrini, S.; Barion, S.; Serra, J. M.; Fabrizio, M. *Energy Environ. Sci.* **2015**, 8, 3675-3686.
16. Escolastico, S.; Seeger, J.; Roitsh, S.; Ivanova, M.; Meulenberg, W. A.; Serra, J. M. *Chem Sus Chem*, **2013**, 6, 1523-1532.
17. Song, S.; Wachsman, E. D.; Rhodes, J.; Dorris, S. E.; Balachandran, U. *Solid State Ionics*, **2004**, 167, 99-105.
18. Zhu, Z.; Sun, W.; Dong, Y.; Wang, Z.; Shi, Z.; Zhang, Q.; Liu, W. *Int. J. Hydrogen. Energy*. **2014**, 39, 11683-11689.
19. Yao J.; Wang, H. *Chem. Soc. Rev.* **2014**, 43, 4470-4493.
20. Oishi, M.; Akoshima, S.; Yashiro, K.; Sato, K.; Mizusaki, J.; Kawada, T. *Solid State Ionics*, **2009**, 180,127.
21. Bouwmeester, H. J. M.; Burggraaf, A. J. *Handbook of Solid State Electrochemistry*; CRC press: Florida, 1996.
22. Kreuer, K.D. *Annu. Rev. Mater. Res.* **2003**, 33, 333-359.
23. Yamazaki, Y.; Blanc, C.; Okuyama, Y.; Buannic, L.; Lucio-Vega, J. C.; Grey, C. P.; Haile, S. M. *Nature. Mater.* **2013**, 12, 647-651.
24. Kim, D.; Miyoshi, S.; Tsuchiya, T.;Yamaguchi, S. *Solid State Ionics*, **2014**, 262, 875-878.
25. Zhou, Y.; Guan, X.; Zhou, H.; Ramados, K.; Adam, S.; Liu, H.; Lee, S.; Shi, J.; Tsuchiya, M.; Fong, D. D.; Ramanathan, S. *Nature.* **2016**, 534, 231-234.
26. Uhlhorn, R. J. R.; Zaspalis, V. T.; Keizer, K.; Burggraaf, A. J. *J. Mater. Sci*. **1992**, 27, 527-552.
27. de Vos, R. M.; Verweij, H. High-selectivity, High-flux silica membranes for gas

separation. *Science*. **1998**, 279, 1710-1711.

28. Itoh, N.; Wu, T. H.; Haraya, K. *J. Membr. Sci*. **1999**, 99, 175-183.
29. Climent-Font, A.; Wätjen, U.; Bax, H. *Nucl. Inst. Methods. Phys. Rev. B.* **1992**, 71, 81-86.
30. Krukau, A. V.; Vydrov, O. A.; Izmaylov, A. F.; Scuseria, G. E. *J. Chem. Phys.* **2006**, 125, 224106.
31. Siodmiak, M.; Govind, N.; Andzelm, J.; Tanpipat, N.; Frenking, G.; Korkin, A. *Phys. Stat. Sol*. **2001**, 226, 29-36.
32. Kresse, G.; Hafner, J. *Phys. Rev. B*. **1993**, 47, 558.
33. Kresse, G.; Hafner, J. *Phys. Rev. B*. **1994**, 49, 14251.
34. Kresse, G.; Furthmüller, J. *Comput. Mat. Sci.* **1996**, 6, 15.
35. Kresse, G.; Furthmüller, *Phys. Rev. B*. **1996**, 54, 11169.
36. Blochl, P. E. *Phys. Rev. B*. **1994**, 50, 17953.
37. Kresse, G.; Joubert, D. *Phys. Rev. B*. **1999**, 59, 1758.
38. Monkhorst, H. J.; Pack, J. D. *Phys. Rev. B*. **1976**, 13, 5188.
39. Persson, C.; Zhao, Y-J.; Lany, S.; Zunger, A. *Phys. Rev. B*. **2005**, 72, 035211.
40. Iwazaki, Y.; Suzuki, T.; Tsuneyuki, S. *J. Appl. Phys.* **2010**, 108, 083705.
41. Ramana. C. V.; White, S.; Esparza, N.; Rangel. V.; Campbell, A. L. *J. Electron. Mater.* **2012**, 41, 3139-3144.
42. Bonanos, N.; Huijser, A.; Poulsen, F. W. *Solid State Ionics*. **2015**, 275, 9-13.
43. Schlom, D. G.; Chen, Long-Qing.; Pan, X.; Schmehl, A.; Zurbuchen. M. A. *J. Am. Ceram. Soc.* **2008**, 91, 2429-2454.
44. Kim, S.; Avila-Paredes, H. J.; Wang, S.; Chen. C. T.; De Souza, R. A.; Martin, M.;

Munir, Z. A. *Phys. Chem. Chem. Phys.* **2009**, 11, 3035-3038.

45. Aoki, Y.; Hashizume, M.; Onoue, S.; Kunitake, T. *J. Phys Chem. B*. **2008**, 112, 14578-14582.
46. Uekawa, N.; Kaneko K. *J. Phys. Chem. B.* **1998**, 102, 8719-8724.
47. Pierson, H. O. *Handbook of Chemical Vapor Deposition: Principle, Technology and Applications (Second Edition)*; Noyes publications: New Jersey, 1999.
48. Hara. S.; Caravella, A.; Ishitsuka, M.; Suda, H.; Mukaida, M.; Haraya, K.; Shimano, E.; Tsuji, T. *J. Memb. Sci.* **2015**, 421, 355-360.
49. Gelhausen, O.; Phillip, M. R.; Goldys, E. M.; Paskova, T.; Monemar, B.; Strassburg, M.; Hoffmann, A. *Phys. Rev. B.* **2004**, 69, 125210.
50. Kleekajai, S. Jiang, F.; Colon, K.; Stavola, M.; Fowler, W. B.; Martin, K. R.; Polimeni, A.; Capizzi, M.; Hong, Y. G.; Xin, H. P.; Tu, C. W.; Basis, G.; Rubini, S.; Martelli, F. *Phys. Rev. B.* **2008**, 29, 085213.
51. Suihkonen, S.; Pimputkar, S.; Speck, J. S.; Nakamura, S. *Appl. Phys. Lett.* **2016**, 108, 202105.
52. Janotti, A.; Zhang, S. B.; Wei, S. H. *Phys. Rev. Lett.* **2002**, 88, 125506.
53. Janotti, A.; Zhang, S. B.; Wei, S. H. Van de Walle, C. G. *Phys. Rev. Lett.* **2002**, 88, 086403.
54. Van de Walle, C. G.; Neugebauer, J. *Nature.* **2003**, 423, 626-628.
55. Holbech, J. D; Nielsen, B. B.; Jones, R.; Sitch, P.; Öberg, S. *Phys. Rev. Lett.* **1993**, 71, 875-878.
56. Sun, W. Qian, C.; He, L.; Ghuman, K. K.; Wong, A. P. Y.; Jia, J.; Jelle, A. A.; O'Brien, P. G.; Reyes, L. M.; Wood, T. E.; Helmy, A. S.; Mims, C. A.; Singh, C. V.; Ozin, G.

A. *Nature Commun.* **2016**, 7, 125531-125539.

57. Fujii, R.; Gotoh, Y.; Liao, M. Y.; Tsuji, H.; Ishikawa, J. *Vacuum* **2006**, 80, 832-835.
58. Hood, D. M.; Pitzer, R.; Schaefer, H. *J. Chem. Phys.* **1979**, 71, 705-712.
59. Tsuchiya, B.; Oku, M.; Sahara, R.; Nagata, S.; Shikama, T.; Kawazoe, Y. *J. Surf. Anal.* **2008**, 14, 424-427.
60. Yan, Y.; Shi. W.; Yuan, Z.; He, S.; Li, D.; Meng, Q.; Ji, H.; Chen, C.; Ma, W.; Zhao, J. *J. Am. Chem. Soc*. **2017**, 139, 2083-2089.
61. Roesky, H. W.; Bai, Y. Noltemeyer, M. *Angew. Chem. Int. Ed.* **1989**, 28, 754-755.
62. Abarca, A.; Gómez-Sal, P.; Martín, Avelino.; Mena, M.; Poblet, J. M.; Yélamos, C. *Inorg. Chem.* **2000**, 39, 642-651.
63. Hayashi, K.; Sushko, P. V.; Hashimoto, Y.; Shluger, A. L.; Hosono, H. *Nature Commun.* **2014**, 5, 35151-35158.
64. Froben, F. W.; Rogge, F. *Chem. Phys. Lett*. **1981**, 78, 264-265.
65. Nyquis, R. A.; Kagel, R. O. *Handobook of Infrared and Raman Spectra of Inorganic Compounds and Organic Salts*; Academic Press: London, 1971.
66. Dementjef, A. P.; de Graaf, A.; de Sanden, M. C. M. V.; Maslakov, K. I.; Naumkin, A. V.; Serov, A. A. *Diamond. Related Mater.* **2000**, 9, 1904-1907.
67. Chertihin, G. V.; Andrews, L. *J. Am. Chem. Soc*. **1994**, 116, 8322-8327.
68. Xiao, Z. L.; Hauge, R. H.; Margrave, J. L. *J. Phys. Chem.* **1991**, 95, 2696-2700.
69. Mario, M.; Milman, V. *Phys. Rev. B*. **2000**, 62, 2899.
70. Conway, B. E. *Electrochim. Acta.* **1993**, 38, 1249-1258.
71. Kobayashi, G.; Hinuma, Y.; Matsuoka, S.; Watanabe, A.; Iqbal, M.; Hirayama, M.; Yonemura, M.; Kamiyama, T.; Tanaka, I.; Kanno, R. *Science*. **2016**, 351, 1314-1317.

72. Verbraeken, M. C.; Cheung, C. Suard, E.; Irvine, J. T. S. *Nature. Mater.* **2014**, 14, 95-100.

73. Maier, J. *Nature. Mater.* **2005**, 4, 805-815.

74. Ramanathan, S. *J. Vac. Sci. Technol. A*. **2009**, 27, 1126-1134.

Appendix: Estimation of hydridic ion conductivity

(a) Comparison with other hydrogen permeable membranes

600 nm-thick $TiN_{0.7}$ and $TiN_{1.0}$ membranes yield the hydrogen fluxes of 5.3×10^{-7} and 1.3×10^{-7} mol cm^{-2} s^{-1} at 25ºC (Table A3-1). These values are several orders of magnitude larger than the fluxes reported for various mixed proton electron conducting ceramics (MPECs) at temperature above 800ºC (Table A3-1). It is concluded that TiN_x membranes are promising candidates of technologically-feasible Pd-alternatives. As shown in Fig. 3-12(b), 200 nm-thick $TiN_{0.7}$ membranes give rise to 1.0×10^{-6} mol cm^{-2} s^{-1} at 25°C, which is still one order of magnitude smaller than the flux of 25 μm-thick state-of-the-art $Pd_{75}Ag_{25}$ membranes (3.0×10^{-5} mol cm^{-2} s^{-1}; Table 3-4) at 450ºC. Moreover, this value is still 2 orders of magnitude smaller than the 2015‘s DOE target (1×10^{-4} mol cm^{-2} s^{-1} at 25°C).[A1]

(b) Hydridic ion conductivity

When a gradient in hydrogen chemical potential ($\nabla\mu_{H2}$) is applied across a mixed hydride anion electron conducting membrane, hydrogen transport must occur from the high to the low hydrogen chemical potential side accompanied by a counter flux of electrons or holes. In such a case, an expression for the hydrogen flux can be derived by[A2]

$$J_{H2} = -\frac{RTt_e\sigma_{H-}}{F^2L}\int_{\ln p_{H2}'}^{\ln p_{H2}''} d\ln p_{H2} \quad \text{(A3-1)}$$

Here, t_e, σ_{H-} and L are electronic transfer number (unity), H^- ion conductivity and

membrane thickness of TiN_x. F is a faraday constant. Prime and double prime denote the entrance and exit side of the membrane, respectively. If H^- anion carrier concentrations are not dependent on p_{H2} in the finite range, Eq. (A3-1) indicate the slope of the J_{H2} vs $\ln[p_{H2}'/p_{H2}'']$ plots allow the H^- anion conductivity, σ_{H-}. p_{H2}'' corresponding to the pressure at the film/support interfaces can be available under steady state condition by using a flux calibration curve of porous alumina support (Fig. 3-6).[A3] The detailed explanation is noted in Experimental section. The assumption would be reasonable in the case of TiN_x, because small p_{H2} dependence of Ti-D IR bands implies that the deviation of the relative peak intensity, [Ti-D], is within 20% in the measure p_{H2} range (Fig. A3-1). All membranes reveal a good linear relationship between J_{H2} and $\ln[p_{H2}'/p_{H2}'']$ (Fig. A3-2(a-c)), and thus, the permeability of TiN_x is well replicated by ion electron mixed conducting model. In case of hydrogen permeable metals, the hydrogen solubility obeys Sieverts' law[A4] and the corresponding permeation fluxes should be proportional to $p_{H2}^{0.5}$ term. J_{H2} vs $(p_{H2}'^{0.5} - p_{H2}''^{0.5})$ plots of $TiN_{0.7}$ are largely deviated from a straight line passed through an origin (Fig. 3-19), indicating that hydrogen permeation is not driven by the hydrogen dissolution unlike metallic alloys. Accordingly, it is evident that hydride anion diffusion involves hydrogen permeation in TiN_x.

σ_{H-} thus obtained obeys Arrhenius type linear relationship in a wide temperature range in every composition (Fig. A3-2(d)). σ_{H-} becomes larger and the related E_a smaller at smaller x. $TiN_{0.7}$ possesses σ_{H-} of 1.5×10^{-4} S cm^{-1} even at 100°C, and this value is very close to the conductivity of fast H^- ion conductor $L_{2-x}Sr_xLiH_{2-x}O_2$ at 300°C (2×10^{-4} S cm^{-1}).[A5]

Table A3-1. Summary of recent reports for various hydrogen separation membranes.

Materials	L / μm	T / °C	E_a / kJ mol^{-1}	J_{H2} / mol cm^{-2} s^{-1}	σ_{H-}/S cm^{-1}	Ref
$TiN_{0.7}$ (this work)	0.6	500	5.8	9.0×10^{-7}	2.5×10^{-4}	
		rt		5.3×10^{-7}		
$TiN_{0.9}$ (this work)	0.6	500	6.3	7.6×10^{-7}	1.6×10^{-4}	
		rt		3.3×10^{-7}		
$TiN_{1.0}$ (this work)	0.6	500	12	6.5×10^{-7}	1.4×10^{-4}	
		rt		1.1×10^{-7}		
Pd	6	480	26	2.6×10^{-5}		A5
$Pd_{75}Ag_{25}$	25	450	-	3.0×10^{-5}		A6
$Nb_{56}Ti_{23}Ni_{21}$	800	400	-	1.4×10^{-6}		A7
V	2000	425	-26	1.4×10^{-7}		A8
Ta	500	420	-20	2.4×10^{-7}		A9
Nb	500	420	-18	6.0×10^{-7}		A9
Ti	500	100	59	2.4×10^{-12}		A10
$SrCe_{0.95}Eu_{0.05}O_{3-\delta}$	1720	650	66	7.5×10^{-10}		A11
$BaCe_{0.95}Nd_{0.05}O_{3-\delta}$	700	925	-	1.9×10^{-8}		A12
$BaCe_{0.65}Zr_{0.20}Y_{0.15}O_{3-\delta}$	650	755	91	2.0×10^{-7}		A13
-$Ce_{0.85}Gd_{0.15}O_{2-\delta}$						
Ni-$Ba(Ce_{0.9}Y_{0.1})O_{3-\delta}$	230	800	-	5.7×10^{-7}		A14
Ni-$BaCe_{0.85}Tb_{0.05}Zr_{0.1}O_{3-\delta}$	500	800	-	1.3×10^{-7}		A15

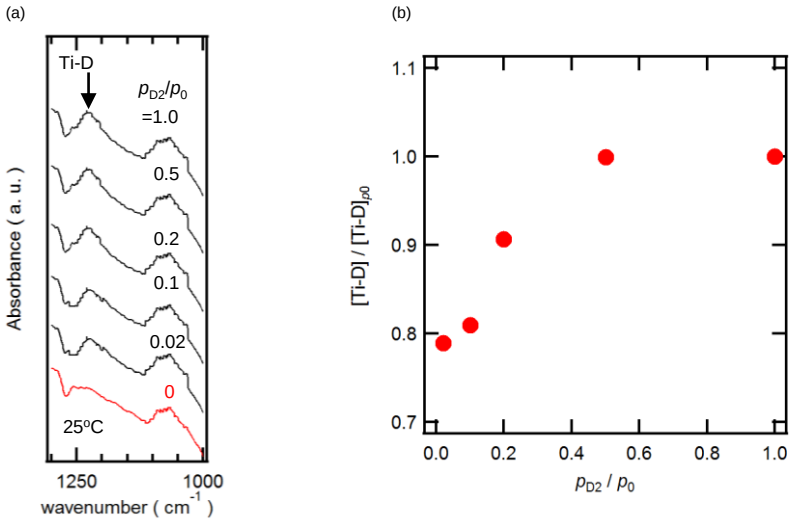


Fig. A3-1 *in situ* FT-IR spectrum of $TiN_{0.7}$. (a) p_{D2} dependence of Ti-D absorption bands at 25°C. (b) Relationships between the relative peak intensity, [Ti-D], and p_{D2} in (a). The peak intensities are normalized by ones at p_{D2}= p_0 =101 kPa.

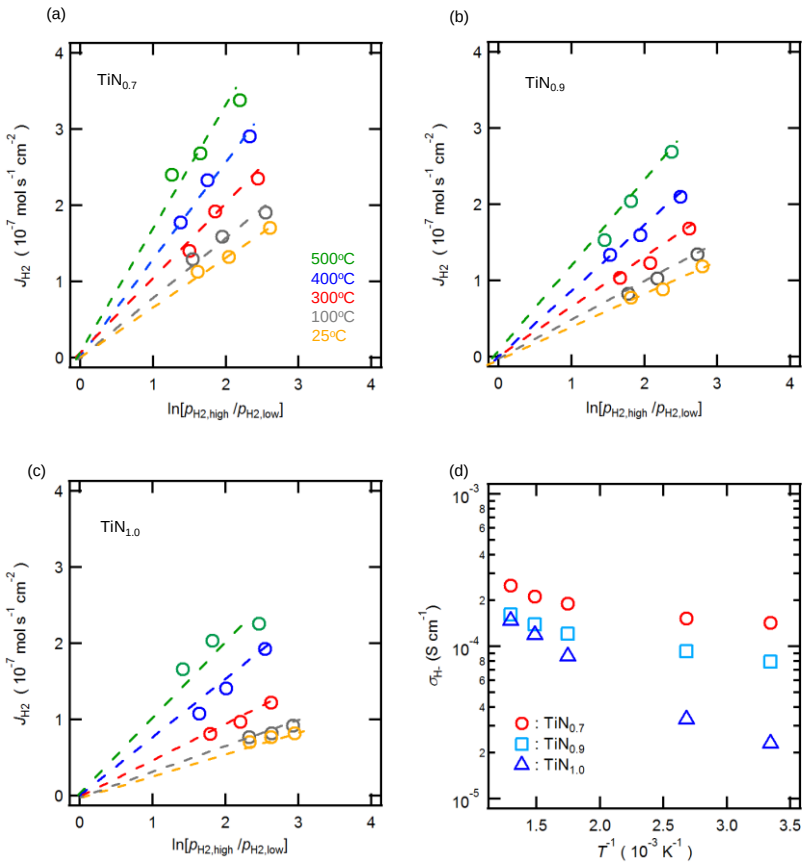


Fig. A3-2 p_{H2} dependence of hydrogen fluxes of TiN_x membranes fitted to ion electron mixed conducting mechanism. J_{H2} of 2.5 μm thick TiN_x membranes (x = 0.7 (a), 0.95 (b) and 1.0 (c)), plotted by way of ion electron mixed conductors (see Eq. (A3-1)). p_{H2}' denote p_{H2} at hydrogen supply side and p_H'' at permeation side. The fluxes are measured at p_{H2}' of 30, 50 and 100 kPa. (d) Arrhenius plots of the H^- ion conductivity σ_{H^-} determined from a slope of the plots in (a), (b) and (c).

References of Appendix

A1. Drioli, E.; Barbieri, G. *Membrane Engineering for the Treatment of Gases: Volume 2: Gas-separation Problems Combined with Membrane Reactors (1st Edition)*; RSC Publishing: United Kingdom, 2011.

A2. H. J. M. Bouwmeester; A. J. Burggraaf, "*Dense Ceramic Membranes for Oxygen Separation" in Handbook of Solid State Electrochemistry*; CRC press: Boca Raton, 1997

A3. Itoh, N.; Wu, T. H.; Haraya, K. *J. Membr. Sci*. **1999**, 99, 175-183.

A4. Cornaglia, L.; Múnera, J.; Lombardo, E. *Int. J. Hydrogen Energy*. 2015, 40, 3423-3437.

A5. Zhang, X., Xiong, G.; Yang, W. *J. Membr. Sci*. **2008**, 314, 226-237.

A6. Xie, D.; Yu, J.; Wang, F.; Zhang, N.; Wang, W.; Yu, H.; Peng, F.; Park, A. H. A. *J. Hydrogen Energy*. **2011**, 36, 1014-1026.

A7. Luo, W.; Ishikawa K.; Aoki, K. *J. Alloys. Compd.* **2006**, 407, 115-117.

A8. Buxbaum, R. E.; Markerb, T. L. *J. Membr. Sci*. **1993**, 85, 29-38.

A9. Buxbaum, R. E.; Kinney, A. B. *Ind. Eng. Chem. Res.* **1996**, 35, 530-537.

A10. Millenbach, P.; Givon, M. *J. Less. Common. Metals.* **1982**, 92, 339-342.

A11. Song, S.; Wachsman, E. D.; Rhodes, J.; Dorris, S. E.; Balachandran, U. *Solid State Ionics*, **2004**, 167, 99-105.

A12. Cai, M.; Liu, S.; Efimov, K.; Caro, J.; Feldhoff, A.; Wang, H. *J. Membr. Sci*. **2009**, 343, 90-96.

A13. Rebollo, E.; Mortalò, C.; Escolástico, S.; Boldrini, S.; Barion, S.; Serra, J. M.;

Fabrizio, M. *Energy Environ. Sci.* **2015**, 8, 3675-3686.

A14. Kim, H.; Kim. B.; Lee, J.; Ahn, K.; Kim, H. R.; Yoon, K. J.; Kim, B. K.; Cho, Y. W.; Lee, H. W.; Lee, J. H. *Ceram. Int*. **2014**, 40, 4117-4126.

A15. Wei, Y.; Xue, J.; Fang, W.; Chen, Y.; Wang, H.; Caro, J. *Chem. Commun*. **2015**, 51, 11619-11621.

Chapter 4

Improved hydrogen permeability of TiN_x nanocrystalline membranes by microstructural tailoring

4-1 Introduction

In Chapter 3, It has been demonstrated that TiN_x nanocrystalline membranes are alternative hydrogen membrane based on the novel transport mechanism featured by ambipolar diffusion of hydride ions and electrons. The hydrogen fluxes of the sub-mm thick films are much higher than that of technological-limit 5-μm-thickness ultrathin Pd membranes at room temperature due to the extremely-lowered activation energy for diffusion (~10 kJ mol^{-1}), however, the value is still lower than the DOE flux rate target (1×10^{-4} mol cm^{-2} s^{-1} at 25°C).[1]

In Chapter 3, it was demonstrated that titanium nitride (TiN_x; x = 0.7, 0.9, and 1.0) nanocrystalline membranes exhibit hydrogen permeability levels exceeding that of Pd metals at 25°C due to the fast diffusion of hydridic ions. This observation is ascribed to the following reasons. 1) NMR and FT-IR spectroscopy confirmed that Ti-H group are dominantly formed in hydrogenated TiN_x membranes, revealing that hydrogen favour to form hydridic hydrogen defects (H^-) via associated with Ti cations attributed to the relatively high Fermi energy levels (–4.1 eV vs V. L.). 2) Hydrogen permeability and

solubility of stoichiometric $TiN_{1.0}$ was not far different from highly-N-deficient $TiN_{0.7}$, which prove that hydridic diffusion was not mediated via nitrogen anion vacancies. 3) Permeability is increased by reducing crystallite sizes, indicating grain boundaries preserve the diffusion pathway of hydridic ions. According to brick layer models,[2,3] grain boundary diffusion is linearly correlated with grain boundary volumes which can be given by a function of the inversed grain sizes. Hence, it is of fundamental and technological importance to investigate the relationship between crystallite sizes and hydrogen permeability in TiN_x systems. In this chapter, the hydrogen solubility was demonstrated and thus the related permeability of TiN_x (x = 0.7, 1.0) nanocrystalline membranes are remarkably enhanced by decreasing nanocrystalline grain sizes, which provides a clear evidence for the interfacially-controlled diffusion of hydride ions. (111)-oriented $TiN_{0.7}$ membranes possess higher hydrogen solubility than (100)-oriented $TiN_{1.0}$ because the population of Ti cations, i.e. a coordination site for hydride on (111) surface are several times higher than that of (100) surface, which results in the hydrogen permeability of (111)-oriented $TiN_{0.7}$ membranes consisting sub 10 nm-sized crystallites is three orders of magnitude higher than equivalent thickness Pd at room temperature.

4-2 Experimental

4-2-1 Hydrogen permeability tests

Nonstoichiometric TiN_x membranes (x = 0.7 and 1.0) were deposited by reactive sputtering in an ultrahigh vacuum chamber system (ULVAC S-3000). The sputtering

condition is written in 3-2-1(b). In order to investigate the particle size dependence of the hydrogen permeation, the TiN_x crystal growth rate was controlled by changing substrate temperature to 25, 200 and 500°C. The thickness of the membranes was adjusted in 600 nm by controlling sputtering time.

To investigate a hydrogen permeability of TiN_x with different nanocrystalline size, the membranes were fabricated on a porous alumina support consisting of macroporous α-Al_2O_3 sintered pellets with mesoporous γ-Al_2O_3 top layer. The procedure to produce porous Al_2O_3 support was written in 3-2-1(a).[4,5]

Hydrogen permeability of TiN_x membranes were carried out with a homemade gas-tight chamber system equipped with a gas chromatography (GL Sciences GC-4000). A TiN_x membrane sample was sealed in specially-designed sample holder using carbon sheet gaskets and placed in an electrical furnace to controlled temperature. The details of measurement condition are written in 3-2-1(c).

4-2-2 Characterization techniques

Phase purities were determined by X-ray diffraction (XRD; RIGAKU RINT2200 diffractometer with Cu Kα radiation). The above measurements were performed for 500-nm-thick TiN_x films deposited on a Si wafer modified with a 100 nm-thick γ-Al_2O_3 layer.

The morphologies of TiN_x membranes were characterised by transmission electron microscopy (TEM; JEOL JFM-ARM-200F). High-resolution images taken from corresponding specimens are prepared by ion-milling process (JEOL AT-12310). The 1.2 cm × 1.2 cm TiN_x/γ-Al_2O_3/Si samples pasted together with petropoxy resin were polished at ~0.1 mm by hands, and thinned from both sides constantly rotated, using Ar^+ ion beam

at 3 kV at a glancing incidence angle of about 5°.

^{1}H magic-angle-spinning nuclear magnetic resonance (MAS-NMR) spectroscopy was performed using a JEOL JNM-ECAII spectrometer. The procedure of powder TiN_x samples and measurement conditions were written in 3-2-2(a).

Amount of the hydrogen absorbed are measured with a home-made gas flow chamber system equipped with a 5 MHz quartz crystal microbalance (QCM) device (USI System) at 25°C. The quartz crystal resonator (1.0 cm∅) have an Au film electrode (1.32 cm^2). The TiN_x films are deposited directly on the Au film electrode through a shadow mask at 25 and 200°C. The amount absorbed are determined by the shift of the resonance frequency as switched from pure Ar to 50%-H_2/Ar gases at 25°C.

4-3 Results and Discussion

4-3-1 Fabrication of TiN_x membranes

In Chapter 3, nanogranular membranes of single-phase NaCl-type TiN_x (x = 0.7 and 1.0) have successfully fabricated by reactive sputtering of a pure Ti metal target in N_2/Ar mixed process gas at 0.9 Pa (See Chapter 3). According to the results of a broad survey of the effect of N_2 gas concentration on the developed films, we successfully optimized the N content at each deposition temperature, as summarized in Table 4-1. The results indicated that higher N_2 concentrations were required in the gas phase for deposition at lower substrate temperatures, probably due to the lower nitridation reaction rates. Hereafter, TiN_x membranes deposited at 500, 200, and 25ºC are denoted as TiN_x-500,

TiN_x-200, and TiN_x-25 (x = 0.7 or 1.0), respectively.

The highly N-deficient $TiN_{0.7}$ membranes always exhibited (111) preferred orientation during grain growth regardless of the deposition temperatures, while stoichiometric $TiN_{1.0}$ membranes had a (100) orientation at all deposition temperatures, as confirmed by X-ray diffraction (XRD) (Fig. 4-1). The full-width-at-half-maximum (FWHM) values of the (111) and (100) peaks increased with decreasing temperature; this was attributed to a reduction in the crystallite sizes at lower deposition temperatures. The average grain sizes (d_{av}) of TiN_x-500, -200, and -25 were 23, 13, and 7 nm for x = 0.7, and 22, 12, and 8 nm for x = 1.0, respectively, as calculated from the XRD data using the Scherrer equation (Table 4-1).

Fig. 4-2(a) shows a cross-sectional scanning electron microscopy (SEM) image of a 600-nm $TiN_{0.7}$ membrane deposited on a porous alumina support, indicating three distinct layers: the macroporous α-Al_2O_3 substrate, mesoporous γ-Al_2O_3 middle layer (1 μm thickness), and dense TiN_x membrane layer (600 nm thickness). The middle layer retained numerous nanometer-sized pores in the interstitial spaces of the nanoparticle networks and the dense TiN_x films were uniformly formed over the mesoporous layer without intermixing at the interface (Fig. 4-2(b)). Moreover, transmission electron microscopy (TEM) images revealed that the TiN_x layer was composed of rectangular crystallites with dimensions of a few tens of nanometers, which became smaller with decreasing deposition temperature as 20, 14, and 7 nm for $TiN_{0.7}$-500, -200, and -25, respectively (Fig. 4-2(c-e), Fig. 4-3 and Table 4-1). The crystallite sizes observed by TEM were in good agreement with the d_{av} values determined by XRD.

4-3-2 Hydrogen permeability

In our previous reports, hydrogenated TiN_x-500 was found to exhibit a sharp peak at 1.93 p.p.m. in ^1H nuclear magnetic resonance (NMR) spectroscopy, attributed to the hydride ions coupling with Ti cations (Chapter 3). The TiN_x-25 films in this study also showed similar spectroscopic features (Fig. 4-4); all films showed a sharp peak at δ = 1.93 p.p.m., together with a broad peak of hydroxyl groups of sacrificial mesoporous γ-Al_2O_3 layers centered at δ = 5 p.p.m.; the former of which was identical to the hydrogen defects in TiN_x as the peak intensity clearly increased with hydrogenation. The δ values were clearly different from the features of protonic hydrogens in Ti–NH (3.9 p.p.m.)[6] or Ti–NH_2 (13.5 p.p.m.)[7]. Hayashi *et al.* reported that a ^1H-chemical shift $\delta_{iso}(H^-)$ of metal hydride systems can be correlated with their M–H bond length using the following empirical equation:[8-11]

$$\delta_{iso}\ (H^-)\ (ppm) = 0.070\ d_{M-H}\ (pm) - 11.5(\pm 2) \qquad (4\text{-}1)$$

Using the Ti–H bond length (174 pm)[12], Eq. (4-1) was used to calculate the δ_{iso} (H^-) value of about 1.68 p.p.m., which was very close to the observed peak (1.93 p.p.m.), confirming that hydridic hydrogen defects were favorably formed in TiN_x by the following hydrogenation reaction:

$$Ti_{Ti}^{\times} + 1/2\ H_2\ (g) + e' \rightarrow (TiH)_{Ti}' \qquad (4\text{-}2)$$

To determine the hydrogen permeability and selectivity of the TiN_x membranes, 50 vol%-H_2/N_2 or 50 vol%-He/N_2 mixtures were supplied to the surface of the membranes and the gas exiting from the support side was analysed by gas chromatography. All membranes showed very small nitrogen fluxes (J_{N2}; ~3×10^{-8} mol s^{-1} cm^{-2}), which were at least two orders of magnitude smaller than the hydrogen permeation fluxes (J_{H2}; see Fig.

4-5(a-b)), confirming that TiN_x membranes show selective hydrogen permeation by hydridic conductivity. Helium fluxes (J_{He}) from TiN_x-500 membranes were nearly zero, despite the fact that He molecules are smaller than those of H_2 (Fig. 3-12(a)), thus proving that the observed hydrogen transport was not via pinholes or cracks.

Fig. 4-5(a) and (b) show the J_{H2} of 600 nm TiN_x-25, -200, and -500 (x = 0.7 and 1.0) membranes, indicating that the hydrogen permeability of the TiN_x membranes was significantly enhanced with decreasing average crystallite size, d_{av}. For both $TiN_{0.7}$ and $TiN_{1.0}$, J_{H2} values increased equally at every temperature with decreasing d_{av}; the temperature dependency remained unchanged with decreasing d_{av}, providing clear evidence for interfacially controlled hydride ion diffusion in the nanocrystalline matrices. For $TiN_{0.7}$, J_{H2} showed an Arrhenius-type linear temperature dependence at $T \geq 250$°C, which became much less pronounced at $T \leq 200$°C due to the reduced mobility of hydridic ions with temperature due to the negative formation energy of Ti-H groups (Chapter 3). The ratio between hydrogen and deuterium permeation fluxes, J_{H2}/J_{D2}, through the TiN_x-25 membranes was close to the reciprocal ratio of root mass, $\sqrt{M_D}/\sqrt{M_H} \sim 1.4$ (Fig. 3-15), providing a signature of diffusion-limited hydrogen permeation.[13] Hence, the activation energies (E_a) observed for $T \geq 250$°C must have corresponded to the diffusion energy of hydridic defects and the values for $TiN_{0.7}$-500 and -200, and -25 equal to 5.5, 5.6, and 5.8 kJ mol^{-1}, respectively (Table 4-2). (100)-oriented $TiN_{1.0}$ showed more pronounced temperature dependent J_{H2} than (111)-oriented $TiN_{0.7}$ for $T \geq 200$°C, which was attributed to the relatively large E_a (8.9–12 kJ mol^{-1}). Therefore, the permeability of the former was several times smaller than that of the latter at ambient temperature (Table 4-2).

According to the brick layer model, where cubic grain cores are arranged on a simple

cubic lattice (with length d_{av}) separated by homogeneous grain boundary layers (Fig. 4-8(a)),[2,14] the grain boundary volumes of nanocrystalline materials are proportional to their volumetric surface areas, which are correlated with d_{av}^{-1}. In $TiN_{0.7}$, decreasing d_{av} from 23 ($TiN_{0.7}$-500), to 13 ($TiN_{0.7}$-200), to 7 nm ($TiN_{0.7}$-25) increased J_{H2} from 1.5 to 2.2 times, respectively, indicating that the J_{H2} ratios of $TiN_{0.7}$-200 to $TiN_{0.7}$-500 and $TiN_{0.7}$-25 to $TiN_{0.7}$-500 were roughly equivalent to the inverse ratios of d_{av}, i.e. $(13\ nm/23\ nm)^{-1}$~1.8 and $(7\ nm/\ 23\ nm)^{-1}$~3.3, respectively. Similarly, the ratios of J_{H2} values obtained for $TiN_{1.0}$-25 to $TiN_{1.0}$-500 and $TiN_{1.0}$-200 to $TiN_{1.0}$-500 were approximately equal to 2.7 and 1.6, respectively, which was in agreement with the corresponding d_{av}^{-1} ratios, $(8\ nm/20\ nm)^{-1}$~2.5 and $(12\ nm/22\ nm)^{-1}$~1.8, respectively. The linear scalability of J_{H2} vs. d_{av}^{-1} clearly proved that the hydridic conduction in TiN_x occurs via interfacial grain boundary pathways (Fig. 4-5(c-d)).

Table 4-1. RF reactive sputtering conditions of TiN_x (x = 0.7 and 1.0) nanocrystalline membranes and their average grain size (d_{av}) of the corresponding membranes deposited on γ-Al_2O_3/Si wafers, as determined by XRD and TEM.

samples	Substrate temperature / °C	N_2 concentration / %	d_{av} (XRD) / nm	d_{av} (TEM) / nm
$TiN_{0.7}$-500	500	2.5	23	20
$TiN_{0.7}$-200	200	4	13	14
$TiN_{0.7}$-25	25	10	7	7
$TiN_{1.0}$-500	500	100	22	20
$TiN_{1.0}$-200	200	100	12	12
$TiN_{1.0}$-25	25	100	8	9

Table 4-2. Structural and hydrogen-transport properties of 600-nm TiN_x (x = 0.7 and 1.0) membranes.

samples	d_{av} (XRD) / nm	Crystal orientation	Hydrogen flux at 500°C / mol cm^{-2} s^{-1}	Hydrogen flux at rt / mol cm^{-2} s^{-1}	E_a of permeability / kJ mol^{-1}	composition
$TiN_{0.7}$-500	23	(111)	9.0×10^{-7}	5.3×10^{-7}	3.1 ($T \leq 200$°C) 5.8 ($T \geq 250$°C)	–
$TiN_{0.7}$-200	13	(111)	1.1×10^{-6}	7.8×10^{-7}	3.0 ($T \leq 200$°C) 5.6 ($T \geq 250$°C)	$TiN_{0.7}H_{0.15}$
$TiN_{0.7}$-25	7	(111)	1.6×10^{-6}	1.0×10^{-6}	3.1 ($T \leq 200$°C) 5.5 ($T \geq 250$°C)	$TiN_{0.7}H_{0.22}$
$TiN_{1.0}$-500	22	(100)	6.5×10^{-7}	1.3×10^{-7}	6.0 ($T \leq 100$°C) 12 ($T \geq 150$°C)	–
$TiN_{1.0}$-200	12	(100)	1.0×10^{-6}	2.6×10^{-7}	6.1 ($T \leq 200$°C) 9.8 ($T \geq 250$°C)	$TiN_{1.0}H_{0.11}$
$TiN_{1.0}$-25	8	(100)	1.3×10^{-6}	4.9×10^{-7}	6.1 ($T \leq 150$°C) 8.9 ($T \geq 200$°C)	$TiN_{1.0}H_{0.14}$

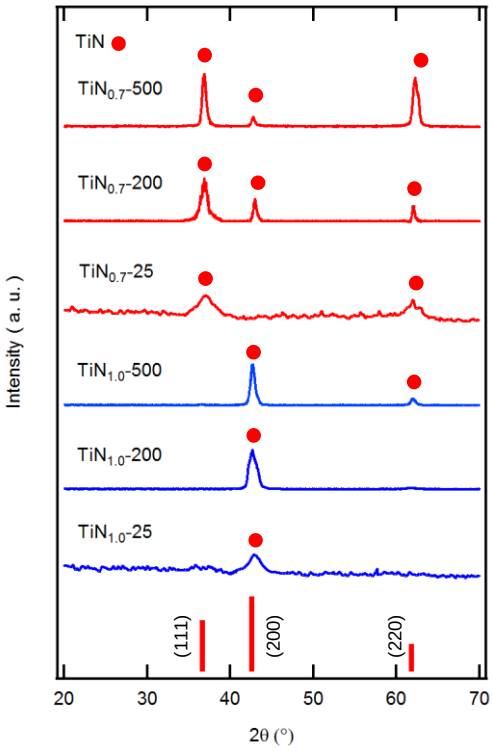


Fig. 4-1 XRD patterns of 500 nm-thick TiN_x (x = 0.7 and 1.0) films deposited on a Si wafer modified by γ-Al_2O_3 mesoporous layer (100 nm thickness). Sputtering was performed at 25, 200 and 500°C.

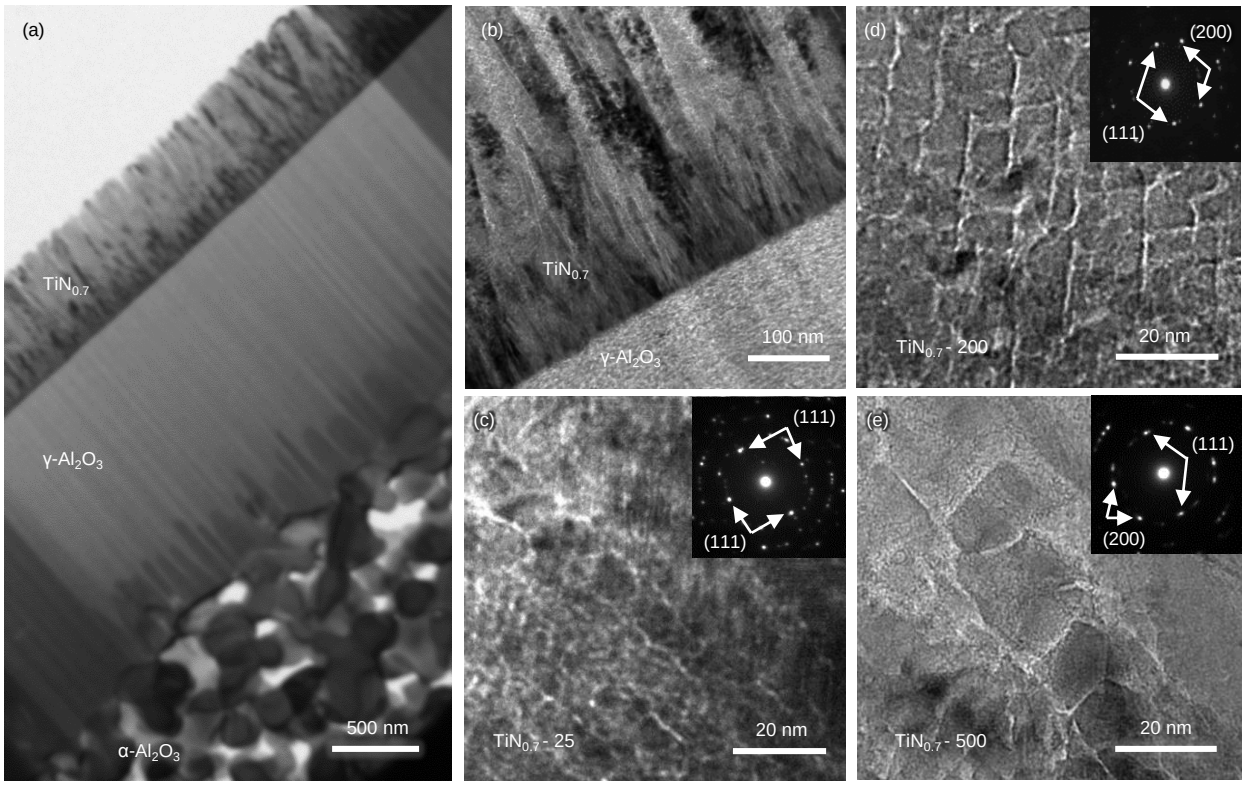


Fig. 4-2 (a) Cross-sectional TEM image of a membrane devices comprising sputter-deposited $TiN_{0.7}$ (top layer, 600 nm), sol-gel-derived mesoporous γ-Al_2O_3 (middle layer, 1 µm), and macroporous α-Al_2O_3. (b) Cross-sectional TEM image of an area close to the $TiN_{0.7}$/γ-Al_2O_3 interface. High-resolution TEM image revealing the nanogranular morphology of $TiN_{0.7}$ deposited at (c) 25, (d) 200 and (e) 500°C. In inset of (c)-(e), the electron diffraction (ED) patterns recorded at a point in the images are also shown.

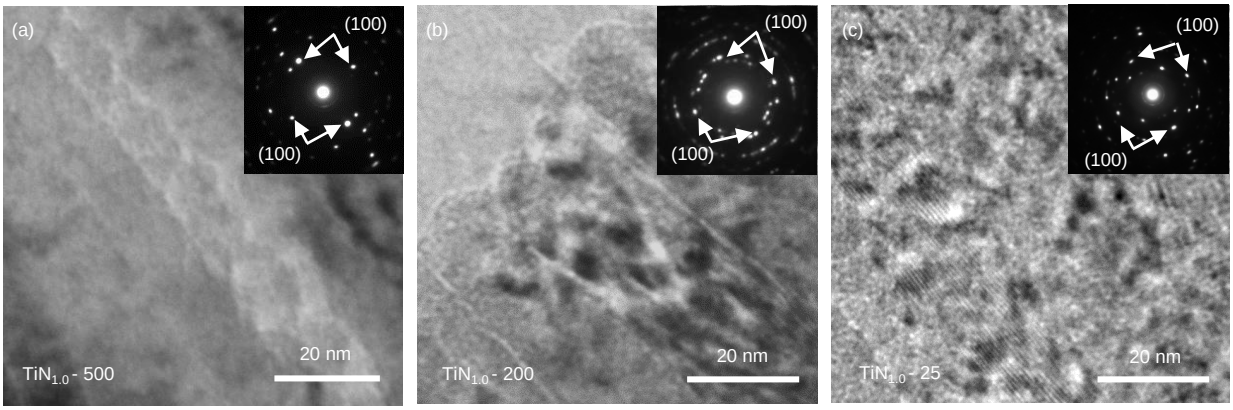


Fig. 4-3 High-resolution TEM image revealing the nanogranular morphology of $TiN_{1.0}$ deposited at (a)500, (b)200 and (c)25^{o}C.

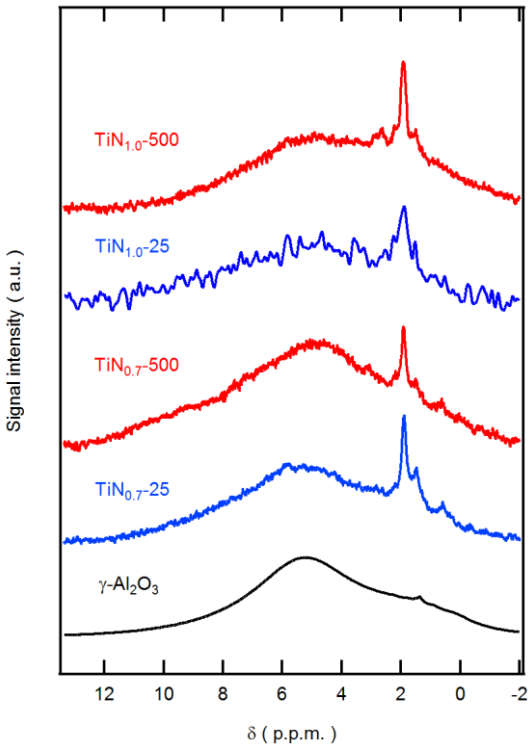


Fig. 4-4 ^{1}H-NMR spectra of TiN_x-500 (red lines) and -25 films (blue lines) (x = 0.7, 1.0; 1 μm thickness) detached from the Si substrate with 100-nm-thick γ-Al_2O_3 sacrificial coating. All samples are treated in 50 vol% H_2/Ar at 500°C for 1 h. The spectrum of the sacrificial γ-Al_2O_3 layer (1 μm thickness) is also shown as a reference.

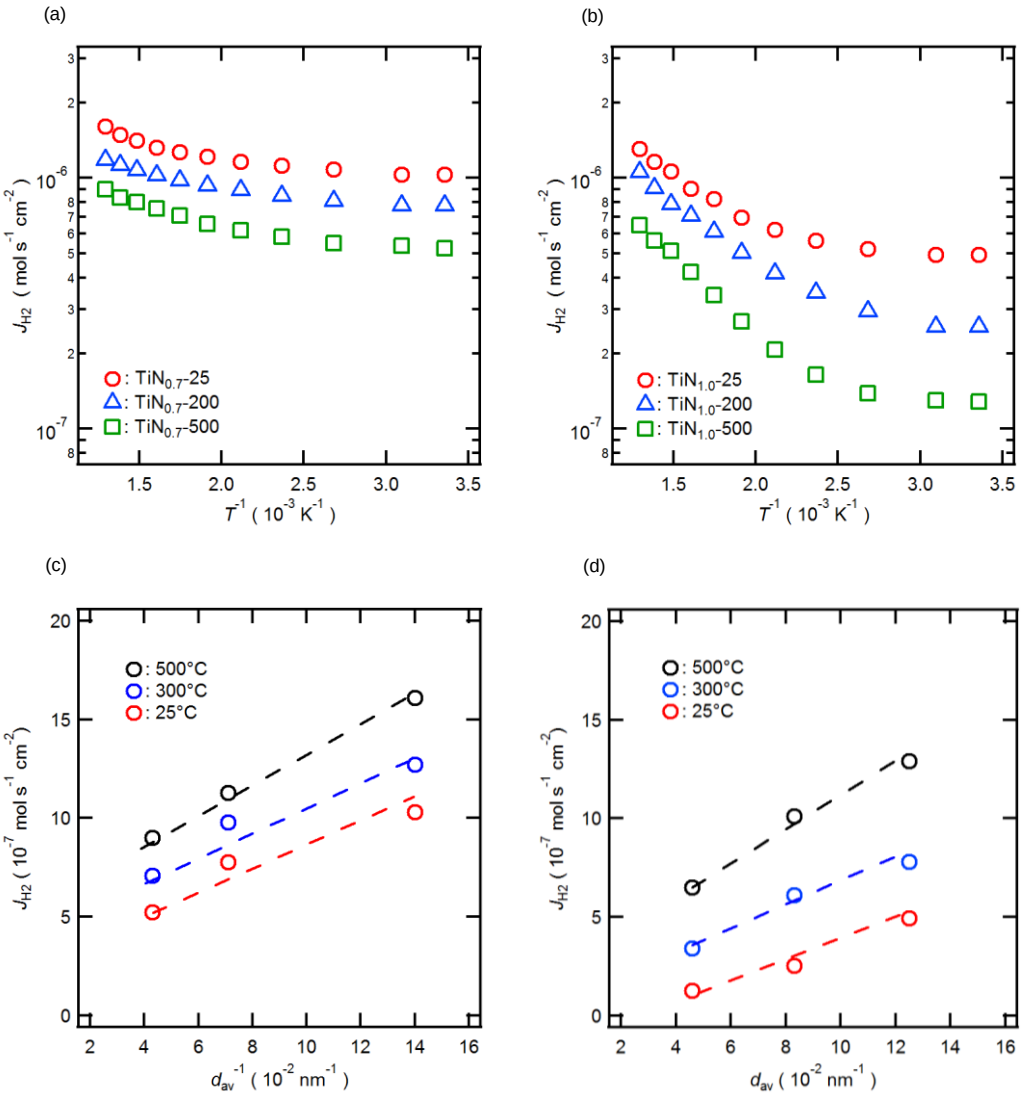


Fig. 4-5 Hydrogen flux of TiN_x membranes at temperatures between ambient and 500°C. (a-b) Arrhenius plots of hydrogen fluxes (J_{H2}) through (a) $TiN_{0.7}$ and (b) $TiN_{1.0}$ membranes of 600-nm thickness prepared at 25°C, 200°C and 500°C. (c-d) The relationship between hydrogen permeation fluxes (J_H) and reciprocal average grain sizes (d_{av}^{-1}) of TiN_x membranes.

4-3-3 Grain size dependence of hydrogen solubility

To provide further verification of interfacial hydrogen solubility in the TiN_x membranes, room-temperature hydrogen sorption was measured for TiN_x-25 and -200 using a 5 MHz quartz crystal microbalance (QCM) by directly depositing $TiN_{0.7}$ or $TiN_{1.0}$ films on a Au electrode of a quartz resonator at 25 or 200°C (Fig. 4-6).[16,17] Unfortunately, it was difficult to fabricate TiN_x-500 on a resonator due to the thermal damage. Upon exposure of $TiN_{0.7}$-25 and -200 in 50%-H_2, the QCM frequencies dropped abruptly and stabilized at –40.9 and –30.1 Hz, respectively, which corresponded to 1.92 and 1.41 μg of hydrogen sorption at 25°C, respectively (Fig. 4-6(a)). Using the geometric film volumes and ideal molar density (8.44×10^{-2} mol cm^{-3}),[18] the hydrogen solubility (S_H), which is defined by the H/Ti ratio under equilibrium, of $TiN_{0.7}$-25 and -200 were calculated to be 0.22 and 0.15, respectively. Similarly, the S_H values of $TiN_{1.0}$-25 and -200 were calculated as 0.14 and 0.11, respectively. The S_H values thus determined are summarized in Table 4-2.

The linearly proportional S_H vs. d_{av}^{-1} curve proved that the hydrogen was favorably incorporated into the grain boundary regions (Fig. 4-7(a)). The S_H of $TiN_{0.7}$-25 was 1.5 times higher than that of $TiN_{0.7}$-200, which is in good agreement with the d_{av}^{-1} ratio of $TiN_{0.7}$-25 to $TiN_{0.7}$-200 (~1.8). Similarly, the S_H of $TiN_{1.0}$-25 (0.14) was larger than that of $TiN_{1.0}$-200 (0.11) by a factor of 1.3, where this value was also in agreement with the d_{av}^{-1} (8 nm/12 nm~1.5) ratio (~1.59) between $TiN_{1.0}$-25 and $TiN_{1.0}$-200 (Table 4-2). Considering also the flux behaviour, the size-enhanced hydrogen permeability was related to the increase in interfacial hydridic carriers.

Moreover, the QCM-measured hydrogen solubility, S_H was in close agreement with the hydrogen content required for a monolayer coverage of all crystallites with terminal Ti–

H bonds. Assuming that the hydrogenation of each crystallite occurred by obeying the Langmuir monolayer chemisorption[19] of hydrogen onto surface Ti sites and that monolayer coverage was achieved under equilibrium conditions at $p_{H2} = 0.5\ p_0$, S_H should ideally be equal to the fraction of the surface to bulk Ti (F_{Ti}) for TiN nanocrystallites. Here, the brick layer model with nanocubes with a side length of d_{av} and grain boundary width of ζ was considered to calculate an ideal F_{Ti} (Fig. 4-8(a)). Because (100)-oriented NaCl-type nanocubes have six equivalent square faces and every face includes two Ti cations (Fig. 4-8(b)), F_{Ti} of the (100)-oriented brick layers (F_{Ti} (100)) were calculated as follows:

$$F_{\mathrm{Ti}}(100) = \frac{(2 \times 6\ {d_{av}}^2 l^{-2})}{(4\ {d_{av}}^3\ l^{-3})} = 3\ l\ {d_{\mathrm{av}}}^{-1} \tag{4-3}$$

where, l is the lattice constant.

The morphology of a (111)-orientated nanocube is more complicated: it has a pair of (111) surfaces on the top with two orthogonal faces with (110) surfaces and the other two with (112) surfaces (Fig. 4-8(c-e)). The (111) surface exposes alternatively pure Ti or N closed-packed-layers (Fig. 4-8(c)); therefore, pure Ti (111) faces retain ideally 2.5 Ti cations per area defined by $\sqrt{3}l^2/2$. The probability of a pure Ti layer is equal to 1/2 and F_{Ti} for one (111) face of a NaCl-type nanocube (f_{Ti} (111)) is calculated using:

$$f_{\mathrm{Ti}}\ (111) = \frac{2.5}{\sqrt{3}} {d_{\mathrm{av}}}^2 l^{-2} \tag{4-4}$$

As shown in Fig. 4-8(d), the (110) surface ideally includes two Ti cations per area defined by $\sqrt{2}l^2$; therefore, F_{Ti} for one (110) face of a nanocube (f_{Ti} (110)) is represented as:

$$f_{\mathrm{Ti}}\ (110) = \frac{2}{\sqrt{2}} {d_{\mathrm{av}}}^2 l^{-2} \tag{4-5}$$

Similarly, F_{Ti} for one (112) face of a nanocube (f_{Ti} (112)) (Fig. 4-8(e)) is given by:

$$f_{\mathrm{Ti}}\,(112) = \frac{253}{15\sqrt{6}} d_{\mathrm{av}}{}^{2} l^{-2} \tag{4-6}$$

Finally, the corresponding F_{Ti} for (111)-oriented nanocubes is calculated from the sum $2 \times f_{\mathrm{Ti}}\,(111) + 2 \times f_{\mathrm{Ti}}\,(110) + 2 \times f_{\mathrm{Ti}}\,(112)$, as follows:

$$\begin{aligned} F_{\mathrm{Ti}}(111) &= \left\{\left(\frac{2.5\times2}{\sqrt{3}} + \frac{2\times2}{\sqrt{2}} + \frac{253\times2}{15\sqrt{6}}\right) d_{\mathrm{av}}{}^{2} l^{-2}\right\} / 4 d_{\mathrm{av}}{}^{3} l^{-3} \\ &= 4.87\; l d_{\mathrm{av}}{}^{-1} \end{aligned} \tag{4-7}$$

The ideal S_{H} is equivalent to F_{Ti} when a monolayer coverage with terminal Ti-H is achieved.

Fig. 4-7(b) shows plots of the observed S_{H} as a function of F_{Ti} calculated from Eq. (4-3) or (4-7) with the observed d_{av}, along with a straight line indicating the relationship $S_{\mathrm{H}} = F_{\mathrm{Ti}}$. In both (111)-oriented $TiN_{0.7}$ and (100)-oriented $TiN_{1.0}$, the S_{H} values were very close to the straight line, confirming that the hydrogen solubility of TiN_x was identical to the amount required to form the monolayer on all crystallite surfaces in the membrane matrices. The S_{H} values of (100)-oriented $TiN_{1.0}$-200 and $TiN_{1.0}$-25 (0.11 and 0.14, respectively) were in agreement with the corresponding F_{Ti} values (0.11 and 0.16, respectively), and similarly, S_{H} of (111)-oriented $TiN_{0.7}$-200 and $TiN_{0.7}$-25 (0.15 and 0.22, respectively) were also very close to the corresponding F_{Ti} values (0.19 and 0.24, respectively). These features unambiguously demonstrate that hydridic defects were predominantly formed along grain boundaries as Ti-H terminal groups on individual crystallites, while they were not observed in the grain bulk. This is consistent with the theoretical calculations reported in Chapter. 3. If the hydrogen defects exist in the grain interior, they must occupy the interstitial sites of the NaCl-type structure as stoichiometric $TiN_{1.0}$ can retain an amount of hydrogen defects, as shown by the QCM results (Fig. 4-6). However, DFT calculations clarified that the interstitial hydrogen defects are not

energetically favoured.

The S_H of $TiN_{0.7}$-200 (d_{av} of 13 nm) was 1.4 times larger than that of $TiN_{1.0}$-200 (d_{av} of 12 nm), which was in agreement with the theoretical ratio given by comparing Eq. (4-3) and (4-7), revealing that the hydridic carrier concentration of (111)-oriented films became 1.6 times larger than that of the (100)-oriented films with the same d_{av}. The E_a of (111)-oriented $TiN_{0.7}$ (ca. 5.8 kJ mol^{-1}) was about half that of (100)-oriented $TiN_{1.0}$ (ca. 12 kJ mol^{-1}), indicating that the relatively high concentration of surface Ti coordination sites on (111)-related faces were advantageous for interfacial diffusion. The (100) surface has alternating arrays of Ti and N atoms, while the (111) surface shows a closed-packed-layer of only Ti, and the (112) face has a consecutive linear chain of Ti cations (Fig. 4-8(b) and (d)). Therefore, diffusion along (111)-oriented crystallites would be much easier than along (100) ones due to abundant Ti coordination sites. In addition, the absence of N anions between adjacent Ti should create a shallow bottleneck potential for hydride anion transfer. This analysis offers a clear guideline for developing high-throughput hydrogen separation membranes, suggesting that simultaneous control of the sizes and grain growth of crystallites can drastically improve the hydrogen permeability of TiN_x nanocrystalline membranes at ambient temperature.

4-4 Conclusion

It is clearly demonstrated that hydrogen permeability of TiN_x nanocrystalline membranes is driven by the diffusion of hydridic defects in the interfacial grain boundary regions. The nanocrystalline TiN_x matrix was readily hydrogenated when exposed to hydrogen, and Ti-H terminal groups were formed over the surfaces of individual crystallites, resulting in the incorporation of hydridic defects into the grain boundary regions. Therefore, the TiN_x membranes showed pronounced grain boundary diffusion of hydrogen aided by thermal hopping of hydride ions between neighboring Ti atoms. Therefore, the hydrogen solubility was drastically improved by reducing crystallite size as the number of the coordination Ti sites is linearly proportional to the reciprocal of crystallite size. In addition, the orientation of the crystallites is important to improve the hydrogen permeability. Since the (111) face of NaCl-type TiN_x has a higher Ti concentration than the (100) face, (111)-oriented nanocrystalline films exhibit smaller diffusion energy and higher solubility than (100)-oriented ones due to the relatively short Ti-Ti jump distances. Accordingly, 200 nm (111)-oriented $TiN_{0.7}$ membranes with sub-10 nm crystallites yield permeation fluxes of 4×10^{-6} mol s^{-1} cm^{-1} under an applied hydrogen partial pressure of about 50 kPa at ambient temperature. This value was only one order of magnitude smaller than the fluxes of state-of-the-art $Pd_{0.75}Ag_{0.25}$ membranes at 450°C. Hence, we verified that nanocrystalline TiN_x membranes are feasible for high-throughput separation of ultrapure hydrogen at ambient temperature.

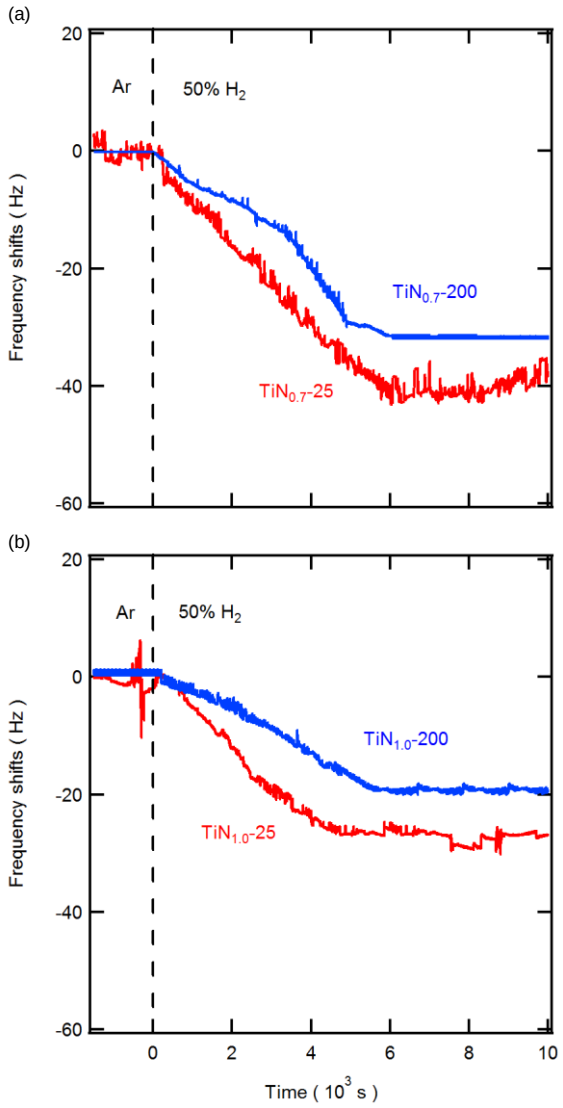


Fig. 4-6 Response transient of QCM frequency shifts due to hydrogen adsorption on (a) $TiN_{0.7}$ (1.05 μm) and (b)$TiN_{1.0}$ films (1.0 μm) deposited at 25 or 200°C on a gold film oscillator electrode (1.32 cm^2). Measurements were performed by switching from pure Ar to 50 vol% H_2/Ar at 25°C.

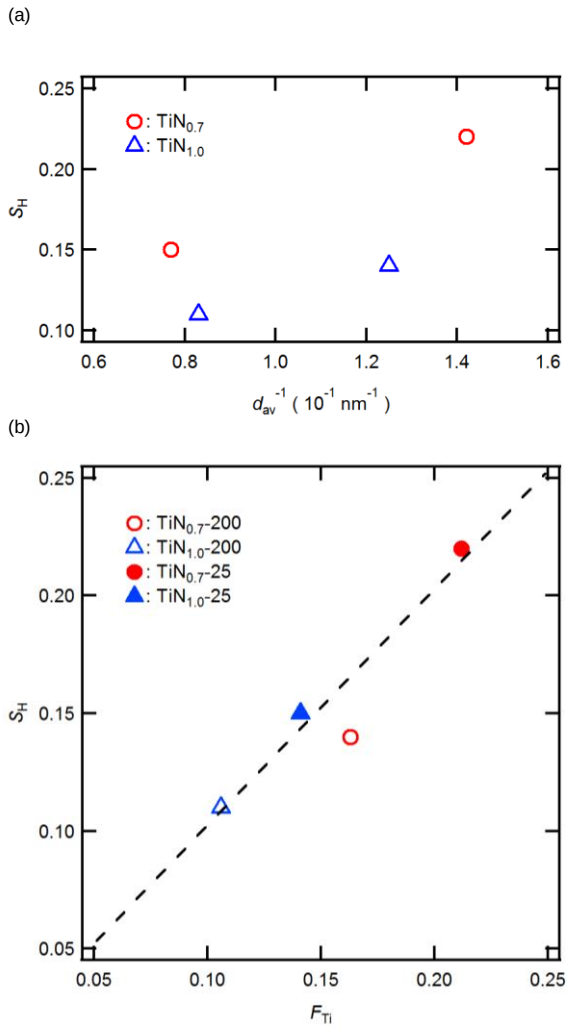


Fig. 4-7 (a) Relationship between hydrogen solubility (S_H) and the reciprocal of average crystallite size (d_{av}^{-1}). (b) Relationship between S_H and fractions of surface Ti cations (F_{Ti}) in TiN_x. F_{Ti} is calculated by Eq. (4-3) and (4-7). The theoretical S_H is also shown as a dashed line, which is defined as being equivalent to the F_{Ti}. The details are described in text.

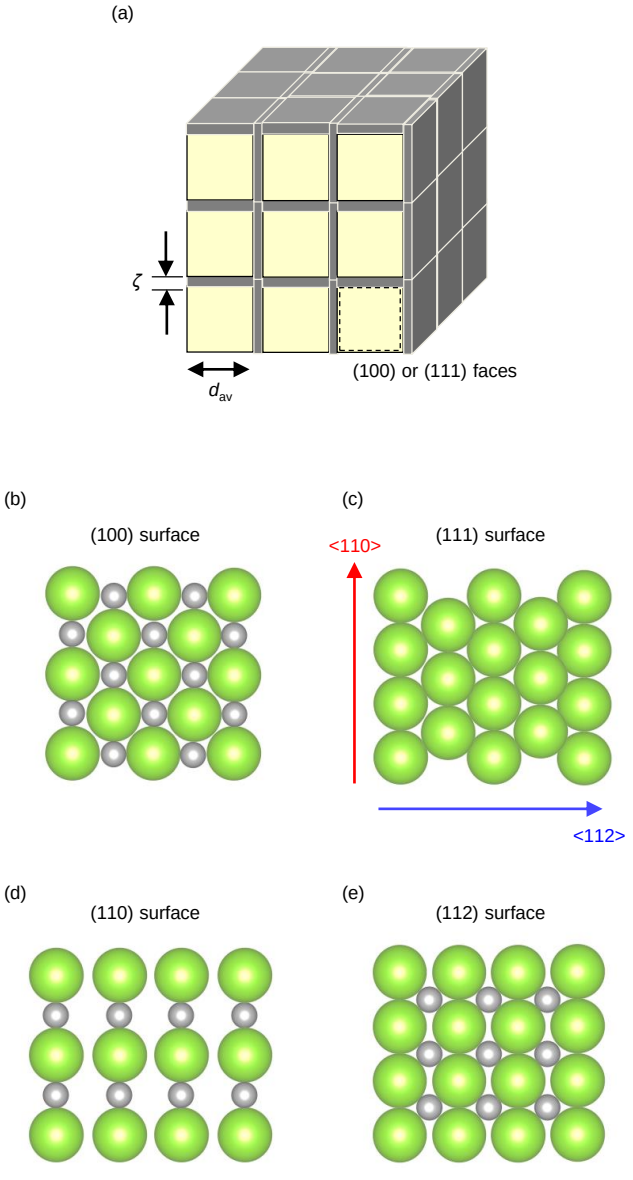


Fig. 4-8 (a) Schematic image of brick layer model for interfacial hydridic conduction in nanocrystalline TiN_x membranes with yellow cube representing grain cores and gray shell grain boundary phase. (b-e) Atomic arrangement of (b) (100), (c) (111), (d) (110) and (e) (112) crystallographic planes of NaCl type TiN. (100)-oriented cubic-shape crystallites have six equivalent planes. (111)-oriented crystallites expose a pair of (111) faces on the top with two orthogonal faces disclosing (110) faces and the other two (112).

4-5 References

1 Drioli, E.; Barbieri, G. *Membrane Engineering for the Treatment of Gases: Volume 2: Gas-separation Problems Combined with Membrane Reactors (1st Edition)*; RSC Publishing: United Kingdom, 2011.

2 Kim, S.; Avila-Paredes, H. J.; Wang, S.; Chen. C. T.; De Souza, R. A.; Martin, M.; Munir, Z. A. *Phys. Chem. Chem. Phys.* **2009**, 11, 3035-3038.

3 Schlom, D. G.; Chen, Long-Qing.; Pan, X.; Schmehl, A.; Zurbuchen. M. A. *J. Am. Ceram. Soc.* **2008**, 91, 2429-2454.

4 de Vos, R. M.; Verweij, H. High-selectivity, High-flux silica membranes for gas separation. *Science*. **1998**, 279, 1710–1711.

5 Uhlhorn, R. J. R.; Zaspalis, V. T.; Keizer, K.; Burggraaf, A. J. Synthesis of ceramic membranes. *J. Mater. Sci*. **1992**, 27, 527–552.

6 Roesky, H. W.; Bai, Y. Noltemeyer, M. *Angew. Chem. Int. Ed.* **1989**, 28, 754-755.

7 Abarca, A.; Gómez-Sal, P.; Martín, Avelino.; Mena, M.; Poblet, J. M.; Yélamos, C. *Inorg. Chem.* **2000**, 39, 642-651.

8 Hayashi, K.; Sushko, P. V.; Hashimoto, Y.; Shluger A. L.; Hosono, H. *Nat. Commun.* **2014**, 4514, 1-8.

9 Nicol A. T.; Vaughan, R. W. *J. Chem. Phys.* **1978**, 69, 5211.

10 Magusin, P. C. M. M.; Kalisvaart, W. P.; Notten P. H. L.; van Santen, R. A. *Chem. Phys. Lett.* **2008**, 456, 55-58.

11 Bowman, R. C.; Hwang, S. J.; Ahn C. C.; Vajo, J. J. *MRS Proc*, **2004**, 837, N3.6.

12 Siodmiak, M.; Govind, N.; Andzelm, J.; Tanpipat, N.; Frenking, G.; Korkin, A. *Phys.*

Stat. Sol. *B*. **2001**, 226, 29-36.

13 Bonanos, N.; Huijser, A.; Poulsen, F. W. *Solid State Ionics*. **2015**, 275, 9-13.

14 Schlom, D. G.; Chen, L.; Pan, X.; Schmehl A.; Zurbuchen, M. A. *J. Am. Ceram. Soc.*, **2008**, 91, 2429-2454.

15 Itoh, N.; Wu, T. H.; Haraya, K. *J. Membr. Sci*. **1999**, 99, 175-183.

16 Aoki, Y.; Hashizume, M.; Onoue, S.; Kunitake, T. *J. Phys Chem. B*. **2008**, 112, 14578-14582.

17 Uekawa, N.; Kaneko, K. *J. Phys. Chem. B.* **1998**, 102, 8719-8724.

18 Pierson, H. O. *Handbook of Chemical Vapor Deposition: Principle, Technology and Applications (Second Edition)*; Noyes publications: New Jersey, 1999.

19 Conway, B. E. *Electrochim. Acta.* **1993**, 38, 1249-1258.

Chapter 5

Hydrogen permeability of hafnium nitride nanocrystalline membranes by interfacial hydridic conduction

5-1 Introduction

Hydrogen-related defects have been known to occur frequently in different metal nitrides as well as in metal oxides.[1-6] Van de Walle et al. reported that hydrogen tends to act as a shallow donor (H^+) or acceptor (H^-) in metal nitride semiconductors if the Fermi energy level is low or high enough relative to the ε(+/–) energy threshold (–4.4 eV vs V. L.),[6] respectively. According to this criterion, hydrogen favors to form hydridic defects in TiN, if the doping is possible, because TiN has relatively high Fermi energy levels (–4.1 eV vs V. L.).[7] As mentioned in previous chapters, it has been demonstrated that titanium nitride (TiN_x; x = 0.7, 0.9, and 1.0) nanocrystalline membranes exhibit hydrogen permeability levels exceeding that of Pd metals at room temperature due to the fast diffusion of hydridic ions.[8] This observation is ascribed to the following reasons. 1) Nanocrystalline TiN_x matrices are readily hydrogenated at ambient hydrogen pressure and form Ti-H terminal groups over individual crystallite surfaces, and thus 2) hydridic diffusion takes place along the interfacial grain boundary via bond exchange between Ti-H terminal groups.[8] These findings imply that metal nitride systems with relatively high

Fermi energy levels and significantly reduced crystallite sizes can exhibit excellent hydrogen permeability owing to fast hydridic conduction at significantly lowered activation energies. Hafnium nitrides (HfN_x) have the same NaCl-type crystal structure as TiN_x, while the Fermi energy level (about –4.3 eV vs. V.L.)[7,9] is higher than the threshold. Hence, it would be interesting to examine the hydrogen permeability of well-defined nanocrystalline films of HfN_x.

In Chapter 5, HfN_x nanocrystalline membranes is demonstrated to exhibit a pronounced hydrogen permeability, comparable to that of TiN_x, at ambient temperatures owing to a rapid interfacial diffusion of hydridic ions. Both $HfN_{0.8}$ and $HfN_{1.0}$ films with equivalent crystallite sizes and (100)-grain growth orientation exhibit similar hydrogen solubility and permeability regardless of the large differences in nitrogen deficiency, which confirms that hydrogen transport is driven via hydride hopping between terminal Hf-H groups over hydrogenated crystallite surfaces without mediation by bulk nitrogen vacancies.

5-2 Experimental

5-2-1 Hydrogen permeability tests

(a) RF sputtering deposition of HfN_x membranes

HfN_x membranes (x = 0.8 and 1.0) were deposited by reactive sputtering in an ultrahigh vacuum chamber system (ULVAC ACS-3000) using a Hf metal disk (99.99% purity) with 2 inch-diameter as a target. The base pressure of the chamber was less than 2×10^{-5} Pa.

HfN_x films were deposited in a flow of an Ar/N_2 mixed gas at a total pressure of 0.9 Pa. The substrate temperatures were kept at 25, 200 or 500°C, and a sputtering power was applied at 200 W. The Ar/N_2 molar ratio in the mixed gas was controlled using a mass flow controller by fixing the total gas flow at 20 sccm. The thickness of the membranes was adjusted in the range of 200–1000 nm by controlling the sputtering time. TiN_x membranes (x = 0.7 and 1.0) were fabricated by the same RF sputtering method as reported in our earlier work (Chapter 3).[8] In summary, the films were deposited in an Ar/N_2 atmosphere at a total pressure of 0.9 Pa, substrate temperature of 200 °C, and a sputtering power of 200 W. The Ar/N_2 gas flow ratios were 96/4 for $TiN_{0.7}$ and 0/100 for $TiN_{1.0}$ and the total gas flow was controlled at 20 sccm.

(b) Hydrogen permeation tests of HfN_x membranes

For hydrogen permeability analysis, HfN_x membranes were fabricated on porous alumina supports consisting of macroporous α-Al_2O_3 sintered pellets with a mesoporous γ-Al_2O_3 top layer. The porous alumina supports were prepared according to a method previously reported by Uhlhorn et al.[10,11] The detail of the procedure is written in 3-2-1(a).

Hydrogen permeability measurements of HfN_x membranes were performed in a homemade gas-tight chamber system equipped with a gas chromatograph (GC, GL Sciences GC-4000). A HfN_x membrane sample was sealed in a specially designed sample holder using carbon sheet gaskets and placed in an electrical furnace whose temperature could be controlled. Pure Ar gas was supplied to the porous support side at 25 sccm and a 1:1 gas mixture of H_2/N_2 was supplied to the membrane side at 100 sccm using mass

flow controllers. H_2 and He in out gas were detected by thermal-coductive detector (TCD) with a flow of Ar reference gas and N_2 by TCD with a flow of N_2 reference gas. The hydrogen fluxes, J_{H2}, are determined from the hydrogen concentrations, analyzed using GC, in the exhaust on the support side as follows,

$$J_{\mathrm{H2}} = \frac{C_{\mathrm{H}} J_{\mathrm{Ar}}}{C_{\mathrm{Ar}}} \tag{5-1}$$

where C_H and C_{Ar} are the concentrations of H_2 and Ar in the out gases, respectively, and J_{Ar} is the Ar flow (25 sccm) supplied to the alumina support side. The fluxes of others were also determined by the same way.

5-2-2 Characterization techniques

(a) Materials characterization

The phase purities of the fabricated membranes were checked by X-ray diffraction (XRD; RIGAKU RINT2200 diffractometer with Cu Kα radiation) in the 2θ scan mode with a fixed θ axis at 1° at 40 kV and 20 mA. For XRD measurements, a Si wafer spin-coated with a mesoporous γ-Al_2O_3 layer (100 nm thick) was used as the substrate instead of the γ-Al_2O_3/α-Al_2O_3 bilayer porous supports used for permeation tests because most of the XRD patterns of HfN_x overlapped with those of α-Al_2O_3, whereas the influence of the crystallographic orientation of a Si wafer could be isolated and precluded. Spin coating of γ-Al_2O_3 on Si wafers was conducted in a manner similar to the method described earlier with 0.1 M boehmite sol. Rutherford backscattering spectrometry (RBS) was carried out on 500 nm-thick films using a 2.0-MeV He^+ beam (Tohoku University), and the curve fitting analysis was carried out with RUMP software package.[12] To reduce

the increase in background signal intensity, which occurs when heavy elements are used as substrates, the films used for RBS measurements were deposited on glassy carbon plates. The morphologies of the HfN_x membranes were characterized by transmission electron microscopy (TEM; JEOL JFM-ARM-200F), for which the specimens were prepared by focused ion beam microfabrication (FIB; HITACHI FB-2100) or microtome (PowerTome, RMC products). Field emission scanning electron microscopy (FE-SEM) imaging was carried out using a JEOL JSM-6500F instrument. Fourier transform infrared (FT-IR) spectroscopy was carried out on 500 nm-thick HfN_x films on porous alumina supports using a JASCO FT/IR-350 spectrometer.

^1H magic angle spinning (MAS) nuclear magnetic resonance (NMR) spectra of the developed membranes were recorded on a JNM-ECA600 (JEOL RESONANCE Inc.) spectrometer operating at a resonance frequency of 598.97 MHz; the spectrometer was equipped with a magic angle spinning probe with a diameter of 3.2 mm. The MAS frequency was kept at 10 kHz. For each sample, spectra were acquired with two types of pulse sequences – a single pulse with 30 deg pulse and a length of 1.5 μs and a DEPTH background suppression pulse sequence with 90 deg pulse. The measured frequency range was 10 kHz. The repetition time was 5 s for single pulse experiments, while it was 8 s for DEPTH experiments. A total of 318 scans were performed for single pulse experiments and 256 scans were performed for DEPTH experiments. The chemical shifts were externally referenced to tetramethylsilane (TMS). For NMR measurements, 5 μm-thick HfN_x films were deposited on Si wafers modified with 100 nm-thick γ-Al_2O_3 buffer sacrificial layers; HfN_x powders were obtained by scratching the deposited layers with a spatula to pulverize. The powder specimens thus obtained were filled in a sample tube in

a H_2 atmosphere.

The hydrogen solubility is evaluated with a 5 MHz quartz crystal microbalance (QCM) technique. The quartz crystal resonator (∅1.0 cm) attached with an Au film electrode (1.32 cm^2) are purchased from MaTek. HfN_x films are deposited directly on the Au film electrode using a shadow mask at 25°C and 200°C. The amount of hydrogen solves in the membranes was determined by the shift of the resonance frequency when pure Ar supply is abruptly switched to 50%-H_2/Ar gas at 25°C.

(b) Density-functional theory (DFT) calculations

The electronic states of the hydrogen impurities in HfN_x were characterized by first-principle calculations. The calculations were based on the spin-polarized density-functional theory (DFT) with a generalized gradient approximation (GGA) using the PBE exchange-correlation function,[13] which is implemented using the plane-wave and projector augmented wave methods of the Vienna Ab-initio Simulation Package (VASP).[14-19]The supercells consists of 2 × 2 × 2 HfN unit cells (~64 atoms) with neutrally charged defects. The cut-off energy for the plane-wave basis was set to 600 eV. A Γ-centered 3 × 3 × 3 Monkhorst-Pack special k-point grid[20] for the first Brillouin zone using a Gaussian smearing model of σ = 0.05 eV was used. ΔE_{def} for H defects in $HfN_{1-\delta}$ supercells can be expressed according to

$$\Delta E_{def} = E^{tot}[\mathrm{HfN_{1-\delta}H}] - E^{tot}[\mathrm{HfN_{1-\delta}}] - 1/2\mu_{H2} \qquad (5\text{-}2)$$

where E^{tot}[supercell] represents the total energy of each supercell. The chemical potential of H, denoted by μ_{H}, is derived from the enthalpy of hydrogen.[21] ΔE_{def} is calculated for the HfN phase with one H interstitial, H_i: $HfN(H_i)_{1/32}$ ($Hf_{32}N_{32}H_i$) and $HfN_{0.75}$ with one H

on the N vacancy, H_N: $HfN_{0.75}(H_N)_{1/32}$ ($Hf_{32}N_{24}H$).

In the case of $HfN(H_i)_{1/32}$, three types of H interstices are considered: i) $^{tet}H_i$: the tetrahedral site of the fcc Hf sublattice, ii) $^{Hf\text{-}N}H_i$: the center of the closest Hf-N bond, and iii) $^{Hf\text{-}Hf}H_i$: the center of the closest Hf-Hf bond (Fig. 5-15). ΔE_{def} for all interstitial defect models, however, exhibits large positive values (>2 eV) even after lattice relaxation and hence the formation of H interstitials is not favorable for HfN_x. On the other hand, ΔE_{def} for hydrogen defects on N vacancy sites, H_N, is converged to a negative value (–0.71 eV).

5-3 Results and Discussion

5-3-1 Fabrication of HfN_x membranes

First of all, we conducted an extensive study on reactive sputtering deposition with a pure Hf metal target by changing the Ar/N_2 gas flow ratios and substrate temperatures in order to fabricate HfN_x films by adjusting nitrogen nonstoichiometry, x, and grain sizes. Other deposition parameters, such as sputtering power and chamber pressure were fixed as mentioned in 5-2-1(a). The crystallinity and phase purity of the deposited films were analyzed by XRD to optimize the process conditions. For XRD analysis, a Si wafer spin-coated with a mesoporous γ-Al_2O_3 layer (100 nm thick) was used instead of an γ-Al_2O_3/α-Al_2O_3 bilayer porous support because most of the XRD peaks of HfN overlap with those of α-Al_2O_3 whereas the influence of the crystallographic orientation of a Si wafer could be isolated and precluded. Finally, nearly-stoichiometric HfN_x films with $x = 1.0 \pm 0.06$ and N-deficient films with $x = 0.8 \pm 0.04$ were prepared as a single phase of the NaCl

type (cubic; *Fm3m*), as confirmed by XRD, wavelength-dispersive X-ray spectroscopy (WDX) and Rutherford back scattering (RBS) analyses. Both types of films contained small amounts of oxygen impurities (O/Hf < 0.04) (Fig. 5-1, 5-2, 5-3 and Table. 5-1). These films were denoted as $HfN_{1.0}$ and $HfN_{0.8}$, respectively, for brevity and were further investigated. The details of the process gases and substrate temperatures used for deposition are summarized in Table 5-2.

All HfN_x (x = 0.8 and 1.0) films exhibit a preferred (100) orientation grain growth and the full width at half maximum (FWHM) values of the (100) XRD peaks increased with a decrease in the deposition temperature; this observation is attributed to the smaller crystallite sizes at lower temperatures. By XRD analysis using the Scherrer equation, the average grain sizes (d_{av}) of the films deposited at 500, 200, and 25°C were calculated to be 25, 14, and 11 nm, respectively, in the case of $HfN_{0.8}$ and 24, 13, and 10 nm, respectively, in the case of $HfN_{1.0}$ (Table 5-1). Hereafter, the films deposited at various temperatures are denoted as HfN_x-25, 200, or 500 (x = 0.8 or 1.0). Previously, we confirmed that $TiN_{0.7}$-200 exhibited a (111) orientation, while $TiN_{1.0}$-200 exhibited a (100) orientation, similar to the HfN_x films.[8] The patterns corresponding to these films are displayed in Fig. 5-1.

Hydrogen-permeable membranes were fabricated by depositing HfN_x layers on porous alumina supports modified by a 1.2 μm-thick mesoporous γ-Al_2O_3 top layer.[10,11] Densely-packed HfN_x layers are uniformly formed over γ-Al_2O_3 middle layers (Figs. 5-4(a-b)) with forming sharp HfN_x/Al_2O_3 interfaces (Fig. 5-4(c)). All membranes have columnar microstructures irrespective to the different deposition temperatures. Moreover, the membranes retain nanocrystalline morphologies, with each column comprising of

rectangular nanograins with an average size (d_{av}) of a few tens of nanometers (Figs. 5-4(d-e)). The d_{av} values measured by TEM are listed in Table 5-2; these results are in agreement with the corresponding sizes determined by XRD analysis.

Table 5-1 Phase purity and chemical composition of HfN_x films on a Si wafer.

N_2 concentration / %	Phase	Composition by WDX	Composition by RBS
3	HfN, Hf	$HfN_{0.34}O_{0.077}$	-
4	HfN, Hf	$HfN_{0.54}O_{0.76}$	-
10	HfN	$HfN_{0.83}O_{0.085}$ ($HfN_{0.8}$)	$HfN_{1.04}O_{0.035}$ (10 nm, outer)/ $HfN_{0.79}O_{0.031}$ (580 nm, inner)
40	HfN	$HfN_{1.04}O_{0.080}$ ($HfN_{1.0}$)	$HfN_{1.13}O_{0.035}$ (10 nm, outer)/ $HfN_{1.06}O_{0.033}$ (590 nm, inner)

Table 5-2 RF reactive sputtering conditions of HfN_x (x = 0.8 and 1.0) nanocrystalline membranes and the average grain sizes (d_{av}) of the corresponding membranes deposited on γ-Al_2O_3/Si wafers, as determined by XRD and TEM.

samples	Substrate temperature / °C	N_2 concentration / %	d_{av} (XRD) / nm	d_{av} (TEM) / nm
$HfN_{0.8}$-500	500	10	25	23
$HfN_{0.8}$-200	200	15	14	–
$HfN_{0.8}$-25	25	20	11	11
$HfN_{1.0}$-500	500	40	24	–
$HfN_{1.0}$-200	200	40	13	–
$HfN_{1.0}$-25	25	40	10	–

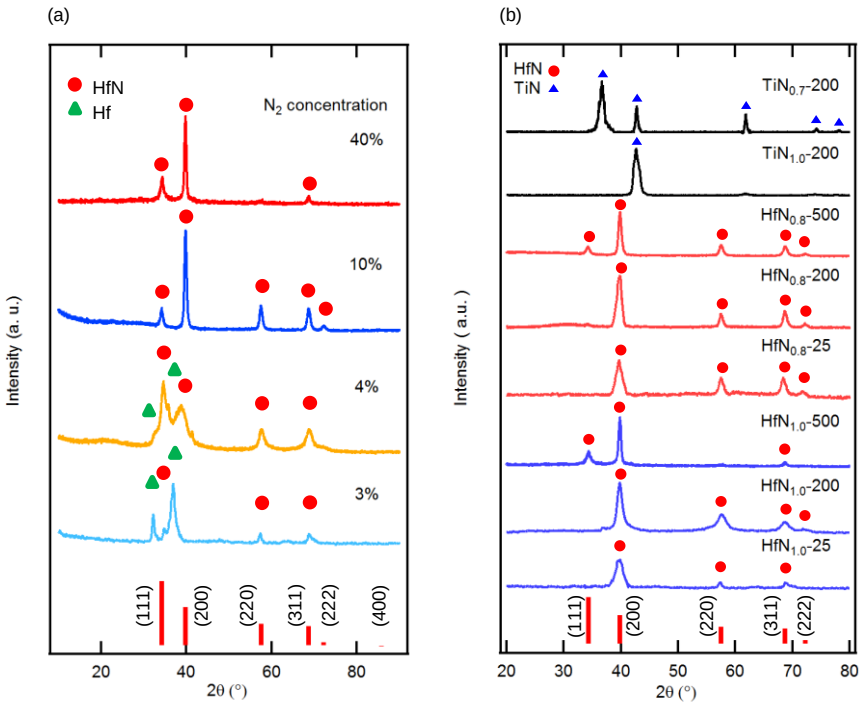


Fig. 5-1 XRD patterns of HfN_x films. (a) HfN_x films deposited on a Si wafer (100) by RF sputtering in reactive gases with various N_2 concentrations. Chamber pressure and substrate temperature were fixed at 0.9 Pa and 500°C, respectively. (b) XRD patterns of 500 nm-thick HfN_x (x = 0.8 and 1.0) films deposited at 25, 200, and 500°C. TiN_x films (600 nm thick, x = 0.7 and 1.0) films deposited at 200°C[8] are also shown.

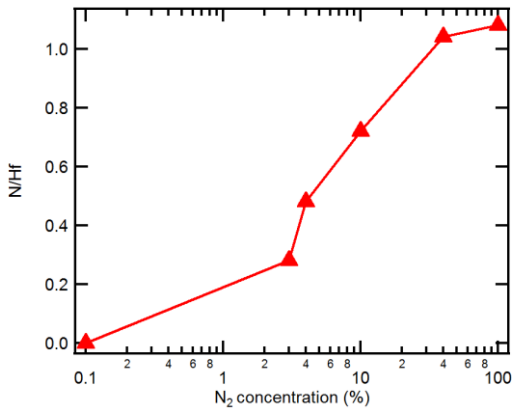


Fig. 5-2 Nitrogen stoichiometry of sputter-deposited HfN_x thin films as a function of N_2 concentrations in reactive sputtering gases. *x* is determined by WDX.

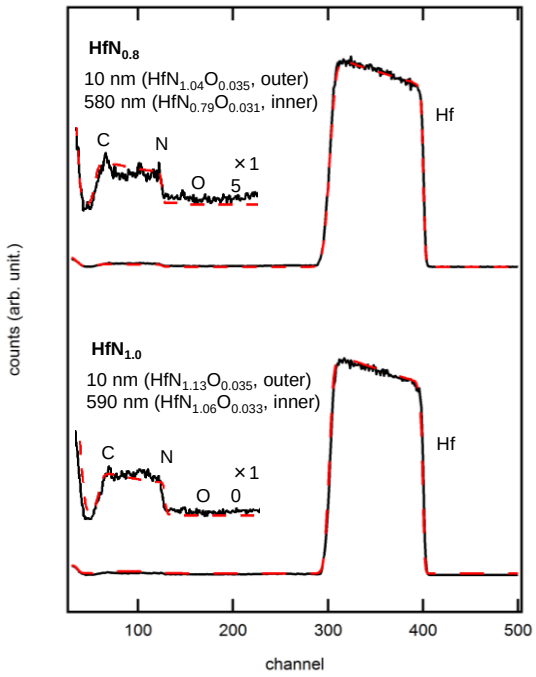


Fig. 5-3 RBS depth profiles of $HfN_{0.8}$ and $HfN_{1.0}$ films (500 nm) prepared on glassy carbon substrates. Black lines are the observed and red dots the simulated. Their corresponding chemical composition is $HfN_{0.79}O_{0.031}$ ($HfN_{0.8}$) and $HfN_{1.06}O_{0.033}$ ($HfN_{1.0}$), respectively. The surfaces of both films are oxidized by air, forming 10 nm-thick outerlayer.

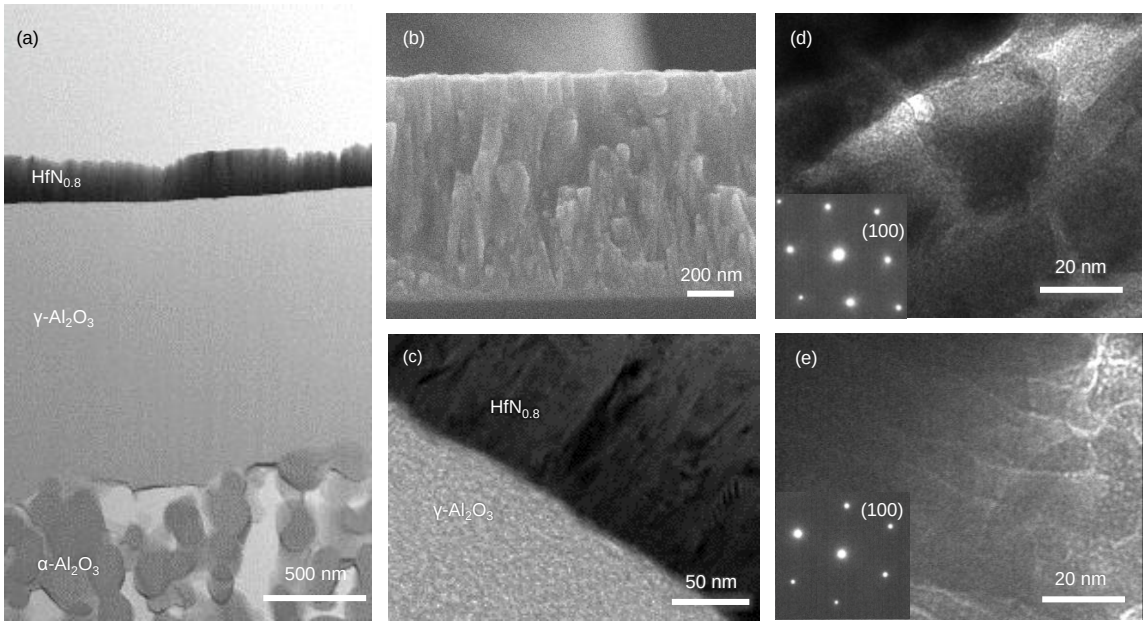


Fig. 5-4 Electron microscopy images showing nanocrystalline and dense HfN_x membranes formed over porous alumina supports. (a) Cross-sectional TEM image of a membrane device comprising of sputter-deposited $HfN_{0.8}$ (top layer, 250 nm), sol-gel-derived mesoporous γ-Al_2O_3 (middle layer, 1.2 µm), and macroporous α-Al_2O_3 (support). (b) Cross-sectional SEM image of the columnar morphology of 1 µm-thick $HfN_{0.8}$ membranes. (c) Cross-sectional TEM image of an area close to the $HfN_{0.8}$/γ-Al_2O_3 interface. (d-e) High-resolution TEM images revealing the nanogranular morphology of $HfN_{0.8}$ membranes deposited at (d) 500^{o}C and (e) 25^{o}C.

5-3-2 Hydrogen permeability

Fig. 5-5(a) depicts the hydrogen and nitrogen fluxes (J_{H2} and J_{N2}, respectively) of 500 nm-thick HfN_x membranes deposited at 500 °C. To determine hydrogen permeability and selectivity, the surfaces of the membranes were exposed to 50 vol%-H_2/N_2 mixtures and out gases from the support side were analyzed (see 5-2-1(b) for more details). The porous alumina supports yield hydrogen temperature-independent fluxes of H_2 is 2.5×10^{-6} and N_2 is 1.4×10^{-6} mol cm^{-2} s^{-1} (Fig. 5-5(a)).

Apparently, HfN_x membranes exhibit hydrogen permeability mediated via the thermally-activated mass diffusion in their matrix. In both x = 0.8 and 1.0, J_{H2} slightly increased at temperatures $T \geq 250$°C, reaching values greater than ~7.1×10^{-7} mol cm^{-2} s^{-1} at 500°C, whereas J_{N2} is temperature independent, exhibiting a value of ~2×10^{-8} mol cm^{-2} s^{-1}. Hence, J_{H2} is at least 30 times higher than J_{N2} at 500°C. The J_{N2} measured for HfN_x can be attributed to a small leak in the seal, because the value is equivalent to the value measured for a thick stainless plate used as a dummy specimen (Fig. 5-5(a)). The flux of helium through $HfN_{0.8}$ is identical to that of nitrogen, despite the fact that He molecules are smaller than those of H_2 (see J_{He} in Fig. 5-5(a)), thus proving that hydrogen transport in HfN_x membranes does not concern with diffusion through pinholes or cracks. It is concluded that HfN_x membranes carry out selective hydrogen permeation due to their hydrogen diffusivity.

The J_{H2} values of $HfN_{0.8}$-500 and $HfN_{1.0}$-500 are very similar to each other in the measured temperature range: both exhibit less pronounced temperature dependence at $T \leq 200$ °C, however, are clearly temperature-dependent at $T \geq 250$°C (Fig. 5-5(a)). As will be described in the following sections, hydrogenation of HfN_x occurs spontaneously at

the ambient hydrogen pressure at around 25°C and thus the related Gibbs energy of reaction must be negative under the experimental conditions, which indicates that the mobile hydrogen concentration decreases with increasing temperature. Accordingly, the weak thermal activation of J_{H2} at $T \leq 200$°C is responsible for a decrease in mobile hydrogen concentration. The slope of the plot at $T \geq 250$°C can be used to estimate the hydrogen diffusion barriers because diffusivity activation is expected to dominate the reduction in mobile hydrogen in that region. The corresponding activation energy (E_a) of HfN_x-500 at $T \geq 250$°C is determined to be 11 kJ mol^{-1}, which is smaller than that of hydrogen diffusion in Pd metal (26 kJ mol^{-1}) (Fig. 5-5(b)).[22] Therefore, it can be deduced that the J_{H2} value of 500 nm-thick $HfN_{0.8}$ is at several orders of magnitude higher than that of a Pd membrane with a technologically limited thickness of 5 μm at 25°C (Fig. 5-5(a-b)). It is to be noted that the calculated E_a value is smaller than those of the recently-discovered hydride ion-conductors, such as $La_{2-x-y}Sr_{x+y}LiH_{1-x+y}O_{3-y}$[23] and BaH_2.[24]

The inversed proportional relationship between hydrogen permeability and thickness (L) of HfN_x membranes reveals that the surface kinetics for hydrogen incorporation does not mainly concerns the permeation rate (Fig. 5-5(b)). In case of thermally-activated jumps of hydrogen atoms or ions, the ratio between hydrogen and deuterium fluxes, J_{H2}/J_{D2}, should be close to $\sqrt{M_D}/\sqrt{M_H} \sim 1.4$ due to the $\sqrt{M}$ dependency of the jump rate.[25] Fig. 5-6 depicts the relaxation in the permeation flux upon switching between H_2 and D_2 supplies at a fixed temperature. The permeation fluxes decays by switching from H_2 to D_2, which results in 24% reduction in hydrogen fluxes, and subsequently recover to the original level upon switching back to H_2. Thus, the observed J_{H2}/J_{D2} ratios are about 1.30 at every temperature, revealing that hydrogen transport through HfN_x membranes is

driven by thermally-assisted mass diffusion in the matrices. TEM confirms that the morphology of the membranes remained unchanged before and after hydrogen permeation tests in a heating and cooling cycle between 25-500ºC (Fig. 5-7).

5-3-3 Mobile hydrogen species

It is known that protonic defects in various p-type nitride semiconductors favor the formation of amide-like defect complexes via association with N anions.[1-4] In the Kröger-Vink notation, the above reaction is denoted as shown below.

$$N_N^{\times} + H_2(g) \rightarrow (NH_2)_N^{\bullet\bullet} + e' \quad (5\text{-}3)$$

Meanwhile, hydridic defects in n-type semiconductors are normally created by association with metal (M) cations.[5,6,26,27]

$$M_M^{\times} + 1/2\ H_2\ (g) + e' \rightarrow (MH)_M' \quad (5\text{-}4)$$

To evaluate the formation of hydridic Hf-H groups, hydrogenated $HfN_{0.8}$-500 and $HfN_{1.0}$-500 were probed by ^{1}H-NMR (Fig. 5-8). The broad band centered at δ = 6 p.p.m. corresponds to the hydroxyl groups of the sacrificial mesoporous γ-Al_2O_3 layers. Both films show sharp peaks at δ = 1.91 p.p.m. and a shoulder at 1.62 p.p.m., which can be assigned to the doped hydrogen due to its being more pronounced in samples hydrogenated at 500°C. Hayashi et al. investigated the relationship between the ^{1}H-chemical shift $\delta_{iso}(H^-)$ and M–H bonding length of metal hydride systems and proposed the following empirical equation.[28-31]

$$\delta_{iso}(H^-)\ (\text{p.p.m.}) = 0.070\ d_{M-H}\ (\text{pm}) - 11.5 \quad (5\text{-}5)$$

Using the Hf–H bonding length (184 pm)[32], Eq. (5-5) calculates the $\delta_{iso}(H^-)$ value to be about 1.4 ppm, which is very close to the observed δ value. Moreover, the observed δ

value is much smaller than those of the protonic hydrogen in Hf-NH (4.9 p.p.m.)[33] or Hf-NH_2 moieties (11.5 p.p.m.).[34] These spectroscopic features clarify that the doped hydrogen in HfN_x is present in the form of H^- ions rather than as H^+ ions by coupling with Hf cations. As the width of NMR peaks can be correlated with the reciprocal of the spin relaxation time,[35] the peaks at δ = 1.91 ppm can be assigned to fast-diffusing hydridic dopants and the another to less-mobile hydrogen.

In situ FT-IR analysis proves the formation of hydridic Hf-D groups through H/D isotopic exchange (Fig. 5-9(a-b)). Pristine $HfN_{0.8}$-500 films showed Hf-N stretching bands at 900 cm^{-1} [36] and bands of hydrocarbons, water, and CO_2 adsorbs at ~2900, 1650, and 2350 cm^{-1}, respectively.[37] Switching from H_2 to D_2 atmosphere at 400°C triggers the development of the Hf-D stretching band[38] at ~1200 cm^{-1}, whereas the Hf-D band completely disappears upon switching back to H_2 (Fig. 5-9(c)). Unfortunately, Hf-H bands (~1600 cm^{-1})[36] are not evident by overlapped with H_2O adsorbs. Although amide-like $(NH_2)_N^{\bullet\bullet}$ defect complexes in metal nitrides have been reported to exhibit N-H and N-D stretching in the 3000–3300 cm^{-1} and 2100–2300 cm^{-1} regions, respectively,[3-5] such bands were not evident in the case of $HfN_{0.8}$, indicating that protonic H defects are not dominantly formed in HfN_x. The similar H/D exchange also take place in $HfN_{1.0}$ (Fig. 5-10). Therefore, the NMR and FT-IR results confirms that hydrogen act as an electron accept in HfN_x by associating with Hf cations.

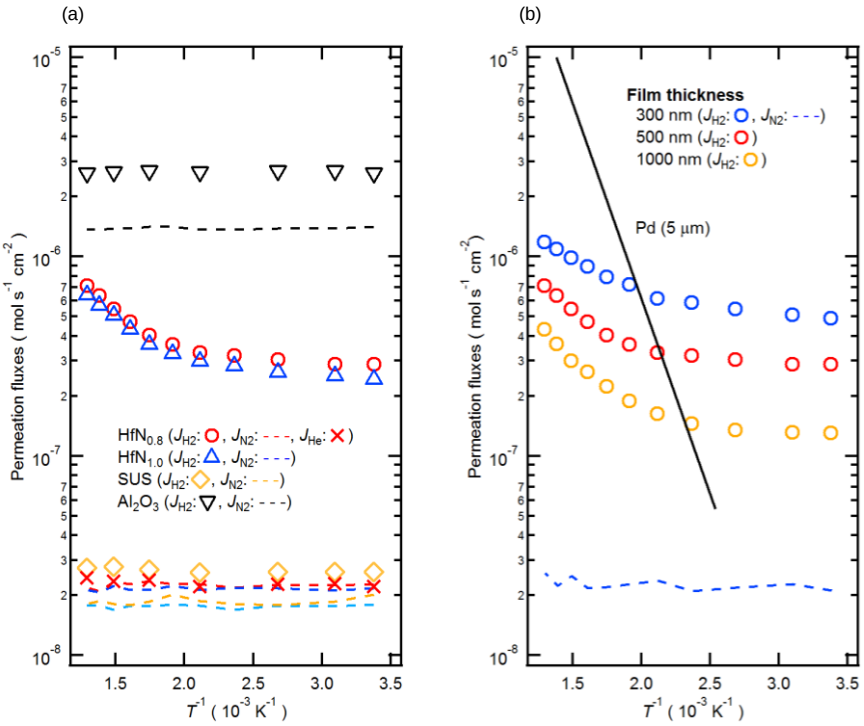


Fig. 5-5 Hydrogen permeabilities of HfN_x membranes at temperatures ranging between the ambient conditions and 500°C. (a) Arrhenius plots of hydrogen (J_{H2}, filled symbols) and nitrogen (J_{N2}, dashed lines) fluxes through 500 nm-thick $HfN_{0.8}$-500 and $HfN_{1.0}$-500 membranes when 50 vol% H_2/N_2 gas mixtures are supplied at 100 sccm. J_{H2} and J_{N2} of the bare porous alumina support were also measured under identical conditions along with the helium flux (J_{He}) through $HfN_{0.8}$ using a 50 vol% H_2/He gas mixture. To calibrate the contribution of background gas leakage from the sample holder, J_{N2} was measured for a 0.3 mm-thick SUS plate exposed to pure N_2 gas. (b) J_{H2} of $HfN_{0.8}$-500 membranes of different thicknesses; J_{N2} of a 300 nm-thick membrane is indicated. Hydrogen flux through a 5 μm-thick Pd foil at ΔP = 50 kPa was calculated using previously reported permeability values.[22]

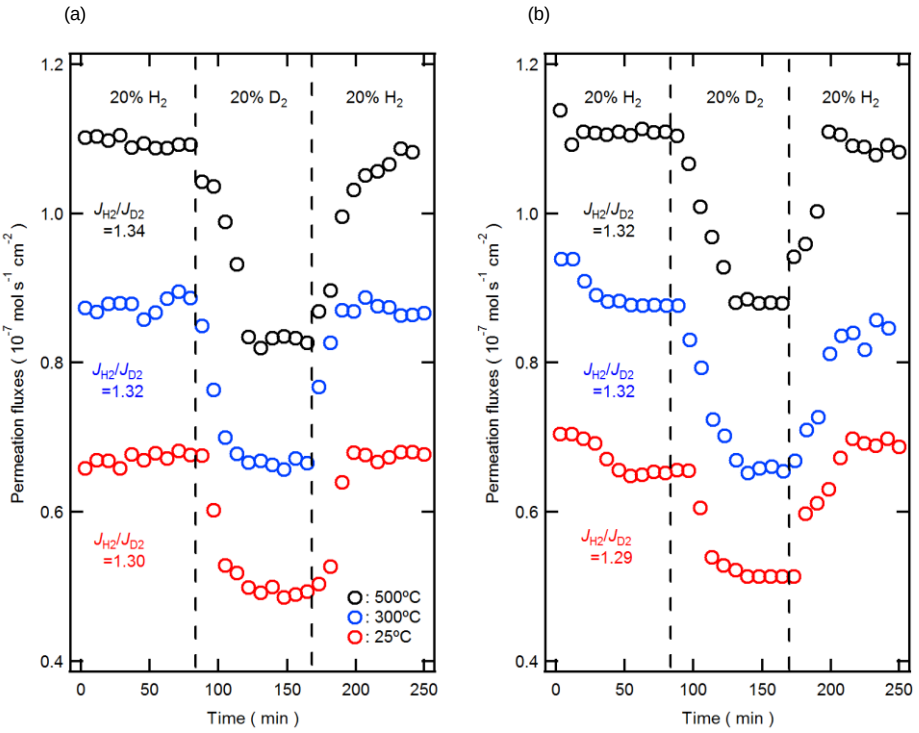


Fig. 5-6 H/D isotope effect on hydrogen fluxes through 1.0 µm-thick (a) $HfN_{0.8}$-500 and (b) $HfN_{1.0}$-500 membranes at 25, 300, and 500°C, as determined by switching between 20 vol% H_2 and 20 vol% D_2 in N_2. The dashed lines indicate the timing of atmosphere switching.

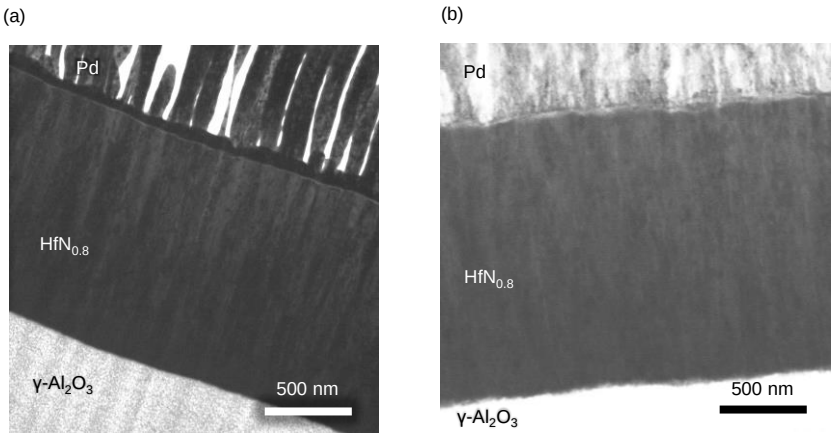


Fig. 5-7 Cross-sectional TEM images of $HfN_{0.8}$ samples (a) before and (b) after hydrogen permeation test.

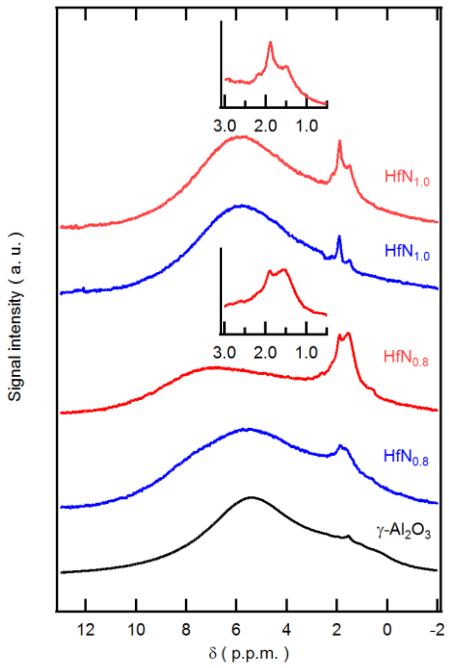


Fig. 5-8 ^{1}H NMR spectra of $HfN_{0.8}$ and $HfN_{1.0}$ films (1 μm thick) detached from Si substrates with a 100 nm-thick γ-Al_2O_3 sacrificial coating. The red lines represent the as-prepared films, while the blue lines represent those heated in 50 vol% H_2/Ar at 500°C for 1 h. The black line represents the spectrum of the sacrificial γ-Al_2O_3 layer.

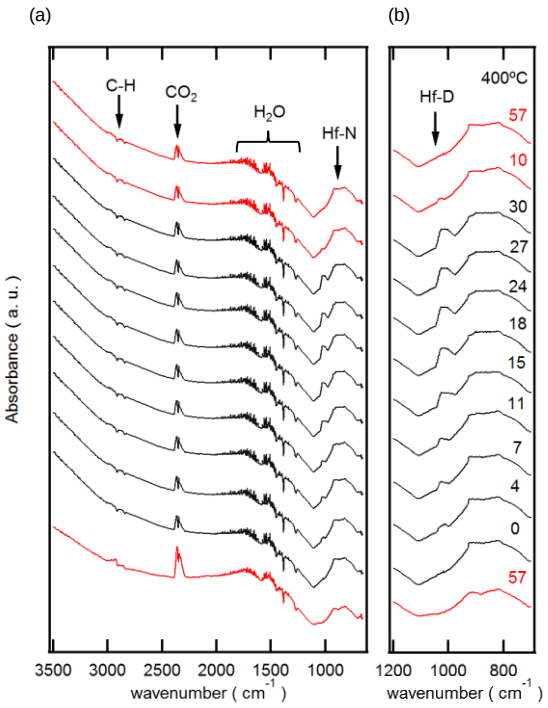


Fig. 5-9 *In situ* FT-IR spectra of $HfN_{0.8}$-500 membranes (500 nm thick). The films were initially exposed to a 20 vol% H_2/Ar atmosphere for 1 h, followed by switching to 20 vol% D_2/Ar for 30 min and then reverting to 20 vol% H_2/Ar for 1 h. The spectra recorded for H_2 are shown in red and those obtained for D_2 are shown in black. (a) FT-IR survey spectra (650–3500 cm^{-1}) and (b) expansion of the Hf-D stretching region at 400°C. The numbers in (b) indicate the time (min) to start measuring each spectrum with the time to switching the atmosphere being defined as 0 min. The measurement time of a spectrum is about 2.5 min.

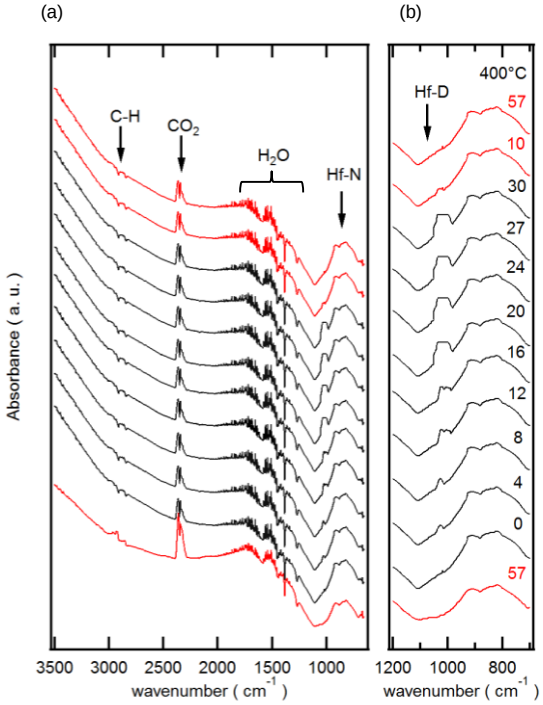


Fig. 5-10 *In situ* FT-IR spectra of $HfN_{1.0}$-500 membranes (500 nm thick). (a) *in situ* FT-IR spectra of the 650-3500 cm^{-1} region in 100% H_2 atmosphere at 100-400°C and in 20% D_2 atmosphere at 400°C. (b) expansion of the Ti–D stretching region at 400°C. The numbers in (b) indicate the time (min) to start measuring each spectrum with the time to switch atmosphere being defined by 0 min. The measurement time of a spectrum is about 2.5 min.

5-3-4 Grain size dependence of permeability and solubility

The above findings unambiguously demonstrate that nanocrystalline HfN_x membranes exhibit rapid diffusion of the hydridic defects which are incorporated into HfN_x membranes via association with Hf cations. In nanocrystalline TiN_x (x = 0.7 and 1.0) systems, the hydridic carriers mainly exist along the grain boundary as Ti-H terminal groups rather than as surface-hydrogenated crystallites,[8] and hence hydrogen diffusion is caused by grain boundary hopping transport via a bond exchange process between Ti-H terminal groups.[8] Based on a brick layer model,[39,40] where cubic grain cores are arranged on a simple cubic lattice (the length is d_{av}) separated by homogeneous grain boundary layers (Fig. 5-8(a)), such interfacially-controlled diffusivity should feature a linear scalability between both hydrogen solubility and permeability and volumetric surface area, which can be correlated with the reciprocal of grain size (d_{av}^{-1}).

In fact, the hydrogen permeability (J_{H2}) of HfN_x increases in proportion with d_{av}^{-1}, thus providing clear evidence for the interfacially-controlled diffusion of hydridic defects (Fig. 5-11(a)). The linear scalability of J_{H2} vs d_{av}^{-1} is clearly shown in Fig. 5-12(b). In the case of $HfN_{0.8}$, decreasing d_{av} from 25 nm ($HfN_{0.8}$-500) to 14 nm ($HfN_{0.8}$-200) or 11 nm ($HfN_{0.8}$-25) increases J_{H2} by a factor of about 1.5 or 1.8, respectively; the magnitude of change is similar at all temperatures, with the factors being roughly equivalent to the inversed ratio of the d_{av} values which are $(14\ nm/25\ nm)^{-1} \sim 1.8$ or $(11\ nm/25\ nm)^{-1} \sim 2.2$, respectively. Similarly, the ratios of the J_{H2} values of $HfN_{1.0}$-25 (d_{av} = 10 nm) with -200 (d_{av} = 13 nm) or -500 (d_{av} = 24 nm) are approximately 1.5 or 2.0, respectively, at all temperatures, which is in agreement with the corresponding d_{av}^{-1} ratios, $(10\ nm/13\ nm)^{-1} \sim 1.3$ or $(10\ nm/24\ nm)^{-1} \sim 2.4$, respectively.

To validate interfacial hydridic solubility, room temperature hydrogen sorption of the HfN_x films is monitored using a 5-MHz QCM (Fig. 5-12)[41,42] by depositing a $HfN_{0.8}$ or $HfN_{1.0}$ film directly on an Au electrode of a quartz resonator at 25 °C or 200°C (it is difficult to deposit at 500°C because of the damages in the resonator). Upon exposing $HfN_{0.8}$-200 and $HfN_{0.8}$-25 to H_2, their base frequencies are relaxed by decreasing to –15.5 and –18.4 Hz, respectively, which corresponds to the incorporation of 0.73 and 0.86 μg of hydrogen, respectively, at p_{H2} = 50 kPa and 25°C. Using geometric film volumes and ideal molar density (7.17×10^{-2} mol cm^{-3}),[43] hydrogen solubility (S_H), which is defined by the H/Hf ratio under equilibrium, was determined to be 0.10 and 0.12 for $HfN_{0.8}$-200 and $HfN_{0.8}$-25 at 25°C, respectively. The S_H values thus determined are summarized in Table 5-3 and Fig. 5-13(b).

Clearly, the S_H of $HfN_{0.8}$-25 is 1.2 times higher than that of $HfN_{0.8}$-200, which is in good agreement with the d_{av}^{-1} ratio of $HfN_{0.8}$-25 and $HfN_{0.8}$-200 (~1.3) and thus the corresponding J_{H2} ratio (~1.13). Similarly, the S_H of $HfN_{1.0}$-25 (0.12) is larger than that of $HfN_{1.0}$-200 (0.093) by a factor of 1.3 and this value is also in agreement with the d_{av}^{-1} (10 nm/13 nm ~ 1.3) and J_{H2} ratios (~1.41) between $HfN_{1.0}$-25 and $HfN_{1.0}$-200 (Table 5-3), indicating that size-enhanced permeability is identical to the increase in hydrogen solubility when the grain size is reduced.

Regardless of the large differences in nitrogen deficiencies, the S_H of (100)-oriented $HfN_{1.0}$-200 is very close to that of (100)-oriented $HfN_{0.8}$-200 as the d_{av} values of both films are similar (Table 5-3 and Fig. 5-13(b)). This strongly suggests that nitrogen vacancies in the grain bulk do not concern themselves with the diffusion of hydridic defects. In a separate experiment, the defect-formation energies (ΔE_{def}) of H-HfN systems

were calculated by DFT, which yielded a negative enthalpy for H intake into nitrogen vacancy (V_N); on the other hand, large positive enthalpies (>1.8 eV) were observed for various H-interstitials even after lattice relaxation (Fig. 5-14), indicating that hydrogen is not positioned at a favorable energy level to be introduced into the interstitials of HfN crystals. The experimental and theoretical results together lead to a clear conclusion that mobile hydrogens cannot enter deeply into the interior of the grain bulk.

Moreover, the QCM-measured solubility (S_H) is in close agreement with the hydrogen content needed for the monolayer coverage of overall crystallite surfaces with Hf-H terminal groups. Assuming that the hydrogenation of each crystallite occurs by obeying the Langmuir monolayer chemisorption[44] of hydrogen onto surface Hf sites and the monolayer coverage is achieved under equilibrium conditions at $p_{H2} = 0.5\ p_0$, S_H should be equal to the fraction of surface Hf cations to total ones in (100)-oriented HfN nanocubes (F_{Hf}). In the case of the brick layers built up with a (100)-oriented NaCl-type nanocube (Fig. 5-8(a)), the fraction of surface cations M (F_M) can be calculated using a general equation as follows.

$$F_M = 3\ l\ {d_{av}}^{-1} \tag{5-6}$$

Here, l is a lattice constant. The theoretical S_H value is calculated to be equal to F_{Hf} using Eq. (5-6) and a HfN lattice parameter,[43] as shown in Fig. 5-13(b). The observed S_H values of $HfN_{0.8}$-200 (d_{av} = 14 nm), $HfN_{1.0}$-200 (d_{av} = 13 nm), $HfN_{0.8}$-25 (d_{av} = 11 nm), and $HfN_{1.0}$-25 (d_{av} = 10 nm) are 0.10, 0.093, 0.12, and 0.12, respectively, and are in agreement with the theoretical S_H values (Fig. 5-13(b)), confirming that most of the surface cationic sites coordinated with hydridic hydrogens at the ambient temperature and hydrogen pressure. Hence, S_H is equivalent to F_{Hf}.

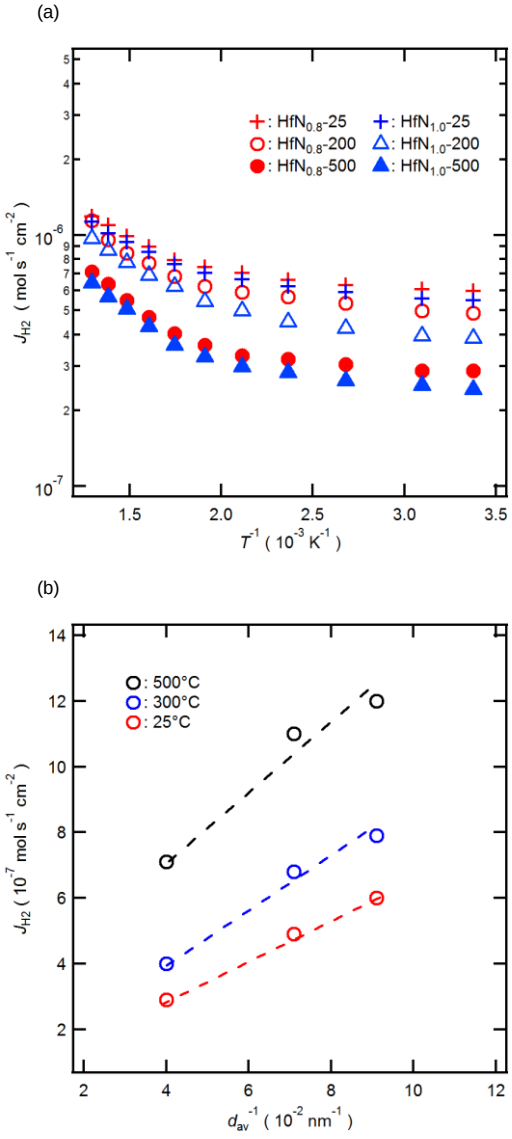


Fig. 5-11 (a) Arrhenius plots of hydrogen flux (J_{H2}) of $HfN_{0.8}$ and $HfN_{1.0}$ films (500 nm thick) prepared at 500, 200, and 25°C, indicating an enhancement in the hydrogen permeability of nanocrystalline HfN_x membranes with a reduction in the grain size. Mixed gases of 50%-H_2/N_2 are supplied at 100 sccm to the entrance side. (b) Linear d_{av} scaling of the hydrogen permeability of $HfN_{0.8}$ membranes. The circles show the plots of J_{H2} measured at 25 (red), 300 (blue), and 500 °C (black) and the dashed lines represent the fitting curves.

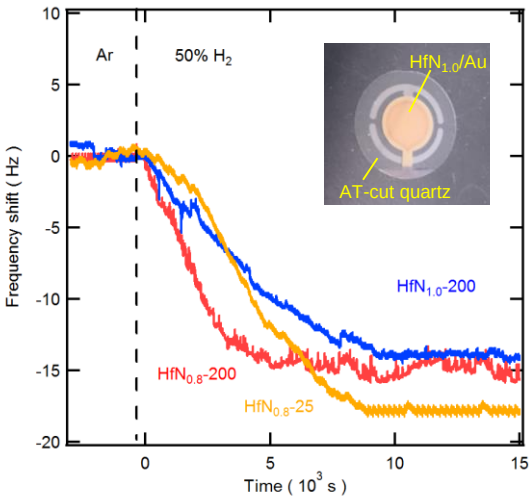


Fig. 5-12 Response transient of QCM frequency shifts due to hydrogen adsorption on 1 µm-thick $HfN_{0.8}$ and $HfN_{1.0}$ films deposited at 25 or 200°C on Au film oscillator electrodes (1.32 cm^2). The measurements were performed by switching from pure Ar to 50 vol% H_2/Ar at 25°C. The dashed lines indicate the timing for atmosphere switching. The inset shows an optical image of a quartz resonator with Au electrode onto which a $HfN_{1.0}$-200 film is deposited.

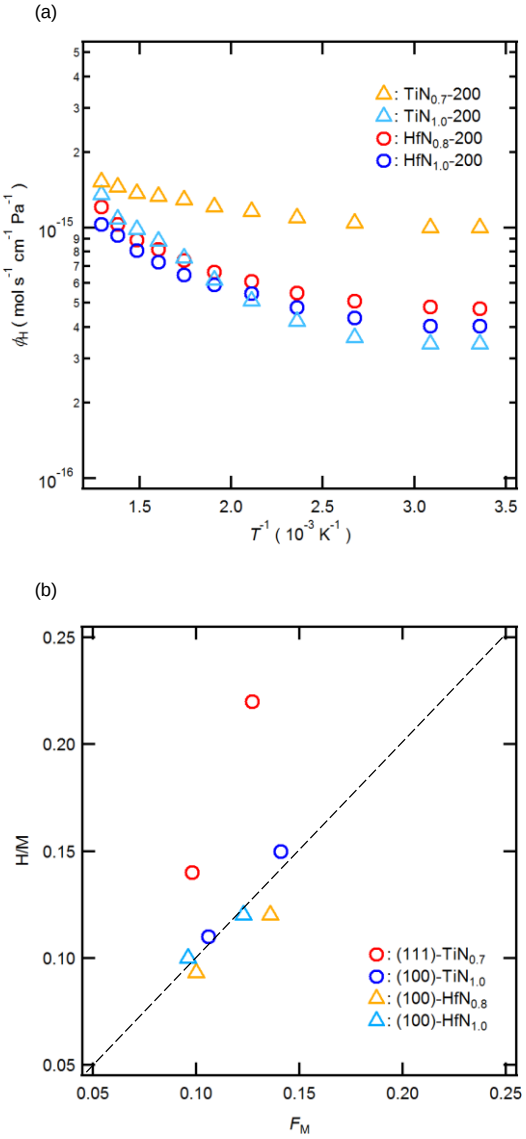


Fig. 5-13 (a) Relationship between hydrogen permeation coefficients (φ_H) of HfN_x-200 (x = 0.8 and 1.0) and TiN_x-200 (x = 0.7 and 1.0) membranes at temperatures in the range of 25–500°C. (b) Relationship between hydrogen solubility (S_H) and reciprocal average crystallite sizes (d_{av}^{-1}) of HfN_x-200, 25, TiN_x-200 and 25. Here, the fractions of surface M cations (F_M) are used as the x-sets, as calculated by eqn (5-6). The theoretical S_H value calculated by equaling it to F_M is shown as a dashed line. The details are described in the main text. The data corresponding to TiN_x-200 (x = 0.7 and 1.0) is sourced.[8]

5-3-5 Comparison of HfN_x and TiN_x

A comparison between HfN_x and TiN_x discloses that controlling the grain growth orientation is crucial for the hydridic conductivity of transition metal nitride-based membranes. Fig. 5-13(a) shows the hydrogen permeation coefficients (ϕ_H; mol s^{-1} cm^{-1} Pa^{-1}) of 500 nm-thick HfN_x-200 (x = 0.8 and 1.0) and 600 nm-thick TiN_x-200 (x = 0.7 and 1.0)[8] membranes as functions of the reciprocal of temperature. ϕ_H was determined according to Eq. (5-7)[45]

$$\phi_H = \frac{J_{H2} L}{(p_{H2}' - p_{H2}'')} \tag{5-7}$$

where p_{H2}' is the partial pressure of hydrogen at the entrance and p_{H2}'' is the partial pressure of hydrogen at the exit, i.e. the MN_x/Al_2O_3 interface. L is the film thickness and J_{H2} is the hydrogen flux of the MN_x membrane. p_{H2}'' can be experimentally determined, the details of which are described in the Supporting Information.

The behavior of (100)-$TiN_{1.0}$[8] is analogous to that of both (100)-$HfN_{0.8}$ and $HfN_{1.0}$, as the plots of the three (100)-oriented films overlap with each other at temperatures greater than 250°C and exhibit similar E_a values in the range of 9.6–10 kJ mol^{-1} (Table 5-3). Moreover, the observed S_H of (100)-$TiN_{1.0}$ (0.11) is comparable to the theoretical value calculated using the TiN lattice constant[43] as well as to that of HfN_x-200 (Fig. 5-13(b)), which indicates that the number of surface cationic sites on both HfN_x and TiN_x nanograins is similar to that of ideal NaCl-type cubic crystals. The ϕ_H value of (111)-$TiN_{0.7}$ is clearly larger than that of other (100)-oriented membranes and the S_H is largely deviated from the theoretical line corresponding to the (100)-oriented films (Fig. 5-13(b)). These features can be attributed to the relatively large population of cationic sites on (111)

surfaces because of the following reason. Compared to the (100) plane with equal amounts of Ti and N, the (111) surface alternatively exposes pure Ti or N close-packed layers (Fig. 5-15(a-b)). The aforementioned results clearly demonstrate that the hydrogen permeability of HfN_x nanocrystalline membranes is comparable to those of TiN_x systems with an equivalent grain-growth orientation. It is concluded that such nanocrystalline metal nitrides with relatively high Fermi energy levels and significantly high hydridic conductivity are potential candidates for Pd-alternative hydrogen membranes.

Table 5-3 Structural and hydrogen-transport properties of 500-nm HfN_x (x = 0.8 and 1.0) and 600-nm TiN_x (x = 0.7 and 1.0) membranes. The data corresponding to TiN_x membranes is sourced.[8]

samples	d_{av} (XRD) / nm	Crystal orientation	J_{H2} at 500°C / mol cm^{-2} s^{-1}	J_{H2} at rt / mol cm^{-2} s^{-1}	E_a of permeability / kJ mol^{-1}	composition
$HfN_{0.8}$-500	25	(100)	7.1×10^{-7}	2.9×10^{-7}	4.2 ($T \leq 200$°C) 11 ($T \geq 250$°C)	–
$HfN_{0.8}$-200	14	(100)	1.1×10^{-6}	4.9×10^{-7}	4.3 ($T \leq 200$°C) 9.6 ($T \geq 250$°C)	$HfN_{0.8}H_{0.10}$
$HfN_{0.8}$-25	11	(100)	1.2×10^{-6}	6.0×10^{-7}	4.4 ($T \leq 200$°C) 9.2 ($T \geq 250$°C)	$HfN_{0.8}H_{0.12}$
$HfN_{1.0}$-500	24	(100)	6.4×10^{-7}	2.4×10^{-7}	3.7 ($T \leq 200$°C) 11 ($T \geq 250$°C)	
$HfN_{1.0}$-200	13	(100)	9.6×10^{-7}	3.9×10^{-7}	4.3 ($T \leq 200$°C) 10 ($T \geq 250$°C)	$HfN_{1.0}H_{0.093}$
$HfN_{1.0}$-25	10	(100)	1.1×10^{-6}	5.5×10^{-7}	4.3 ($T \leq 200$°C) 9.1 ($T \geq 250$°C)	$HfN_{1.0}H_{0.12}$
$TiN_{0.7}$-200	14	(111)	1.2×10^{-6}	7.8×10^{-7}	3.0 ($T \leq 200$°C) 5.6 ($T \geq 250$°C)	$TiN_{0.7}H_{0.15}$
$TiN_{1.0}$-200	12	(100)	1.1×10^{-6}	2.6×10^{-7}	6.1 ($T \leq 200$°C) 9.8 ($T \geq 250$°C)	$TiN_{1.0}H_{0.11}$

5-4 Conclusions

In summary, HfN_x (x = 0.8 and 1.0) membranes comprising rectangular-shaped nanograins with lengths in the range of a few tens of nanometers exhibit room-temperature hydrogen permeability due to the enhanced grain boundary diffusion of hydridic ions. Similar to TiN_x systems, nanocrystalline matrices of HfN_x are readily hydrogenated to form Hf-H terminal groups over the crystallite surfaces and thus, hydridic ions can migrate through the grain boundary region owing to a bond exchange between Hf-H groups (Fig. 5-15(c)). Hence, the hydrogen solubility of the membranes increases with decreasing crystallite size and thus, 500 nm-thick $HfN_{0.8}$ membranes with reduced crystallite sizes (11 nm) exhibit hydrogen solubility of 3×10^{-7} mol cm^{-2} s^{-1}, exceeding that observed for the state-of-the-art Pd membranes at ambient temperature. Both $HfN_{1.0}$ and $HfN_{0.8}$ films exhibit similar E_a (about 11 kJ mol^{-1}) and S_H (about 0.10); these values are comparable to those of $TiN_{1.0}$ films with equivalent crystallite sizes. Such similarities can be attributed to the same preferred (100) orientation during grain growth. The current results establish a general guide to design hydrogen membranes using metal nitrides, suggesting that nitrides with significantly high Fermi energy levels and small crystallite sizes are promising high hydridic ion conductors. These findings open up a new way towards non-Pd hydrogen separation systems for sustainable hydrogen technology.

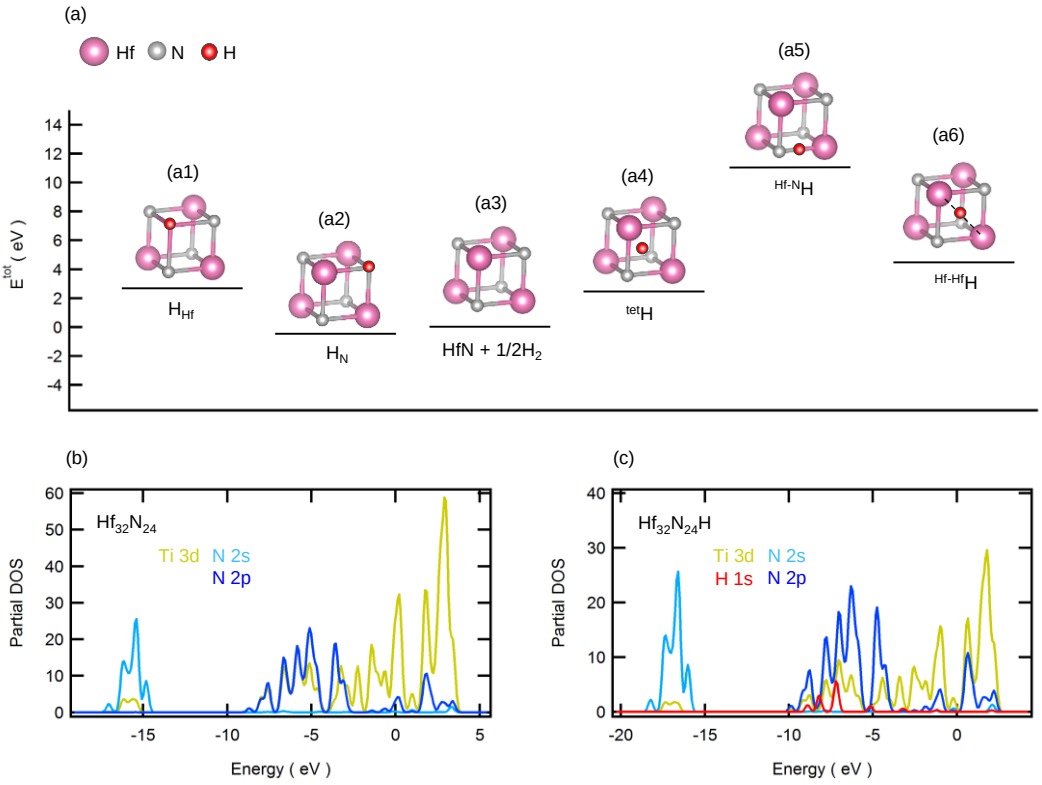


Fig. 5-14 (a) The DFT energies calculated for 2×2×2 supercells of various hydrogen defect models. (a3) shows the total energies of the system comprising stoichiometric HfN phase ($Hf_{32}N_{32}$) and 1/2 H_2 gas. (a1) $Hf_{31}N_{32}(H_{Hf})$: H defect occupying a Hf vacancy of Hf-deficient $Hf_{31/32}N$ phase. (a2) $Hf_{32}N_{24}(H_N)$: H defect occupying a N vacancy of N-deficient $HfN_{24/32}$ phase. (a4, a5, a6) $Hf_{32}N_{32}H_1$: HfN phase with an H interstitial at (a4) tetrahedral site of fcc Hf sublattice (^{tet}H), (a5) center of the closest Hf-N bond ($^{Hf\text{-}N}H$) and (a6) center of the closest Hf-Hf bond ($^{Hf\text{-}Hf}H$). (b-c) Partial DOS of $Hf_{32}N_{24}$ and $Hf_{32}N_{24}H$. H 1*s* state is offset by ×2.

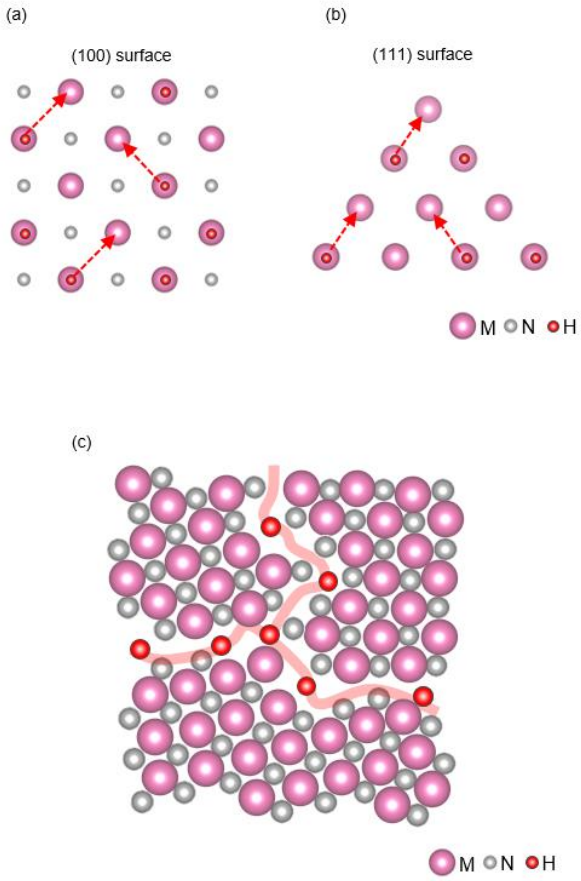


Fig. 5-15 (a-b) Schematic representation of a hydride ion bound to a M cation on the (100) surface built up by an alternative stacking of M cations and N anions and a (111) surface comprising of a pure M close-packed layer. (c) Schematic illustration of hydride ion diffusion in grain boundary.

5-5 References

1. Gelhausen, O.; Phillip, M. R.; Goldys, E. M.; Paskova, T.; Monemar, B.; Strassburg, M.; Hoffmann, A. *Phys. Rev. B.* **2004**, 69, 125210.
2. Kleekajai, S. Jiang, F.; Colon, K.; Stavola, M.; Fowler, W. B.; Martin, K. R.; Polimeni, A.; Capizzi, M.; Hong, Y. G.; Xin, H. P.; Tu, C. W.; Basis, G.; Rubini, S.; Martelli, F. *Phys. Rev. B.* **2008**, 29, 085213.
3. Suihkonen, S.; Pimputkar, S.; Speck, J. S.; Nakamura, S. *Appl. Phys. Lett.* **2016**, 108, 202105.
4. Janotti, A.; Zhang, S. B.; Wei, S. H. *Phys. Rev. Lett.* **2002**, 88, 125506.
5. Janotti, A.; Zhang, S. B.; Wei, S. H. Van de Walle, C. G. *Phys. Rev. Lett.* **2002**, 88, 086403.
6. Van de Walle, C. G.; Neugebauer, J. *Nature.* **2003**, 423, 626-628.
7. Fujii, R.; Gotoh, Y.; Liao, M. Y.; Tsuji, H.; Ishikawa, J. *Vacuum* **2006**, 80, 832-835.
8. Kura, C.; Kunisada, Y.; Tsuji, E.; Zhu, C.; Habazaki, H.; Müller, M. P.; de Souza R. A.; Aoki, Y. *Nat. Energy*, **2017**, 2, 786-794.
9. Gotoh, Y.; Tsuji, H.; Ishikawa, J. *J. Vac. Sci. Technol. B.* **2003**, 21, 1607.
10. Uhlhorn, R. J. R.; Zaspalis, V. T.; Keizer, K.; Burggraaf, A. J. *J. Mater. Sci*. **1992**, 27, 527-552.
11. de Vos, R. M.; Verweij, H. High-selectivity, High-flux silica membranes for gas separation. *Science*. **1998**, 279, 1710-1711.
12. Climent-Font, A.; Wätjen, U.; Bax, H. *Nucl. Inst. Methods. Phys. Rev. B.* **1992**, 71, 81-86.

13. Perdew, J. P.; Burke, K.; Ernzerhof, M. *Phys. Rev. Lett*, **1997**, 78, 1396.

14. Kresse, G.; Halfner, J. *J. Phys. Rev. B.* **1994**, 49, 14251.

15. Kresse, G.; Furthmüller, J. *Compt. Mat. Sci.* **1996**, 6, 15.

16. Kresse, G.; Halfner, J. *J. Phys. Rev. B.* **1993**, 47, 558.

17. Kresse, G.; Furthmüller, J. *J. Phys. Rev. B.* **1996**, 54, 11169.

18. Blochl, P. E. *Phys. Rev. B.* **1994**, 50, 17953.

19. Kresse, G.; Joubert, D. *Phys. Rev. B.* **1999**, 59, 1758.

20. Monkhorst, H. J.; Pack, J. D. *J. Phys. Rev. B.* **1976**, 13, 5188.

21. Iwazaki, Y.; Suzuki, T.; Tsuneyuki, S. *J. Appl. Phys.* **2010**, 108, 083705.

22. Holleck, G. L. *J. Phys. Chem*. **1970**, 74, 503-511.

23. Kobayashi, G.; Hinuma, Y.; Matsuoka, S.; Watanabe, A.; Iqbal, M.; Hirayama, M.; Yonemura, M.; Kamiyama, T.; Tanaka, I.; Kanno, R. *Science*. **2016**, 351, 1314-1317.

24. Verbraeken, M. C.; Cheung, C. Suard, E.; Irvine, J. T. S. *Nature. Mater.* **2014**, 14, 95-100.

25. Bonanos, N.; Huijser, A.; Poulsen, F. W. *Solid State Ionics*. **2015**, 275, 9-13.

26. Holbech, J. D; Nielsen, B. B.; Jones, R.; Sitch, P.; Öberg, S. *Phys. Rev. Lett.* **1993**, 71, 875-878.

27. Sun, W. Qian, C.; He, L.; Ghuman, K. K.; Wong, A. P. Y.; Jia, J.; Jelle, A. A.; O'Brien, P. G.; Reyes, L. M.; Wood, T. E.; Helmy, A. S.; Mims, C. A.; Singh, C. V.; Ozin, G. A. *Nature Commun.* **2016**, 7, 125531-125539.

28. Hayashi, K.; Sushko, P. V.; Hashimoto, Y.; Shluger A. L.; Hosono, H. *Nat. Commun.* **2014**, 4514, 1-8.

29. Nicol A. T.; Vaughan, R. W. *J. Chem. Phys.* **1978**, 69, 5211.

30. Magusin, P. C. M. M.; Kalisvaart, W. P.; Notten P. H. L.; van Santen, R. A. *Chem. Phys. Lett.* **2008**, 456, 55-58.

31. Bowman, R. C.; Hwang, S. J.; Ahn C. C.; Vajo, J. J. *MRS Proc*, **2004**, 837, N3.6.

32. Weinhold F.; Landis, C. L. *Valency and Bonding. A Natural Bond Orbital Donor–Acceptor Prespective*; Cambridge university press: Cambridge, 2005.

33. Havlík, A.; Lamač, M.; Pinkas, J.; Růžička, A.; Horáček, M. *RSC Adv.* **2015**, 5, 59154-59166.

34. Hillhouse, G. L.; Bulls, A. R.; Samtarsoerp, B. D.; Bercaw, J. E. *Organometallics*, **1988**, 7, 1309.

35. Stejskal, E. O. *J. Chem. Phys.* **1965**, 43, 3597.

36. Wang, S.; Zhang, Y.; Sun, Y.; Xu, Y.; Yang, M. *J. Alloys Compd.* **2016**, 685, 828-835.

37. Nyquist R. A.; Kagel, R. O. *Handbook of Infrared and Raman Spectra of Inorganic Compounds and Organic Salts*; Academic press: Massachusetts, 1971.

38. Chertihin, G. V.; Andrews, L. *J. Am. Chem. Soc*, **1995**, 117, 6402-6403.

39. Kim, S.; Avila-Paredes, H. J.; Wang, S.; Chen. C. T.; De Souza, R. A.; Martin, M.; Munir, Z. A. *Phys. Chem. Chem. Phys.* **2009**, 11, 3035-3038.

40. Schlom, D. G.; Chen, Long-Qing.; Pan, X.; Schmehl, A.; Zurbuchen. M. A. *J. Am. Ceram. Soc.* 2008, 91, 2429-2454.

41. Aoki, Y.; Hashizume, M.; Onoue, S.; Kunitake, T. *J. Phys Chem. B*. **2008**, 112, 14578-14582.

42. Uekawa, N.; Kaneko K. *J. Phys. Chem. B.* **1998**, 102, 8719-8724.

43. Pierson, H. O. *Handbook of Chemical Vapor Deposition (CVD): Principle,*

Technology and Applications (Second Edition); Noyes Publications: New Jersey, 1999.

44. Conway, B. E. *Electrochim. Acta.* **1993**, 38, 1249-1258.
45. Schlom, D. G.; Chen, Long-Qing.; Pan, X.; Schmehl, A.; Zurbuchen. M. A. *J. Am. Ceram. Soc.* **2008**, 91, 2429-2454.

Chapter 6

Summary

In previous chapters, inorganic thin films exhibiting a pronounced mixed ionic-electronic conductivity were fabricated by RF sputtering; (a) The amorphous Ga(I) suboxide thin films were demonstrated to cause bulk oxide ion conductivity at room temperature due to the the correlation between negative charges on O^{2-} ions and $(4s)^2$ lone pair of Ga(I). (b) Nanocrystalline TiN_x and HfN_x with relatively high Fermi energy can show the excellent hydrogen permeability due to interfacial hydridic conduction in their nanostructured matrices. These current results propose a new guideline to design pronounced ionic conductivity of the sputter-deposited inorganic thin films and open up the potential applications of them for electronic and energy-related technologies. The outstanding results of this thesis were briefly summarized as follows.

In Chapter 1, the history and scientific backgrounds of mixed ionic-electronic conductors are introduced, describing ion conductors as a key component for various electric and energy applications. In addition, the importance of nanostructures and electron-defect interactions for ionic conductivity are also mentioned with describing the recent reports for nanostructure-enhanced ion transport properties. The convenience of reactive sputtering technique as a tool to fabricate such nanostructured materials are also mentioned.

In Chapter 2, the discovery of new resistive-switching functionality in amorphous Ga(I) suboxide, triggered by enhanced bulk oxide ion conductivity at room temperatures is described. Cr-doped amorphous gallium oxide thin films with tailored gallium valence state and oxygen deficiencies has been were successfully fabricated by RF cosputtering process of Ga_2O_3 and Cr. The Ga(I)-Ga(III) mixed valence state homogeneous oxide glass can be formed from a homogeneous mixture of Cr(0) metal atoms and Ga(III) oxides moieties deposited by cosputtering, because Cr(0) scavenges oxygen of Ga(III) oxide due to the relatively large negative energy of Cr-O bonding in comparison to Ga-O bonding by following: 3Ga(III) + 2Cr(0) → 3Ga(I) + 2Cr(III). Amorphous $Ga_{0.82}Cr_{0.18}O_{1.2}$ thin film with optimal Ga(I) contents can reveal remarkable homogeneous resistance switching due to the efficient bulk oxide ion conduction at room temperature, and thus, the film clearly involved multiple resistance state switching where the final device state is determined by bias history, since the oxygen vacancy donor profiles can be incrementally modified by bias duration or number of the applied short pulse biasing. The current results open up a new way to design the bulk mechanism resistive switching metal oxide thin films with tailored oxide ion conductivity.

In Chapter 3, room-temperature hydrogen separation was demonstrated for TiN_x (x = 0.7, 0.9, 1.0) nanocrystalline membranes with unprecedented hydride conductivity. The TiN_x membranes were deposited on porous aluminum support uniformly by RF reactive sputtering. The resultant membranes exhibited room-temperature hydrogen permeability due to enhanced grain boundary diffusion of hydride ions mediated by terminal Ti–H groups on internal grain surfaces with a low activation energy of ~5 kJ mol^{-1}. Hence, the flux of hydrogen through $TiN_{0.7}$ membranes reached to 5.3×10^{-7} mol cm^{-2} s^{-1} at 25°C

under applied hydrogen partial pressure of 50 kPa, which exceeded that observed for Pd membranes at ambient temperature. These nanocrystalline materials with preferred grain orientation and significantly reduced grain sizes could realise ultrafast hydrogen permeation due to grain-boundary diffusion of hydride ions and metallic conduction of the grain bulk.

In Chapter 4, the hydride ion diffusion pathway in TiN_x nanocrystalline membranes was identified more precisely in basis of the mechanism proposed in Chapter 3. The hydrogen permeability of TiN_x nanocrystalline membranes (x = 0.7 and 1.0) was characterized by controlled grain sizes and grain-growth orientation. The hydrogen transport mechanism was unambiguously identified as the grain boundary diffusion of hydric ions aided by Ti-H terminal groups formed over the hydrogenated grain surfaces. Hydrogen solubility was linearly scaled with inversed grain sizes attributed to the interfacial hydridic solubility, and thereby, the permeation coefficients are significantly enhanced with decreasing crystallites sizes, i.e. increasing grain boundary volumes. In addition, the (111)-oriented $TiN_{0.7}$ membranes possess higher hydrogen solubility and lower diffusion energy than (100)-oriented $TiN_{1.0}$ because relatively high Ti population on (111) increase the number of interfacial hydridic defects and reduce the bottleneck energy for jumping between adjacent Ti sites.

In Chapter 5, hydrogen permeability based on the mixed hydride ion-electron conduction was also demonstrated for HfN_x (x = 0.8 and 1.0) nanocrystalline membranes. The (100)-oriented crystalline membranes with crystalline sizes of 10's nm were prepared by RF reactive sputtering. The membranes with average crystalline sizes of 11 nm yielded hydrogen flux of 6×10^{-7} mol cm^{-2} s^{-1} at room temperature, which was higher than the Pd

membranes. Combined spectroscopic, permeability and microbalance measurements clarified that the nanocrystalline matrices were readily hydrogenated with forming Hf-H terminal group over the internal grain surfaces and efficient hydrogen permeation took place due to enhanced diffusion of hydridic defects through grain boundary, aided by Hf-H bond exchange process. In addition, the HfN_x film showed only (100) orientation irrespective of the presence or absence of nitrogen deficiency, and the value of hydrogen flux was similar in any composition, confirming that hydride defects favored to be incorporated into grain boundary region without entering into the bulk.

Combined with the results of TiN_x (Chapter 3 and 4), these findings establish a new guideline for Pd alternatives based on nanostructure-induced hydric conductivity of transition metal nitride nanomaterials; metallic nitrides which possess relatively high Fermi energy levels are promising candidates of hydride ion conductors.

In summary, pronounced ion conductivity and related novel functionality were demonstrated for the inorganic thin films fabricated by reactive sputtering with tailoring microstructures and precise-controlling nonstoichiometry. The results in this thesis clearly demonstrate that reactive sputtering techniques afford a strong tool to design nanostructured materials with high ionic conductivity triggered by optimal electronic structures and interfacial ionic pathways. Recent global concerns regarding energy and environmental issues has drawn a lot of academic and industrial interests to development of the functional materials which enables a precise control of the catalytic and electrochemical reactions for energy conservation and environmental protection aided by their ionic mobility. Despite the recent advances in material sciences, better ion

conductive materials at lower temperature is still needed in various energy and environmental applications, such as batteries, fuel cells, artificial catalysts, gas separation membranes and so on. The discovery of new materials, ideas and function for applications always vitalize the scientific activity, and this effort must be pursued in the future. The author also hopes that this thesis contributes to stimulating further development of Solid State Ionics.

List of publications

Papers published

1. Kura, C.; Aoki, Y.; Tsuji, E.; Habazaki H.; Martin, M. "Fabrication of a resistive switching gallium oxide thin film with a tailored gallium valence state and oxygen deficiency by rf cosputtering process" *RSC Advance*, **2016**, 6, 8964-8970.

2. Kura, C.; Kunisada, Y.; Tsuji, E.; Zhu, C.; Habazaki, H.; Nagata, S.; Müller, M. P.; De Souza, R. A.; Aoki, Y. "Hydrogen separation by nanocrystalline titanium nitride membranes with high hydride ion conductivity" *Nat. Energy*, **2017**, 2, 786-794.

3. Kura, C.; Fujimoto, S.; Kunisada, Y.; Kowalski, D.; Tsuji, E.; Zhu, C.; Habazaki, H.; Aoki, Y. "Enhanced hydrogen permeability of hafnium nitride nanocrystalline membranes by interfacial hydride conduction" *J. Mater. Chem. A,* **2018***,* 6, 2730-2741.

4. Kura, C.; Zhu, C.; Habazaki, H.; Aoki, Y. "Enhanced hydrogen permeability of TiN_x nanocrystalline membranes with tailored grain size and growth-orientation" *submitted*.

Other publications

1. 青木 芳尚，倉 千晴，國貞 雄治，朱 春宇，幅崎 浩樹「窒化チタン微結晶膜におけるヒドリドイオン伝導の発現とそれによる常温水素膜分離」真空技術協会誌, **2017**, 132, 32-41.

2. Aoki, Y.; Kuroda, K.; Hinokuma, S.; Kura, C.; Zhu, C.; Tsuji, E.; Nakao, A.; Wakeshima, M.; Hinatsu Y.; Habazaki, H. “Low-Temperature Oxygen Storage of Cr^{IV}–Cr^{V} Mixed-Valence $YCr_{1-x}P_xO_{4-\delta}$ Driven by Local Condensation around Oxygen-Deficient Orthochromite” *J. Am. Chem. Soc.*, **2017**, 139, 11197-11206.

3. Zaffora, A.; Di Quarto, F.; Kura, C.; Sato, Y.; Aoki, Y.; Habazaki, H.; Santamaria, M. “Assessing the real dielectric properties of anodic Hf-Nb mixed oxides considering the interplay between their structure and composition” *submitted.*

4. 柳澤 慧，高橋 陸，中村 文彦，住谷 陽輔，飯田 良，新田 明央，倉 千晴，戸口 侑，小島 遼人，藤吉 隆雄「研究成果を記者発表する理由と課題：大学院生の視点から」*Japanese Journal of Science Communication*, **2015**, 18, 145-154.

5. 倉 千晴「愛され続ける寮歌：都ぞ弥生」*Annual Report of Hokkaido University Achieve*, **2010**, 5, 104-108.

Patents

1. 青木 芳尚，倉 千晴，幅崎 浩樹

「水素分離用膜」特願 2017-253650.

Awards

1. 平成 27 年 3 月：北海道大学物質化学部門 大塚博先生記念賞
2. 平成 28 年 1 月：HU-UCB Joint Symposium, Outstanding Presentation Award
3. 平成 28 年 5 月：東北大学金属材料研究所, 第 10 回附属新素材共同研究開発センター共同利用研究課題最優秀賞
4. 平成 28 年 11 月：第 6 回 CSJ 化学フェスタ 2016, 優秀発表ポスター賞
5. 平成 28 年 11 月：2016 年電気化学会北海道・東海支部合同シンポジウム, 優秀ポスター発表賞
6. 平成 29 年 7 月：Nagoya Univ.-Tsinghua Univ.-Toyota Motor Corp.-Hokkaido Univ. Joint Symposium, Best Poster Award

Acknowledgement

The research in the present thesis has been carried out under the guidance of Associate Professor Yoshitaka Aoki for the period of 2013-2018 in the Laboratory of Interfacial Electrochemistry, Graduate school of Chemical Science and Engineering, Hokkaido University. I wish to express my sincere gratitude to Associate Professor Yoshitaka Aoki, who gave me a chance to study on “non-filamentary resistive switching” and “hydrogen permeation membrane”, for his kind guidance, valuable suggestions and hearty encouragement through this work.

I would like to express my gratitude to Professor Kiyoharu Tadanaga, Graduate School of Engineering, and Professor Yukio Hinatsu, Graduate School of Science for their kind guidance and valuable discussion for making this thesis.

I sincerely thanks to Professor Hiroki Habazaki, Professor Emeritus Masahiro Seo and Assistant Professor Chunyu Zhu in Hokkaido University, Assistant Professor Etsushi Tsuji in Tottori University and Professor Soo-Gil Park in Chungbuk National University. Thanks to their kind help, useful advice and discussion, the present research could be accomplished.

I also thank to Dr. Yasuhiro Kumaki in Hokkaido University, Dr. Shinji Nagata in Tohoku University, Professor Roger de Souza, Professor Manfled Martin and Mr. Michael Patrick Müller in RWTH Aachen University, for their help with the measurement of NMR, RBS and SIMS.

My thanks are also extended to all the members of Laboratory of Interfacial Electrochemistry who have helped and made my research life so enjoyable; Masatoshi

Ishizuka, Ko Kakeda, Yoshiaki Taguchi, Ryo Nonaka, Hiroshi Oba, Kambun Kure, Hina Sato, Naoto Hirata, Fumitaka Kataoka, Kazumasa Kikutani, Taiki Kimura, Yuki Nakayama, Takenori Yamasaki, Keishi Inoue, Kohei Kobayashi, Shohei Kobayashi, Hiroyuki Noda, Takuya Hiraga, Shiki Matsuura, Yuto Okazaki, Kosuke Kuroda, Taisei Kobayashi, Ryosuke Sakashita, Ryosuke Tomisawa, Kanta Akane, Atsushi Kasuga, Yusuke Kunii, Sho Fujimoto, Tomoyuki Yamaguchi, Tomohiro Inoue, Yuki Sato, SeongWoo Jeong, Kentaro Takase, Keisuke Wada, Xiangjun Shen, Hikaru Kobayashi, Miku Saito, Manami Takata, Hajime Toriumi, Naohito Yamada, Cheong Kim, Laras Fadillah, Ning Wang, Tomomi Takeuchi, Michiko Hayashi, Kanae Inoue, Yoko Iwata, and all international students. All students and professors who met at conferences discussed my research sincerely. All members of Ambitious Leader's Program and technical staffs supported my research.

Special thanks are expressed to my seniors; Dr. Takashi Fujii, Dr. Ke Ye, Dr. Yoshiki Konno, Dr. Khurram Shazard, Dr. Damian Kowalski, Dr. Akira Koyama, Dr. Katsutoshi Nakayama, and my colleagues; Ryo Iida, Ryoto Kojima, Yosuke Sumiya, Riku Takahashi, Yu Toguchi, Fumihiko Nakamura, Akio Nitta and Kei Yanagisawa who gave me useful advice and continuous encouragement.

I would like to acknowledge for the supports by PRESTO "Creation of Innovative Core Technology for Manufacture and Use of Energy Carriers from Renewable Energy" project funded by Japan Science and Technology Agency, Japan, and "Nanotechnology Platform" program and "Hokkaido University Ambitious Leader's Program -fostering Future Leaders to Open New Frontiers in Materials Sciences-" of the Ministry of Education, Culture, Sports, Science and Technology, Japan.

Finally, I am particularly grateful to my family for their perpetual understandings and supports.

March 2018

Chiharu Kura